https://doi.org/10.15388/vu.thesis.21

VILNIUS UNIVERSITY
CENTER FOR PHYSICAL SCIENCES AND TECHNOLOGY

Mantas
DMUKAUSKAS

Development of MOVPE pulsed growth technique for increased efficiency InGaN/GaN multiple quantum well structures

DOCTORAL DISSERTATION

Natural Sciences,
Physics N 002

VILNIUS 2020

This dissertation was written between 2015 and 2019 at Vilnius University, Faculty of Physics, Institute of Photonics and Nanotechnology. The research was supported by The Research Council of Lithuania and FP7-ICT Collaborative project "Nanostructured Efficient White LEDs based on short-period superlattices and quantum dots" - NEWLED, Grant agreement no: 318388.

Academic supervisor:
Dr. Arūnas Kadys (Vilnius University, Natural Sciences, Physics – N 002)

This doctoral dissertation will be defended in a public meeting of the Dissertation Defence Panel:
Chairman – Prof. Dr. Vincas Tamošiūnas (Vilnius University, Natural Sciences, Physics – N 002).
Members:
Dr. Renata Butkutė (Center for Physical Sciences and Technology, Technological Sciences, Materials Engineering –T 008);
Dr. Tomas Čeponis (Vilnius University, Natural Sciences, Physics – N 002);
Dr. Pranciškus Vitta (Vilnius University, Natural Sciences, Physics – N 002);
Prof. Dr. Nerija Žurauskienė (Center for Physical Sciences and Technology, Natural Sciences, Physics – N 002).

The dissertation shall be defended at a public meeting of the Dissertation Defence Panel at 16:00 / on May 28th 2020 in the Center for physical sciences and technology.
Address: Saulėtekio Av. 3, A101 Room, Vilnius, Lithuania.

The text of this dissertation can be accessed at the libraries of Vilnius University as well as on the website of Vilnius University:
www.vu.lt/lt/naujienos/ivykiu-kalendorius

https://doi.org/10.15388/vu.thesis.21

VILNIAUS UNIVERSITETAS
FIZINIŲ IR TECHNOLOGIJŲ MOKSLŲ CENTRAS

Mantas
DMUKAUSKAS

MOVPE impulsinio auginimo technologijos kūrimas ir taikymas padidinto efektyvumo InGaN/GaN kvantinių duobių struktūrose

DAKTARO DISERTACIJA

Gamtos mokslai,
Fizika N 002

VILNIUS 2020

Disertacija rengta 2015– 2019 metais Vilniaus universiteto, fizikos fakulteto fotonikos ir nanotechnologijų institute.
Mokslinius tyrimus rėmė Lietuvos Mokslų Taryba bei FP7-ICT projektas: "Nanostructured Efficient White LEDs based on short-period superlattices and quantum dots" - NEWLED, Paramos numeris: 318388.

Mokslinis vadovas:
dr. Arūnas Kadys (Vilniaus universitetas, gamtos mokslai, fizika – N 002).

Gynimo taryba:
Pirmininkas – **Prof. dr. Vincas Tamošiūnas** (Vilniaus universitetas, gamtos mokslai, fizika – N 002).
Nariai:
Dr. Renata Butkutė (Fizinių ir technologijos mokslų centras, technologijos mokslai, medžiagų inžinerija – T 008);
Dr. Tomas Čeponis (Vilniaus universitetas, gamtos mokslai, fizika – N 002);
Dr. Pranciškus Vitta (Vilniaus universitetas, gamtos mokslai, fizika – N 002);
Prof. dr. Nerija Žurauskienė (Fizinių ir technologijos mokslų centras, gamtos mokslai, fizika – N 002).

Disertacija ginama viešame Gynimo tarybos posėdyje 2020 m. gegužės 28 dieną, 16.00 val., Nacionaliniame fizinių ir technologijos mokslų centre (NFTMC) A101 auditorijoje. Adresas: Saulėtekio al. 3, Vilnius,.

Disertaciją galima peržiūrėti Vilniaus universiteto ir Fizinių ir technologijos mokslų centro bibliotekose ir VU interneto svetainėje adresu:
https://www.vu.lt/naujienos/ivykiu-kalendorius

ACKNOWLEDGEMENT

First of all I would like to thank my supervisor doctor Arūnas Kadys, for support. He gave me the chance to become a part of the research team and helped me to develop my skills as an epitaxial growth specialist.

Secondly, I am grateful to my colleagues – chef prof. Dr. Roland Tomašiūnas, Dr. Tadas Malinauskas, Dr. Jūras Mickevičius, prof. habil. Dr. Gintautas Tamulaitis, as well as Dr. Darius Dobravolskas, Dr. Ignas Reklaitis, Dr. Sandra Stanionytė and Dr. Martynas Skapas who provided me with measurement results and gave me valuable ideas and insights.

Also I am grateful to Vilnius University, Research Council of Lithuania and FP7 NEWLED project, for my PhD research funding.

Finally, I am grateful to my wife Milda and my daughter Nida, who encouraged and supported me throughout this work.

TABLE OF CONTENTS

LIST OF ABBREVIATIONS

AFM	Atomic force microscope
AlN	Aluminum nitride
BSF	Basal plane stacking fault
CBM	Conduction band minima
CCS	Close-couples showerhead
CW	Continuous wavelength
Ebeam	Electron beam
EL	Electro-luminescence
EM	Electromagnetic
EQE	External quantum efficiency
FWHM	Full wavelength of the half maximum
GaN	Gallium nitride
In	Indium
InGaN	Indium gallium nitride
IQE	Internal quantum efficiency
LD	Laser diode
LED	Light emitting diode
LEE	Light extraction efficiency
MFC	Mass flow controllers
MO	Metalorganic precursor
MOVPE	Metal-organic vapor phase epitaxy
MQW	Multiple quantum well
NI	Nucleation islands
NRC	Non-radiative recombination centers
PCC	Pearson correlation coefficient
PE	Piezoelectric
PL	Photoluminescence
QB	Quantum barrier
QCSE	Quantum confined Stark effect
QW	Quantum well
RMS	Root-mean-square
RSM	Reciprocal space mapping
RT	Room temperature
RTPL	Room temperature PL
SD	Surface defects
SF	Stacking fault
SL	Superlattice

SMB	Stacking mismatch boundary
SP	Spontaneous polarization
SSL	Solid state lighting
STEM	Raster TEM scan
TDPL	Temperature dependent PL
TEM	Transmission electron microscope
TMAl	Tri-Methyl-Aluminum
TMGa	Tri-Methyl-Gallium
TMIn	Tri-Methyl-Indium
TRD	Trench defect
uGaN	Unintentionally doped GaN
UL	Underlayer
VBM	Valence band maxima
Wz	Wurtzite
XRD	X-Ray diffractometer
ZB	Zinc blende
µPL	Spatially-resolved PL

INTRODUCTION

Light emitting diodes (LEDs) and laser diodes (LDs) are optoelectronic luminous devices with various applications ranging from home appliances to scientific research. Indium gallium nitride (InGaN) is a versatile material used for creating luminous optoelectronic devices and is desirable due to its tunable property within the visual spectrum which one may do by changing the concentration of indium [1, 2]. Since the discovery of blue LEDs in the early nineties [3], InGaN heterostructures have made significant technological advances in solid state lighting (SSL) by increasing the efficiency of SSL technology and reducing energy consumption as well as expanding the color range of LEDs [2].

However, InGaN has not yet fully reached its promising potential, regarding efficiency, based on theoretical modeling, particularly within the green spectrum. Currently several challenges exist that prevent reaching theoretical efficiencies. One such challenge is the existence of large lattice mismatches, which cause internal stresses that results in high internal piezoelectric fields or defect formation.

Additionally, the large lattice mismatches also cause indium segregation, which further decreases efficiency [4]. Segregation is also a result of lower growth temperature and higher indium (In) concentration that are required to achieve green light emissions, yet also lead to a high defect density [5]. At lower temperatures and higher In concentrations a miscibility gap develops in addition to coherency strain, which results in spinodal decomposition. Ultimately, the atoms in the upper layer segregate forming an uneven distribution of material or separate islands [6]. The uneven distribution causes fluctuations in the energetic bands resulting in a carrier trap, which produces a red-shift of emission and a broadening of the full wavelength of the half maximum (FWHM). Carriers in green emitting MQWs have a long diffusion length, for which many carriers recombine non-radiatively before reaching localization centers [7]. Those carriers, that manage to reach localization centers are trapped and even though, it prevents from non-radiative recombination centers (NRC), the effective luminous surface is reduced, which ultimately reduces emission efficiency. Efficiency is further reduced when carriers are trapped in localization centers with dislocations inside, where it is highly unlikely that radiative recombination will occur [8]. Therefore, in order to increase the active layer efficiency, indium segregation must be minimized. Currently several techniques have been suggested that may increase the efficiency of InGaN MQWs within the green spectral region.

One way to increase MQW efficiency is a short period of TMIn supply before the growth of QW [9, 10]. Indium atoms can bond at the core of a threading dislocation that results in prevention of dislocation glide during growth of QW.

The threading defect reduction results in increased internal quantum efficiency, yet this does not reduce In segregation. Another way to increase efficiency is growing crystals on a Semi-polar GaN substrate [11, 12]. Semi-polar GaN substrates are more lattice matched with InGaN QWs, than c-plane sapphire substrates. MQWs grown on semi-polar substrates are therefore less stressed which results in piezoelectric field reduction and homogenous growth of InGaN QWs even at high In concentrations. Semi-polar GaN substrates are still relatively expensive when compared with c-plane sapphire substrates. Thus cost leads us to find new solutions for more efficient crystal growth using the economical c-plane sapphire substrate. One of the methods to increase efficiency on a c-plane sapphire substrate that has not been fully analyzed is by using a pulsed growth technique, which may reduce In segregation [13, 14]. In a pulsed growth technique of QWs, TMIn flow is periodically interrupted, while the rest of gas flow is kept unchanged. During the interruption indium atoms desorb reducing the indium inhomogeneous distribution.

In this thesis the experimental work of pulsed growth technique by using metal-organic vapor phase epitaxy (MOVPE) and analysis were presented. The influence of pulse and pause duration as well as total growth time and growth temperature on InGaN MQW characteristics were analyzed. Structural as well as optical characteristics of InGaN MQWs were assessed. Finally, pulsed growth technique was applied during the growth of InGaN LEDs.

Aim

The aim of this thesis was to develop an MOVPE pulsed growth technique to increase the efficiency of InGaN/GaN multiple quantum well structures for use in high brightness green light-emitting diodes and to explain the underlying causes for the changes in the optical properties.

The work for this thesis was part of the FP7 NEWLED project, whose aim was to develop a new technological approach for the growth and design of LED structures based on the (In,Ga,Al)N and (In,Ga,Al)(As,P) material systems to cover the whole visible range. The project‘s partners included Osram Opto Semiconductors – a leading LED company in Europe as well as 13 other institutions and companies throughout Europe. One of the project’s tasks was to grow III-nitride QW structures using the pulsed MOVPE method, which is the work that is presented in this thesis.

Objectives

1. To develop an MOVPE pulsed growth technique for InGaN alloy film in the Aixtron flip-top close-coupled showerhead reactor.
2. To determine the optimal temporal MO flow parameters at different growth temperatures at which InGaN/GaN MQW photoluminescence intensity is increased compared to conventionally grown InGaN/GaN MQWs by measuring the structural and optical properties of the grown structures.
3. To characterize the carrier localization profile in InGaN MQWs grown by conventional and pulsed growth modes.
4. To apply the pulsed growth technique to create high brightness LED structures using the optimized MQW growth parameters.

Key findings

- In a pulsed growth technique, for InGaN QWs, an optimized pause duration for a given temperature should be used, and 1 to 4 monolayers of InGaN should be grown during a single pulse growth cycle to achieve the greatest PL enhancement.
- The pulsed growth technique is superior at creating higher density localized states and enhancing PL intensity compared to QWs grown at higher temperatures using the conventional growth method. Additionally, the inevitable PL peak blueshift is observed in both techniques.
- The PL intensity enhancement achieved in pulsed grown InGaN MQW is governed by the modification of the carrier localizing potential due to enhanced migration of In atoms during the crystal growth and creation of a smaller size and a higher density of indium-rich clusters in QWs.

Novelty of the Work

To our knowledge, this work is the first to show how the range of pulsed growth technique parameters (pulse/pause duration and growth temperature) for InGaN MQW structures influence the outcome as parameters are changed incrementally. This study has established the optimal pulsed growth parameters for InGaN MQW, which can be used in future applications for growing green-light emitting MQWs.

Author's Contribution

- The author has designed the protocol for the pulsed growth technique and performed the major part of the growth experiments.
- The author has performed or assisted with the characterization, data analysis and interpretation.
- The author has drafted or significantly contributed to the editing of the manuscripts for publication, the results of which are presented in this thesis.

Layout of the Thesis

The thesis begins with the short introduction, which describes the interest in InGaN material, the problems related to it, possible solutions to those problems, and presents the pulsed growth technique as a solution for higher efficiency InGaN materials and devices.

First chapter briefly introduces the InGaN structural, optical and electrical properties, characteristics as well as material application in multiple quantum well structures.

Second chapter provides an overview of InGaN growth using metalorganic vapor phase epitaxy and growth related problems, which prevent scientists from reaching the material's potential theoretical quality.

Third chapter walks us through the experimental equipment and methods, which were used in this research.

Fourth chapter depicts how the samples in this research were grown and which growth parameters were used.

In fifth chapter the research results are presented and discussed. First, the structural measurements and analysis are presented, followed by the optical measurements and analysis. Two group of samples (green and cyan) are analyzed respectively.

Sixth chapter is dedicated to carrier localization issues. The analysis of how the pulsed growth technique influence localization profile as well as the resulting optical outcomes are presented.

Finally, the seventh chapter presents the pulsed growth technique application to LED structure growth.

Conclusions are presented at the end of the thesis.

List of conference contributions (poster) related to the dissertation

M. Dmukauskas, T. Malinauskas, R. Tomašiūnas, J. Mickevičius, D. Dobrovolskas, M. Skapas, S. Stanionytė, and A. Kadys, Comparative study on structural and optical properties of InGaN/GaN MQWs grown by pulsed MOVPE, Material Research Society Fall Meeting and Exhibit, Boston, US, 2018.

M. Dmukauskas, M. Kolenda, A. Kadys , T. Malinauskas, M. Skapas, J. Mickevičius, R. Tomašiūnas, "All-optical research of In segregation suppression in InGaN QWs grown by MOVPE using metal precursor multiple flow interruptions", 17th European Workshop on Metalorganic Vapour Phase Epitaxy (EW-MOVPE17), Grenoble, France, 2017.

M. Dmukauskas, M. Kolenda, A. Kadys, T. Malinauskas, M. Skapas, J. Mickevičius, R. Tomašiūnas, Metalorganic chemical vapor deposition pulsed growth technique influence on In segregation in InGaN QWs, 19-th International Conference-School Advanced Materials and Technologies, Palanga, Lithuania, 2017.

M. Dmukauskas, A. Kadys, T. Malinauskas, T. Grinys, I. Reklaitis, D. Dobrovolskas, S. Stanionytė, M. Skapas, I. Pietzonka, R. Tomašiūnas, Growth of InGaN QWs by MOVPE Using Pulsed Precursor Flow, NEWLED WORKSHOP on Growth of nitride LEDs, Rome, Italy, 2015.

M. Dmukauskas, A. Kadys, T. Malinauskas, T. Grinys. I. Reklaitis, D. Dobrovolskas, S. Stanionytė, I. Pietzonka, R. Tomašiūnas, Blue and green InGaN MQW growth using pulsed MOVPE technique, National conference of Lithuania, Vilnius, Lithuania, 2015.

1 PROPERTIES OF III-N SEMICONDUCTORS

1.1 Crystal Structure

Periodic arrangement of atoms is the key feature of crystal structures, which enables the existence of energy bands and a gap between them [15, 16]. The carriers can easily move throughout the crystal in the energy bands. In the energy gaps there are no energy states and thus carriers cannot exist. Semiconductor materials can be divided into two different classes depending on their band structure with either direct or indirect bandgap behavior (see figure 1.1). The excited electrons occupy the upper – conduction band minima (CBM) and holes are located in the valence band maxima (VBM). Charge carriers can recombine only when the conservation law is met, which occurs when the carrier maintains it's momentum. In indirect band gap materials the electrons in CBM have different momentum from the holes' in the VBM and therefore to recombine they require a third component – a phonon, which can change the electron's momentum to match with the hole's. III-N are direct band gap materials, their CBM is located at the same electron wave vector (k) value as the VBM, so the radiative recombination from CBM to VBM has a much higher probability than the indirect bandgap materials. This is an important feature for III-N optoelectronic applications.

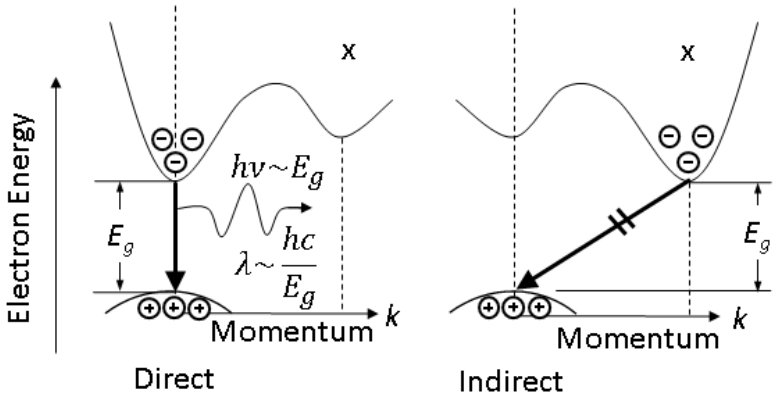

Figure 1.1. Direct and indirect energy bands.

III-Ns possesses the ionic bonding. The bandgap energy tends to increase for compound semiconductors composed of light elements and also having high ionicity in bonding [17]. III-N band gaps are: 0.7±0.05 eV for InN, 3.52±0.1 eV for GaN and 6.1±0.1 eV for AlN [18, 19]. By controlling the mole fraction of each binary component it is possible to achieve ternary alloys such as $In_xGa_{1-x}N$ with

different compound ratios ($0<x<1$) that overlap the visible spectrum. That is a huge advantage of III-N materials. The relationship between the InGaN compound's mole fraction and bandgap can be easily expressed by using Vegard's law (1.1), where $E_{g(\mathrm{In})}$ and $E_{g(\mathrm{Ga})}$ are In and Ga fundamental bandgap energies and b is a bowing parameter which is specific for material compounds and for InGaN is b= 1.32±0.28eV [20].

$$E_g(In_xGa_{1-x}N) = xE_{g(In)} + (1-x)E_{g(Ga)} - bx(1-x) \qquad (1.1)$$

The III-nitride materials have three possible crystal structures – zinc blende (ZB), rocksalt or wurtzite (Wz). The ZB structure of III-N can be produced by epitaxial growth using cubic substrates such as GaAs or Si, though the crystals are metastable. Rocksalt structure can only be achieved under high pressure in a laboratory environment and thus does not have any practical applications. Only the Wz structure is thermodynamically stable and is usually used in III-N optoelectronics [21] .

The Wz atomic layers are arranged in the alternating hexagonal close-packed (hcp) planes with the group III and N element sublatices, following the sequence of ..ABABAB.. as schematically illustrated in figure 1.2, which depicts a Wz GaN unit cell. The atoms in the Wz structure are tetrahedrally bonded to the nearest neighbor. Wz structure is described by two lattice parameters: a and c. Lattice constant a describes the distance between atoms in the sublattice plane, while lattice constant c is perpendicular to the base plane and describes spacing between two sublatices of the same element. The displacement of the hcp sublatices with respect to each other along the c-axis is characterized by the dimensionless parameter u, which is defined by the bond length along the c axis between the cation and the anion divided by the lattice constant c. In other words, u is a factor characterizing bond length along the c-axis, as well as, distortion of the unit cell. In an ideal wurtzite crystal u is always equal to 0.375 and the c/a ratio is always 1.633. Yet, differences in the electronegativity and the strong ionic character of III group elements and N atoms causes the deviations of u and c/a, modifying the GaN unit cell from the ideal Wz structure (see table 1.1). This modification is the reason for the strong polarization that occurs in III-N materials [22].

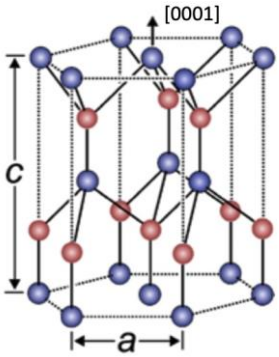

Figure 1.2. Schematic representation of GaN wurtzite unit cell. Blue balls represent group-III atoms, red – N atoms. a and c – lattice constants. Copyright, owned by U.W. Pohl; used by permission [23].

Table 1.1. Lattice parameter values of III-N alloys [24].

Material	*a* (Å)	*c* (Å)	*u*	*c/a*
InN	3.544	5.762	0.377	1.626
GaN	3.193	5.218	0.376	1.634
AlN	3.070	4.910	0.382	1.600

The sequence of III and N element sublatices stacked on top of each other along the *c* direction results in an internal asymmetry that creates polarity of crystals. Polarity of Wz crystals can be either Ga-polar - directed from the surface towards the substrate, or N-polar, directed from the substrate towards the surface. Polarity depends on the growth conditions. GaN growth on a sapphire substrate using MOVPE usually results in Ga-polar materials [25]. Polarity of Wz crystals create macroscopic spontaneous polarization (SP). The magnitude of SP is described by the spontaneous polarization constant p_{sp}, which in III-N materials can initiate an internal electric field up to 3MW/cm [22]. Generally, spontaneous polarization inside the films occurs uniformly.

Due to the lack of suitable native substrates III-nitrides are commonly grown on mismatched substrates with a different lattice constant *a*. This initiates the compressive or tensile stress in a lateral direction that generates piezoelectric (PE) field, which for the III/N can be up to 2MV/cm [22]. III-N materials, grown on a sapphire substrate experience compressive strain and the PE fields are directed from the surface towards the substrate.

Formula (1.2) depicts piezoelectric polarization along the (0001) axis, which is expressed via the piezoelectric coefficients e_{33} and e_{13}.

$$\delta P_3 = e_{33}\epsilon_3 + e_{31}(\epsilon_1 + \epsilon_2) \quad (1.2)$$

Here $\epsilon_3=(c-c_0)/c_0$ is the strain along the c axis, and $\epsilon_1=\epsilon_2=(a-a_0)/a_0$ is the in-plane strain, which is assumed to be isotropic (c_0 and a_0 are the equilibrium values of the lattice parameters). Values of III-N piezoelectric coefficients are presented in table 1.2.

Having no external fields, the total macroscopic polarization P is the sum of the PE and SP. Thus, for III-N materials the total internal polarization field can be up to 5MV/cm.The piezoelectric and spontaneous polarizations have a significant influence on III-N quantum wells, which will be discussed further.

Table 1.2. Spontaneous polarization and piezoelectric coefficients [26].

Material	p_{sp}(C/m^3)	e_{31}(C/m^3)	e_{33}(C/m^3)
GaN	-0.029	-0.49	0.73
InN	-0.032	-0.57	0.97
AlN	-0.081	-0.60	1.46

1.2 Multiple Quantum Wells

The quantum well (QW) is a structure formed by the thin layer of semiconductor with a lower bandgap sandwiched between two layers of another semiconductor with a larger band gap. These two layers form a quantum barriers (QB) and the middle layer – a quantum well. To achieve quantization, the QW thickness has to be comparable to the de Broglie wavelength, and for III/N QW thickness is usually ~3 nm. Carriers in the QW generated optically or injected electrically via the contacts are confined to the quantized discrete states. Confinement increases the electron and hole wave function overlap and the internal quantum efficiency. Increasing the carrier concentration in the QW results in filling of higher states up to the barrier level, where further increase of carriers results in their escape from the active region. Stacking more QWs on each other and making a multiple QW (MQW) structure can solve this problem. In theory another method to increase the number of energy states in the QW would be by growing wider QWs. However, the existence of polarization fields initiates a quantum confined Stark effect (QCSE). The QCSE occurs in the QWs when an external or internal

electric field is applied, which bends the QW and spatially separates the electron from the hole (See Figure 1.3). The separation increases when the QW width is increased. The overlapping of the electron's and the hole's wave functions decreases which in turn reduces recombination efficiency. Also QCSE reduces the band gap and the spectrum is red-shifted. Thus, growing narrower QWs can reduce the impact of the QCSE effect. Also, QCSE can be decreased when the high carrier concentrations are injected, which begin to screen the internal electric field.

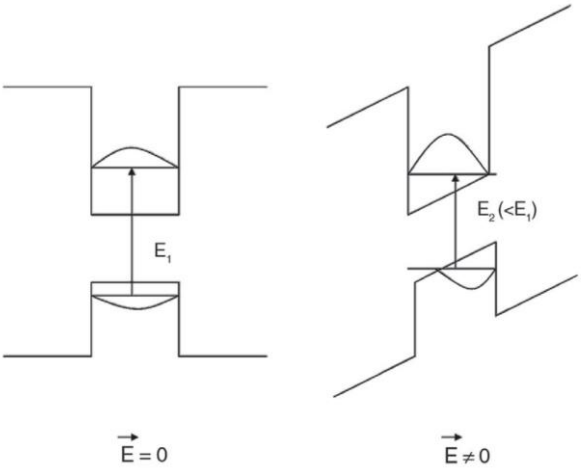

Figure 1.3. Illustration of ideal QW with no electric field and influence of QCSE, when the electric field is applied. Copyright, owned by S. Mokkapati; used by permission [27].

2 GROWTH KINETICS

Growth of III/V material by MOVPE can be divided into three steps: 1) kinetic, or gas transport to the growth region, 2) thermodynamic, or chemical reactions of precursor, decomposition and bonding to the substrate surface, 3) byproduct exhaust to vent.

The first step of growth kinetics depends on material diffusion through the boundary layer – thin layer of gas with the MO concentration gradient [28]. Diffusion through the boundary layer depends on system pressure and temperature. Diffusion coefficient is inversely proportional to the pressure, thus at lower growth pressure a mass transport of precursors through the boundary layer is induced.

Growth kinetics can be divided into three regimes depending on a growth temperature (figure 2.1). During the growth of GaN, when the growth temperature is low (<750K) overall material at the substrate surface reaction rate is low. Material concentration on the substrate is high and diffusion through the boundary layer is low. The growth rate is low, however it increases with temperature. The kinetic limiting growth rate depends on overall reaction rate and it can be expressed as:

$$Rate = Ae^{-\left(\frac{E_a}{RT}\right)} \tag{2.1}$$

Here A is a MO vapor pressure constant, E_a is the activation energy and R is a Boltzmann constant. One can see, that during kinetic limiting regime growth rate strongly depends on a growth temperature. By increasing growth temperature further (750-1200K) material reaction rate increases, gradient of material concentration in the boundary layer becomes higher. Higher gradient of material concentration initiates stronger MO diffusion through the boundary layer. Growth rate increases, though it becomes little dependent on temperature.

Nitrogen has a lower bonding energy than the III-group materials, which not only facilitates N incorporation, but increase desorption as well [29]. Atomic nitrogen concentration depends on its source – ammonia. Ammonia cracking rate depends on a growth temperature. If the growth temperature is lower or the supply of ammonia is lower atomic nitrogen concentration decrease. In this case lack of atomic nitrogen can become a limiting growth factor.

To avoid growth limitation due to the lack of atomic nitrogen, ammonia is usually oversupplied during the crystal growth. Ammonia is oversupplied by choosing high V/III ratio. Consequently, limiting growth factor becomes the supply rate of the MO precursors to the wafer surface.

In addition, growth of nitride materials is always accompanied by the surface layer decomposition and desorption, which depends on a temperature and on a carrier gas and its amount. As an example, hydrogen has high thermal conductivity, which initiates In prereaction, increase In desorption and hinders In incorporation [30, 31]. However, N_2 is a preferred carrier gas during the growth of In containing materials. On the other hand, In desorption can be suppressed if the mass flux of TMIn through the boundary layer is increased. TMIn supply increases when the set ratio of TMIn/TMGa is higher [32].

As the growth temperature increases above (>1200K) the point is reached, where material desorption rises significantly, which begins to reduce the growth rate by further temperature increase. Usually crystal growth by using MOVPE takes place in transport-limited regime, because of easier way to control growth rate.

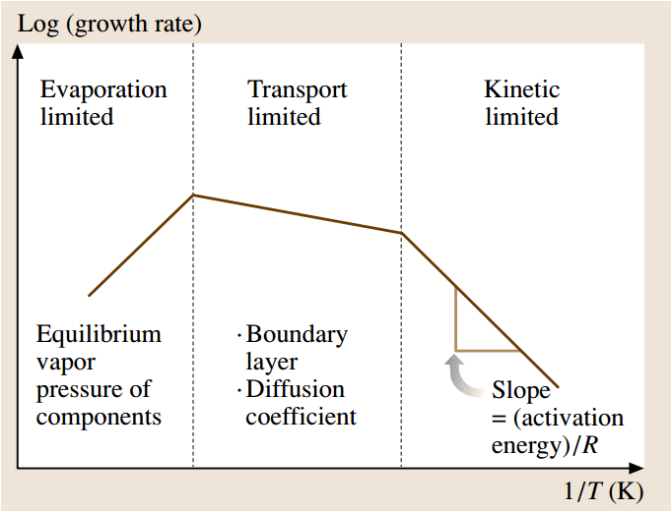

Figure 2.1. MOVPE nitride material growth regimes. Copyright, owned by S. Kasap; used by permission [33].

The deeper understanding of GaN growth can be addressed by analyzing thermodynamics. Once the gasses are introduced to the reactor chamber, the adduct formation between ammonia and TMGa begins. On the way to the wafer surface, the temperature increases and at around 400K the decomposition of gases begins. First TMGa:NH_3 aduct decomposes into the $DMGaNH_2$ and later into the MMGaNH by eliminating methane molecules. Finally, at temperatures above 1200K dominating process is the last methane and carbon elimination and GaN formation on a substrate surface. GaN diffuse laterally on a surface until reaching

the suitable crystal site, where it is incorporated. This GaN growth path is the most probable, though other paths as can be seen in figure 2.2 exist as well [34]. The reduced growth temperatures as used for InGaN growth can increase the byproduct (especially carbon) incorporation.

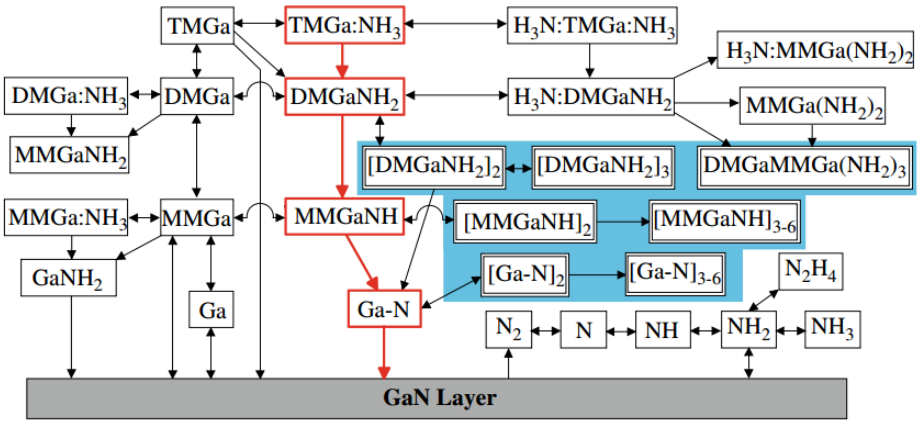

Figure 2.2. Schematic GaN growth by MOVPE pathways. Copyright, owned by D.Ehrentraut; used by permission [35].

2.1 Crystal Defects

Growth of III-N on the non-native substrates is always accompanied by some degree of defect formation. Lattice mismatch and difference in thermal expansion coefficient between the substrate and the epitaxial layer originates strong tensile or compressive stresses. The stress is relieved when crystal layer relaxes through formation of a threading dislocation TD or a stacking fault (SF) [36].

The density of TD in GaN usually lay in the range of 10^6 to 10^{10} cm^{-2} [37]. TD density depends on the substrate, growth method, epitaxial layer and its thickness. TD reduces the crystal quality, because it acts as a non-radiative recombination centers. TD usually generates during the coalescence of the nucleation islands (NI). The role of dislocation is to adopt the misalignments of the NI when they coalesce. There are three types of dislocations: edge, screw or mixed type (the product of former two). Edge type dislocations are mainly created at the boundaries of NI due to the in plane twist of the NI. Screw or mixed type dislocations are usually created inside the NI. The screw components created by the NI tilt misalignment. Majority of dislocations run in parallel with the surface normal. Usually, the edge type dislocations dominates as a threading defect, especially when the grain diameters

are <1 μm [38]. Meanwhile the screw dislocation densities are not influenced by the grain diameters.

As the crystal thickness increase, the surface becomes more even, the mosaic feature of coalesced islands with misorientations disappears. TD formed at the interface of nucleation layer and GaN buffer layer extends along the *c*-direction up to the MQW. Thicker buffer layer reduces TD density, as more dislocations annihilate in pairs. At the MQW TD can create a V-pit - a defect with V-shaped hexagonal walls {10-11} that include thinner InGaN/GaN layers than the rest of the MQW. Figure 2.3 represents the schematic formation of a TD and a V-pit inside the MQW.

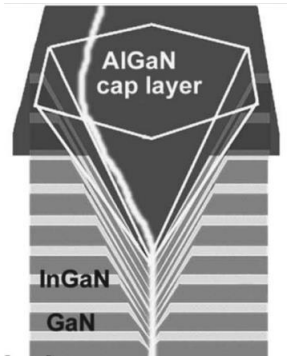

Figure 2.3. Schematic representation of a V-pit inside the MQW. Copyright, owned by F. C. P Massabuau; used by permission [39].

The formation of V-pits begins, when the growth temperature is reduced and In is introduced. Strained field around the TD captures In atoms, and they segregate [40-42]. Further segregated In act as a mask for TD and hinders the Ga migration on the (0001) monolayer. Ga becomes terminated on the six {10-11} planes. With the MQW growth InGaN/GaN layers grow on {10-11} sidewalls as well, although the growth rate is low and the layers on {10-11} sides are thinner than on the (0001) plane. The capping layer grown on top of the MQW fills the V-pit. Still, TD propagates to the free surface through the V-pit filled with the capping layer.

The second way for epitaxial layer under the stress to relax is through formation of a stacking fault – a disorder of crystallographic planes. The dominating stacking faults in nitride materials grown on the polar substrates are the basal plane stacking faults (BSF). BSF are created, when the stacking order of *ABABABAB* along the *c*-axis is transformed into the order of *ABABCBCB* (see figure 2.4).

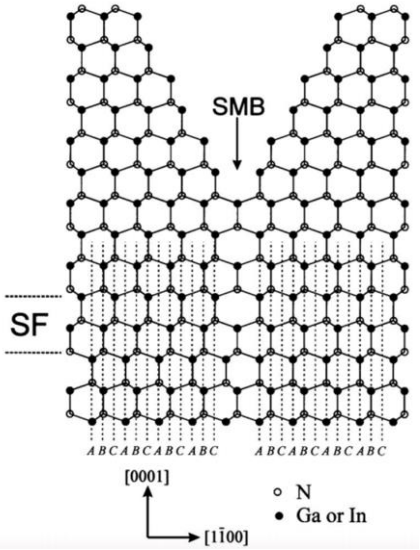

Figure 2.4. Schematic representation of a SMB and V-shaped grove formation. Copyright, owned by H. K. Cho; used by permission [43].

The BSF generate stacking mismatch boundary (SMB), when the faulted area on the left-hand side (*ABABCBCB*) meets the correct area (*ABABABAB*) on the right-hand side. The SMB propagates through the material and usually in the MQW creates a V-shaped grove – a trench defect (TRD). The schematic representation of a TRD is presented in figure 2.5. Figure 2.6 presents the image of InGaN MQW surface measured with AFM, where the TRD as well as TD can be identified. The density of TRD is often similar to the density of TD [39]. SMB as well as TRD often encloses small material region that posses different emission properties than the surrounding area. SMB relax the enclosed region and allows higher In incorporation often resulting in a red-shifted and intensified emissions than the surrounding area. On the other hand, relaxation of the area in vicinity of TRD decrease the QCSE effect. If the higher amount of In is not incorporated, the photoluminescence (PL) from the area in vicinity of a TRD blueshifts. On the other hand trenches act as NRC and reduce overall material internal quantum efficiency. Thus, defect elimination is always one of the key goals in increasing material quantum efficiency.

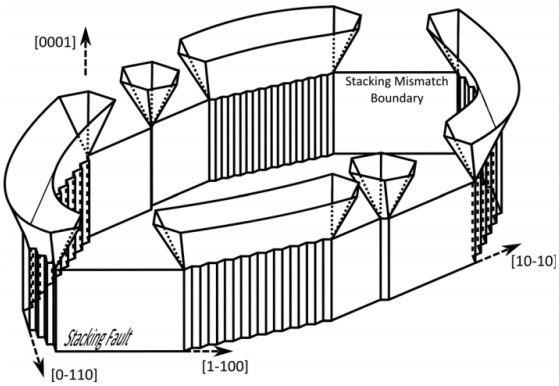

Figure 2.5. Schematic V-pit representation. Copyright, owned by M. Shiojiri; used by permission [40].

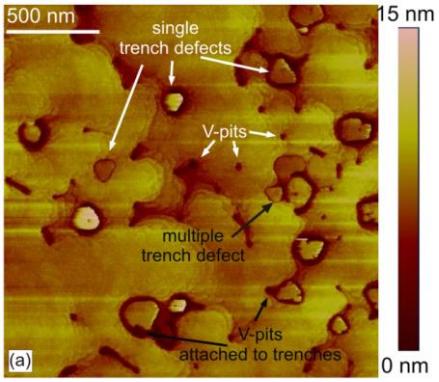

Figure 2.6. AFM image of a InGaN MQW surface, where the trench defects and V-pits can be identified. Copyright, owned by J. Smalc-Koziorowska; used by permission [44].

2.2 Indium Segregation

One of the goals when growing composite materials, such as $In_xGa_{1-x}N$, is to achieve even distribution of material across the surface area. Under optimized growth conditions when the In concentration is low (<15%) it is possible to create the InGaN layer more or less laterally homogeneous [45]. Although higher In concentration is followed by the rise of coherency strain.

The capability of incorporating higher amount of In into the InGaN layer becomes problematic, because increasing strains tend to relax by forming defects as well as initiating In segregation (metallic In droplet formation or inhomogeneous In distribution between In-rich clusters) [4]. The InGaN, grown on

c-plane GaN coherency strain limit is no more than 20% of In [46]. Though, usually even smaller amount of In leads to the lattice relaxation through the defect formation. As a result, InGaN material with higher In concentration possess low quantum efficiency which is called the “green gap” problem. Coherency strain can be reduced by growing InGaN on the native substrates or by using lattice strain adjusting techniques, such as inserting superlattices [47] or strain adjusting layers [48].

Indium segregation is a result of lower growth temperatures and higher indium (In) concentration that are required to achieve green light emissions [5]. Lower growth temperature leads to ineffective ammonia cracking and depression of atomic nitrogen [13]. Indium atoms, lacking atomic nitrogen forms In clusters, that can be incorporated into the material as a metallic In droplets. The process is boosted by the lower energy of InGaN surface, that facilitates In atoms in the subsurface to exchange with the surface. Also, at lower temperatures and higher indium concentrations a miscibility gap appears and coherency strain increases between different materials resulting in spinodal decomposition which results in an uneven distribution of material [6]. In segregation induces the In gradient along the growth direction as well as In content fluctuations on the surface [49]. Furthermore, it also modifies the conduction and valence band shape, which results in a higher spatial separation of electrons and holes as well as reduces the in-plane carrier wave function overlap resulting in a decreased MQW efficiency [50].

On the other hand, to some extent uneven distribution of In causes fluctuations in the energetic bands resulting in a carrier trap, which produces a red-shift. To some degree In-rich cluster formation is advantageous, when one tries to get PL peak deeper into the green region. Though, usually In has an inhomogenous distribution between In-rich clusters resulting not only in a redshift but the broadening of the full wavelength of the half maximum (FWHM) as well.

Carriers in the green emitting MQWs have a long diffusion length of few hundred nm, for which many carriers recombine non-radiatively before reaching localization centers [7, 46]. Those carriers that manage to reach localization centers are trapped and prevented from migration to the NRC. Because most of emission is from localization centers the effective luminous surface is reduced, which ultimately reduces emission intensity and efficiency at higher excitation. Efficiency is further reduced when carriers are trapped in localization centers where dislocations exist and where it is highly unlikely that radiative recombination will occur [8]. Therefore, in order to increase the active layer efficiency, the metalic indium segregation as well as inhomogenous distribution of In in In-rich clusters must be minimized. There are couple of techniques, which can reduce In segregation.

First of all, optimal growth conditions must be set. In segregation is temperature sensitive - higher growth temperatures reduce In segregation. On the other hand, higher growth temperatures increase In desorption and reduce overall In concentration. Lowering TMIn flow results in a similar outcome – the reduced source of atomic In reduces overall In concentration as well as In segregation.

Secondly, additional growth optimization techniques might be applied. The simplest way to reduce In segregation is by growing InGaN MQW homoepitaxially on a native GaN substrate [35]. Although, GaN substrates are still relatively expensive, thus many are keen to find alternative growth techniques.

Wang et. al. suggested, that the temperature ramp up process between the growth of QW and QB can decrease the indium segregation [51]. At the end of QW growth flow of all MO is interrupted, keeping only the flow of NH_3 and the temperature is being ramped up to the temperature of QB growth. During this process InGaN layer is not protected with the GaN layer, and some of In clusters decomposes. According to Oliver et. al. such QW reveal to increasing temperatures results not only in reduction of In clusters, but also in evaporation of the InGaN layer itself that leaves the InGaN layer with gross width fluctuations [52]. In fact, such QW width fluctuations can be beneficial in carrier localization and increase the IQE.

Another possible solution is by introducing the different flows of hydrogen after the QW growth, before the growth of QB. In is very sensitive to H_2, as it becomes volatile and quickly desorbs, leaving GaN areas and thus changing the QW from two dimensional layer into three dimensional islands [53]. On the other hand, Lundin et. al. showed, that the hydrogen-free atmosphere during the MO interruption between QW and QB growth is more advantageous for the green MQWs [54]. In desorption is not that volatile and it helps to provide the formation of much more stable localizing regions with high indium content that contributes to enhanced emission efficiency.

There have been several works suggesting that the characteristics of InGaN layers and MQW structures could be improved, if they were grown with MO flow interruptions – to supply MO into the reactor chamber in pulses [55-59]. Lai et. al. suggested that MO flow modulation during the growth of InGaN QW can reduce V-pit density and reduce surface roughness [60]. Although, the MQW emission is blueshifted and the droop effect increased.

Rossow et. al. suggested the two stage process taking the place during the growth of InGaN MQWs, that could explain the possible benefits of the pulsed growth technique [61]. During the InGaN growth, adsorbed III-group atoms initially form an adlayer and only from the adlayer they are incorporated into the crystal lattice. If the growth temperatures are high, desorption rates are high and it

is likely that the second adlayer is not completely filled. Reducing the growth temperatures increase the occupation of the second adlayer as well as probability of In incorporation. When the second adlayer is filled In can easily diffuse laterally and form In clusters, which after certain point becomes stable In droplets. Further, In droplets can ether feed the adlayer and be incorporated, desorb or remain as a point defect, which is especially likely if the excess In is constantly supplied from the gas phase. Thus, MO flow interruption can increase the chances of first two paths, that lead to reduction of In droplet concentration.

The existence of In source (droplet) at the adlayer can be proved by the fact, that after applying growth interruptions (during which some of In should desorb), the overall In concentration in the layer does not reduce, but contrary can increase up to two times. Thus, it proves, that growth of higher In concentration layers tends to form In droplets. Growth with interruptions reduces In droplet concentration and distributes In composition inside the QW more uniformly [13]. As a result density of localized energy states reduces. Reduced In segregation reduces the In-gradient along the growth direction and its built-in field, which modifies the valence and conduction bands. As a result energy bands are less tilted resulting in a larger density of states. Since the density of states increases, the quantum efficiency also rises (figure 2.6) [PMD1].

Although, there are clear suggestions that growth with interruptions can suppress In segregation, there are still lack of research presenting optimization of growth with interruptions. Also there is lack of analysis how different growth parameters could influence growth process. That is the reason why we were keen to address this issue.

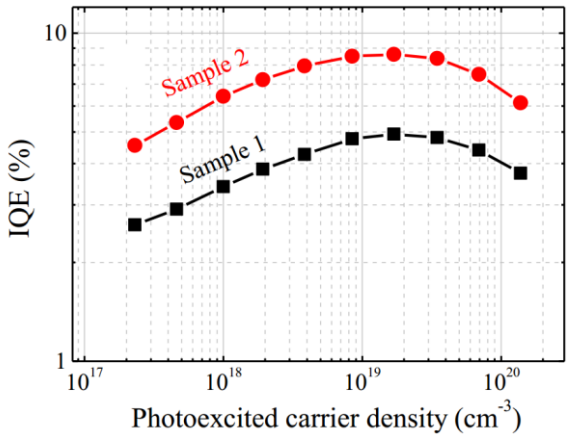

Figure 2.6 Internal quantum efficiencies. Sample 2 – pulsed grown sample (five 15s pulses, 5s pauses), Sample 1 – reference grown conventionally without MO interruptions [PMD1].

3 INSTRUMENTATION

3.1 Metal-Organic Vapor Phase Epitaxy

MOVPE is an epitaxial crystal growth technique for III-N semiconductors. The beginning of this technology is attributed to the pioneering works of Manasevit in the late 1960s. By 1971, Manasevit et. al. reported the first attempt to grow AlN and GaN using metalorganics [62]. Nowadays MOVPE is used for the growth of a single crystalline layer for a wide range of materials: II/VI, IV/VI and III/V [63].

Initially the development and use of MOVPE technologies was slow, yet the appearance of high performance devices in late 1970s such as the R. D. Dupuis AlGaAs/GaAs laser diodes (LD), R. R. Saxena et. al. solar cells and R. R. Bradley light emitting diodes (LED) [64-66], made the way for MOVPE to be seen as a suitable technology for commercial production and application. The quality of III-N as well as their optical and electrical properties were rapidly improved, especially after Amano et al. report on p-doping of GaN in 1989 [67], and Nakamura's report on GaN growth using GaN buffer layer [68].

The MOVPE technique is based on metalorganic precursor (MO) transport, decomposition and adsorption on a substrate surface. The main components of MOVPE reactors are: MO containers (called "bubblers"), gas lines, reactor chamber and exhaust system (see figure 3.1). The bubblers with liquid MO are kept within temperature controlled baths. The temperatures within these baths are controlled precisely to allow for the appropriate vapor pressure. Carrier gasses (H_2 or N_2) injected into the bubblers saturate with the MO and end up in the gas lines. Then saturated gasses can be diluted with H_2 or N_2 and passed to the reactor. The amount of injected carrier gas, gas dilution and output to the lines are precisely controlled by the mass flow controllers (MFC). The valves at the carrier line can quickly open or bypass the flow to the reactor chamber by directing gasses to exhaust.

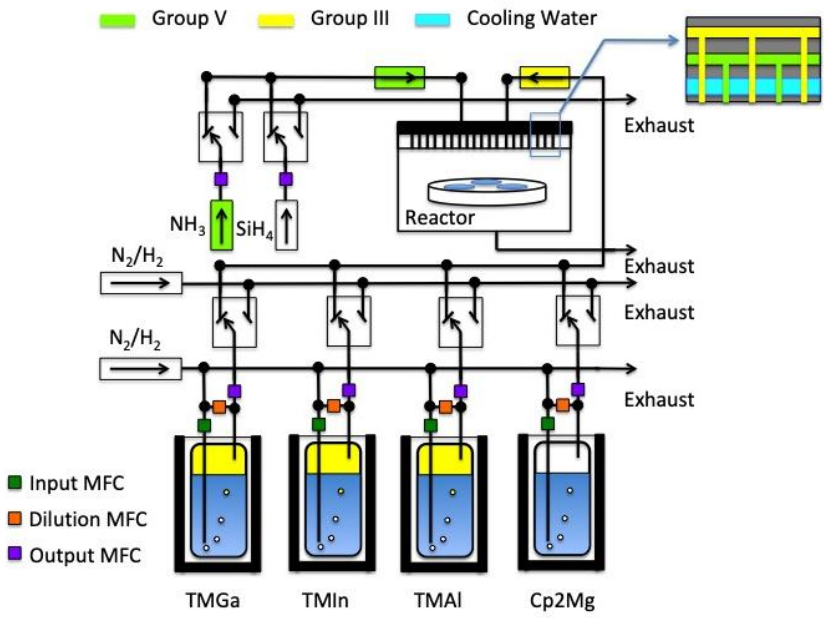

Figure 3.1. Scheme of a gas lines in CCS MOVPE.

The MOs that are used in the Vilnius University laboratory's MOVPE include Tri-Methyl-Gallium (TMGa), Tri-Methyl-Indium (TMIn), Tri-Methyl-Aluminum (TMAl) and Bis-Cyclopentadienyl-Magnesium (Cp_2Mg) as the source of Ga, In, Al and Mg respectively. The source of nitrogen and silicon are ammonia (NH_3) and Silane (SiH_4) respectively. The NH_3 and SiH_4 gas lines are separately controlled by the MFC and valves. To prevent gas prereactions the gases of V and III groups are injected separately into the reactor chamber through the close-coupled showerhead (CCS). CCS is the top lid of the reactor - a matrix with multiple small tubes (figure 3.2). To prevent gas decomposition before entering the reactor chamber, CCS is cooled with water, which helps to maintain the CCS temperature at ~50 ^{o}C. The CCS's close proximity (~10mm) to the substrate holder, also known as the susceptor, helps to prevent gas recirculation and ensure laminar flow of the gasses. Our MOVPE susceptor has three pockets for 2" substrates. At the surface of the hot susceptor gas molecules decompose and adsorb to the substrates and the susceptor. The susceptor is heated from beneath with a resistive heater. To reduce temperature and gas flow deviations in a circumferential direction, the susceptor rotates at a rate of 50-100 rpm. Unreacted or desorbed molecules are exhausted through the vent system, which maintains the desired chamber pressure in the range of 50-900 Torr.

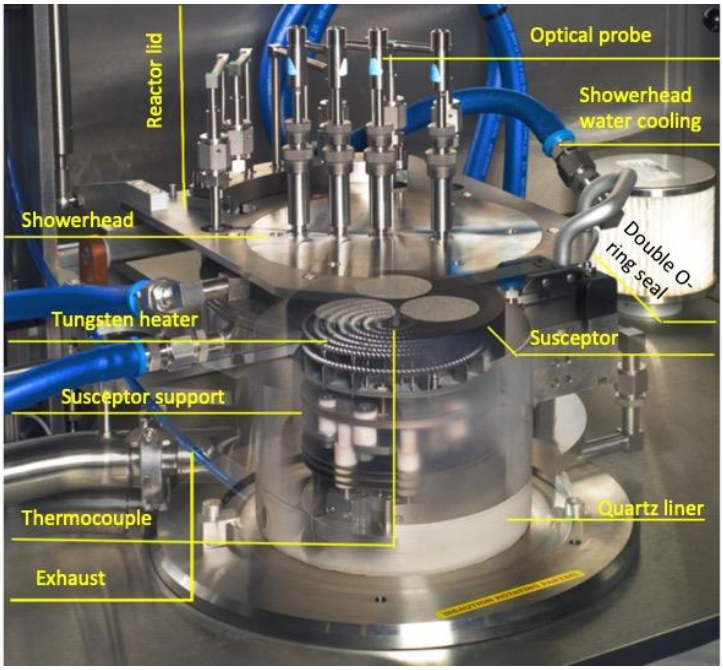

Figure 3.2. CCS MOVPE reactor, which was used in our experiments - a cross-section image. Copyright, owned by Aixtron; used by permission [69].

Thin film growth process is monitored in-situ by using reflectometer. By monitoring the reflection of a laser beam, the film surface empirical quality and growth stage, as well as thickness, can be deduced [70].

The reflectometer consists of a 660 nm laser diode (LD) and a four-detector matrix connected to two optical probes that are located on top of the reactor showerhead. The LD light, transmitted through the optical probe, reflects from the film surface and substrate/film interface, interferes and after transmission through the second optical probe is detected by the detector. The amplitude of reflected light depends on the film thickness *d*, which is related to the occurrence of constructive or destructive interference and film surface roughness, which scatters light and reduces the overall detected signal. The typical interferogram, acquired during the growth of GaN is presented in figure 3.3.

The reflectance from the sapphire surface marks the initial signal amplitude in interferogram. At the stage A-B nucleation of GaN begins and the signal amplitude increases up to the point B. The surface anneal follows at the temperature of 1000 ^{o}C, and the hexagonal GaN island formation occurs, which results in the rough surface and the amplitude of the signal decrease from stage B to C. Then, at point C, MO flow is introduced and islands begin to grow in size, resulting in rougher

surface (up to the point D). At point D, the island coalescence begins, which results in emerge of interference fluctuations. At point E coalescence finishes and 2D film growth begins.

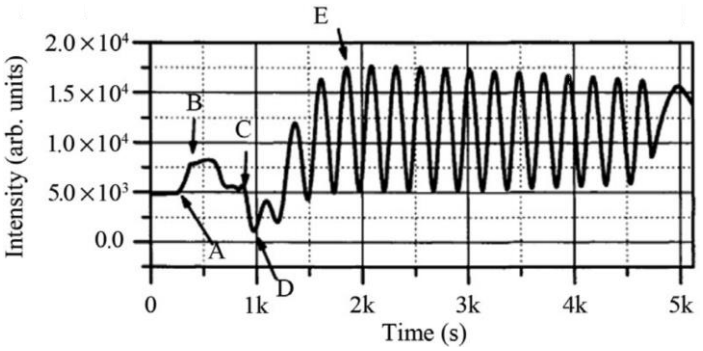

Figure 3.3. Typical interferogram acquired during the growth of GaN. Copyright, owned by T. Nishinaga; used by permission [71].

3.2 Structure Characterization Techniques

3.2.1 X-Ray Diffraction

X-Ray diffractometer (XRD) is a non-destructive instrument that is used to characterize material composition, structure and quality by measuring X-ray diffraction from a single crystal. The primary X-ray beam interacts with the sample's surface and diffracts. The diffraction of X-rays from the crystallographic planes occurs due to the primary X-ray excitation of lattice atoms and emission of secondary X-rays. Secondary X-rays interfere and create a diffraction pattern. The secondary X-rays can only be detected when they interfere constructively [72]. The constructive interference is achieved when the Bragg's diffraction condition is fulfilled (equation 3.1).

$$2d \sin\theta = n\lambda \tag{3.1}$$

Bragg's equation describes the relationship between the angle of a primary beam θ and the interplanar distance of crystallographic planes d. λ is the X-ray source wavelength and n is an integer that stands for the reflection order. The interplanar distance d can be calculated by measuring the angle at which the constructive interference of diffracted beam occurs. Figure 3.4 presents a scheme of X-ray diffraction from the crystal lattice. When the Brag's law is satisfied the

path difference between two scattered X-rays, denoted as 1' and 2', is equal to one wavelength and the path difference between 1' and 3' is equal to two wavelengths. All of the other diffracted X-rays from the atoms at all planes are considered to be in phase.

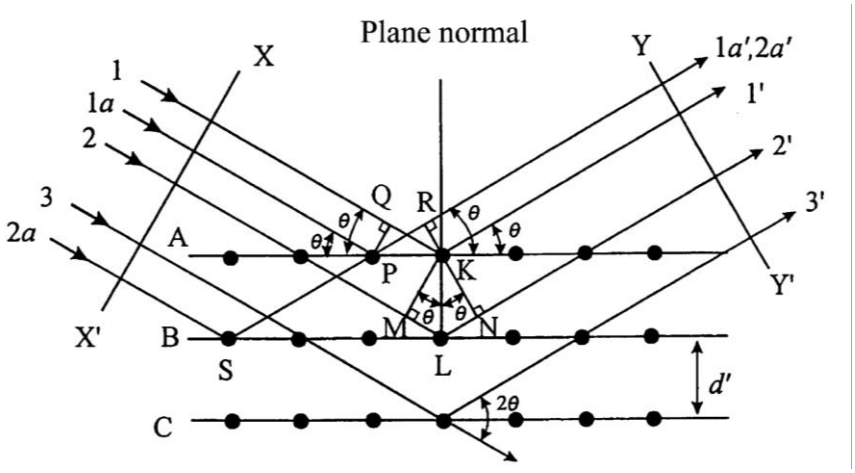

Figure 3.4. Schematic representation of X-ray diffraction by a crystal. Copyright, owned by Y. Waseda; used by permission [73].

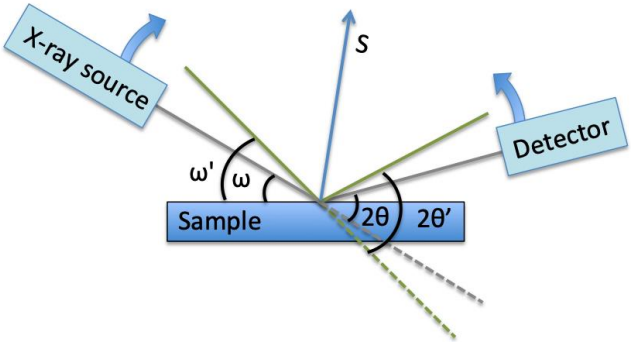

Figure 3.5. Schematic representation of XRD ω - 2Θ scan.

All XRD measurements in this work were conducted by using ω - 2Θ scan configuration, which is schematically presented in Figure 3.5. When the crystal planes are not parallel to the sample's surface the angle between the incident beam and the sample surface (ω) differs from the Θ. In this case, the offset angle between incident beam and sample surface has to be found at which the incident beam is

parallel to the crystal planes. Additionally, the scan interval of (ω-ω') and (2Θ-$2\Theta'$) has to be chosen. Usually during the III-N ω - 2Θ scan the reflections of the (004) planes are registered. During the scanning, the X-ray source and the detector move towards each other at the same speed to maintain the same direction of the scatter vector $\boldsymbol{S}$.

The XRD diffractometer used in our research was "*Rigaku, SmartLab*". XRD consists of three main components: X-ray source, goniometer with sample holder and X-ray detector. The X-rays are generated as follows: heated cathode tube emits electrons that are accelerated by the 9kV voltage toward the copper target, where they are absorbed and emit the white X-rays spectra. The characteristic line of $K_{\alpha 1}$ λ= 1.56054 Å is filtered by germanium crystal monochromators and directed towards the sample. The sample is fixed on the sample holder that is mounted on the goniometer, which can be rotated in all directions to set certain diffraction condition. The scintillation detector (*SC - 70*) is used to detect diffracted X-rays from the sample. The measured data in our research was analyzed using *GlobalFit* software.

3.2.2 Reciprocal Space Mapping

The chemical composition of InGaN films is usually estimated from the peak position of XRD (00*l*) reflection in ω - 2Θ scan, by applying Vegard's law. However, for the greater accuracy of In content and to get further details about the lattice, the influences of strain and composition must be separated and analyzed quantitatively through reciprocal space mapping (RSM). The RSM is the crystal lattice Furje transformation, where each point corresponds to the set of crystal planes. Directions in the RSM are the same as in the real space, while the distances are inverted [74].

The reciprocal lattice is constructed by choosing an origin and drawing a vector $\boldsymbol{S}$ (scattering vector) in a direction of the plane normal of a specific set of the crystallographic planes. At the tip of the vector $\boldsymbol{S}$ a point of a specific set of the crystal planes is plotted. The $\boldsymbol{S}$ magnitude is equal to 1/*d*, where *d* is an interplanar spacing. The $\boldsymbol{S}$ is changed by choosing the angle ω of the incident beam. The RSM is obtained by taking a series of ω–2θ scans and presenting measured results in the map form.

Usually, to determine which lattice planes will create a diffraction signal for an incident beam wavelength λ, the Ewald's sphere is constructed (figure 3.6). The radius of Ewald's sphere is the incident beam vector $\boldsymbol{k_0}$ and the radius length is 1/λ. During the elastic diffraction (no energy is gained or lost), the incident beam vector

$\boldsymbol{k_0}$ is equal to the diffracted beam vector $\boldsymbol{k_h}$ with a length of $1/\lambda$. The difference of a $\boldsymbol{k_0}$ and $\boldsymbol{k_h}$ is equal to $\boldsymbol{S}$, which lays (touches) the sphere's surface. Thus, for the diffraction from a specific set of planes to occur, the reciprocal lattice points has to lay on the surface of Ewald's sphere.

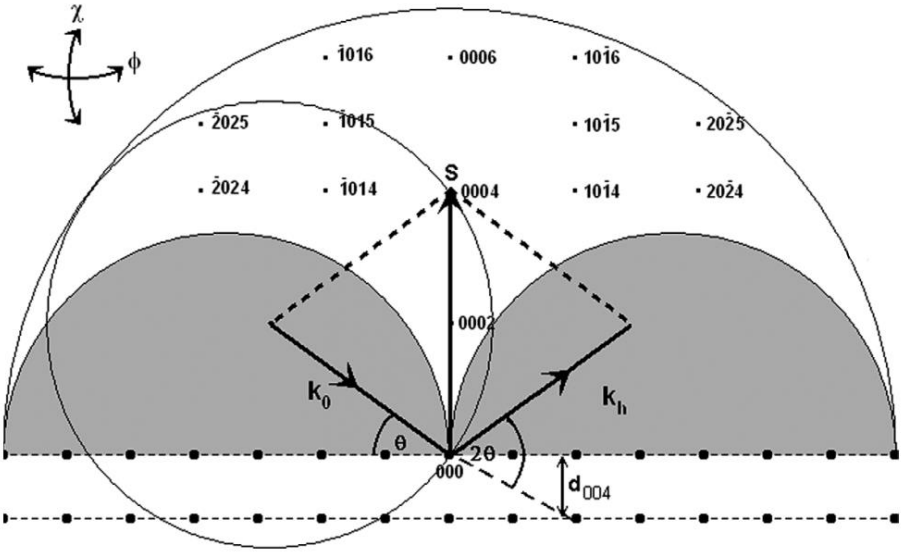

Figure 3.6. A reciprocal space representation of a [0 0 0 1]-oriented GaN film. The Ewald sphere is shown as a circle, cutting the 0004 reciprocal lattice spot. The vector $\boldsymbol{S}$ is perpendicular to the (0004) plane and has a length of $1/d_{0004}$. Reciprocal space regions, where the sample blocks the beam, are inaccessible (shown in grey). Some spots are absent because they have zero intensity. The large ('diffractometer') circle shows the outer limit which can be reached with $\boldsymbol{S}$ for a given λ and maximum θ. Copyright, owned by M. A. Moram; used by permission [72].

RSMs are typically used to facilitate the interpretation of XRD peak position, peak broadening or peak overlap. RSM helps to summarize the information about the interplanar spacing and defect related broadenings.

The peak position is sensitive to epitaxial layer strains, because layer relaxation is usually accompanied by the layer tilting that results in XRD peak displacement. Also, the sharp diffraction spots are not common. Usually, the diffraction spots in reciprocal space are broadened by the microstructural defects, macroscopic size and shape of the sample (for example wafer bending), and the instrumental resolution. The spot broadening in reciprocal space can occur due to the different types of defects: lattice tilt, twist, small-scale strain (microstrains) and

composition/strain gradients. Microstrains are usually created by dislocations. The degree of relaxation is defined by the expression 3.2:

$$R = \frac{a(L) - a_0(s)}{a_0(L) - a_0(s)} \tag{3.2}$$

Where $a(L)$ and $a_0(L)$ are the relaxed and measured in-plane lattice parameters of the InGaN layer, and $a_0(s)$ is the GaN template lattice parameter.

3.2.3 Transmission Electron Microscope

The Transmission electron microscope (TEM) is an instrument, which images a crystal and measures its properties by registering the transmitted electron beam (ebeam) [75]. The main feature of TEM is that it can be set to an atomic size resolution – up to 0.1 nm [76]. The resolution of TEM is limited by the electron de Broglie wavelength (λ) and ebeam aberrations. λ depends on the electron acceleration voltage, as it is demonstrated in the equation 3.3 [77], where h is Planck's constant, e is the charge of an electron, m_0 is the rest mass of an electron, c is the speed of light and U_0 is the ebeam accelerating voltage which in our measurements was 200kV.

$$\lambda = \frac{h}{\sqrt{eU_0\left(2m_0 + \frac{eU_0}{c^2}\right)}} \tag{3.3}$$

TEM operation principles are as follows: the electron gun, that produces an ebeam, is enclosed in the high vacuum chamber and connects with the specimen stage and the detector. The ebeam is created by emitting electrons from the heated cathode and accelerating them towards the anode. In order for the ebeam to penetrate the sample, the ebeam's energy has to be in the order of hundreds of keV. Also the sample has to be relatively thin (5-100nm). Before reaching the sample, the ebeam is aligned with the electromagnetic (EM) condenser lenses. In addition, the EM coils are used to scan the ebeam across the sample's surface area during the raster TEM scan (STEM) operation. After the ebeam interaction and transmission through the material, the ebeam passes through the objective and projector EM lenses and is picked up by the detector. During TEM operation it is possible to apply different configurations to the specimen probe. Varying the configuration one can gather different information, such as: electron diffraction, X-ray emission

or simply specimen imaging. During this work, the *FEI Tecnai G2 F20 X-TWIN* instrument was used in STEM operation to acquire the samples' images.

3.2.4 Atomic Force Microscopy

Atomic force microscopy (AFM) is a surface probing technique. It is used to acquire high-resolution image with nanometer resolution of a surface morphology and to calculate surface roughness (mean surface height deviation). The principle of AFM operation is based on a sharp tip's interaction with the sample's surface. The interaction is between neutral atoms or molecules and it can be described using *Lennard-Jones* model [78, 79]. This model describes the equilibrium between *Van der Waals* attraction between two dipoles and the Pauli repulsion force due to overlapping electron orbitals. The interaction can be empirically expressed through the *Lennard-Jones* potential:

$$U(r) = U_0 \left[\left(\frac{r_0}{r} \right)^{12} - 2 \left(\frac{r_0}{r} \right)^{6} \right] \tag{3.4}$$

Here r is the distance between two particles; r_0 is the distance at which the potential reaches its minimum; U_0 is the depth of the potential well. The positive aspect of the equation describes the repulsion between two particles and the negative aspect represents the attraction. The potential is represented in figure 3.7.

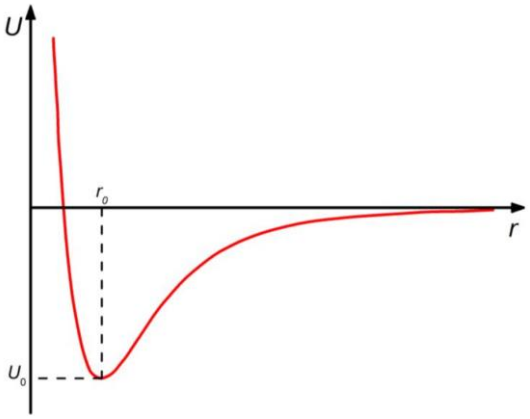

Figure 3.7. Lennard Jones potential [80].

The tip is attached to the flexible cantilever – see figure 3.8. When the sample is moved in a lateral direction with respect to the tip, the van der Waals forces

between the sample surface and the tip bends the cantilever. The angle of the bent cantilever is measured by the laser beam reflection from the cantilever surface, and the beam is registered by the sensitive photo-detector. The sample is moved and scanned in a raster manner. The method is nondestructive and fast, because AFM can be operated in air and room temperature, and the sample preparation is simple.

The *Witec Alpha 300* model was used in AFM research. This type of AFM operates in contact mode. Contact mode is one of a number of possible AFM configurations, whose operation is based on the tip dragging over the sample surface.

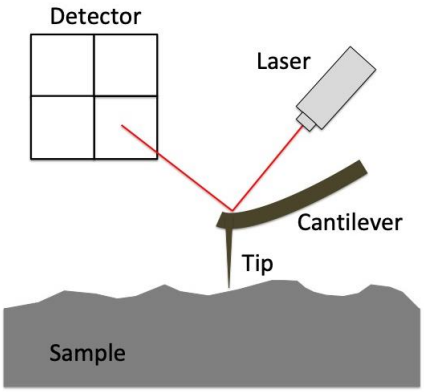

Figure 3.8. Schematic illustration of AFM measurement process.

3.3 Optical Characterization Techniques

3.3.1 Photoluminescence

The room temperature (RT) PL spectra were measured using lab equipment. The excitation source was a continuous wave laser diode (405nm) (10mW, 4 W/cm^2) and the luminescence was collected with *Princeton Instruments Acton SP2300* spectrometer and analyzed with a *Pixis 256* CCD camera.

3.3.2 Temperature Dependent Photoluminescence

The temperature dependent photoluminescence was measured under steady-state excitation conditions. Measurements were performed in the temperature range from 8 to 300 K, which was controled by the closed-cycle helium cryostat. Samples were excited by CW He-Cd laser (λ_{exc}=325 nm). The luminescence was

collected by the double monochromator (*Jobin Yvon HRD-1*) and detected by the photomultiplier (*Hamamatsu*).

3.3.3 Spatially-Resolved Photoluminescence

The spatially-resolved photoluminescence (μPL) measurements were conducted using scanning confocal microscopy. The confocal microscopy has several advantages over the conventional optical microscopy, whereas the main advantage is that it gives shallow depth of field and eliminates out of focus emission [81]. Also, by scanning at different focal planes there is a possibility to collect several optical sections and to create a three dimensional image of the sample.

The configuration of confocal microscope is presented in figure 3.9. The excitation beam focused with the objective illuminates the small spot at the focal plane. Using the same objective the luminescence is collected and reflected by the beam splitter. Finally, the beam is focused to the detector. Before entering the detector, it passes the small aperture, which eliminates the off-focal plane light that results in a sharper resolution and improved contrast of the image. The area of sample that is chosen for measurement is scanned point by point in a raster manner.

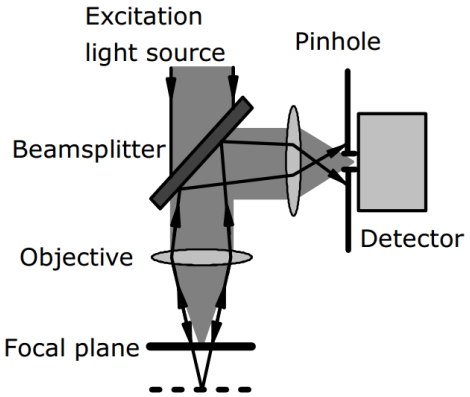

Figure 3.9. The schematic representation of the confocal microscope. Copyright, owned by D. Dobrovolskis; used by permission [82].

In this work the μPL study was performed with the *Witec Alpha 300* microscopy system at the room temperature. Laser diode (λ_{exc}=405 nm) was used as an excitation source. Laser beam was focused into a spot of ~300nm in diameter. Penetration depth was ~2μm, thus all QWs were excited. The spectrometer *UHTS 300*, used to record PL spectra was equipped with a thermo-electrically cooled CCD camera.

4 PULSED GROWTH OF InGaN MQWs

The InGaN MQWs were grown on a sapphire substrate using the MOVPE *AIXTRON* 3 × 2″ closed-coupled showerhead reactor. The sample structure is presented in figure 4.1. Samples consisted of: GaN buffer layer, AlGaN superlattice (SL), InGaN SL, InGaN QWs surrounded by GaN QBs and a GaN cap layer. Trimethylgallium (TMGa), trimethylindium (TMIn), Trimethylaluminum (TMAl) and ammonia were used as Ga, In, Al and N precursors, respectively. H_2 was used as the ambient and carrier gas during the growth of unintentionally doped GaN (uGaN) layer and AlGaN SL. N_2 was used as the ambient and carrier gas during the growth of InGaN SL and InGaN MQW.

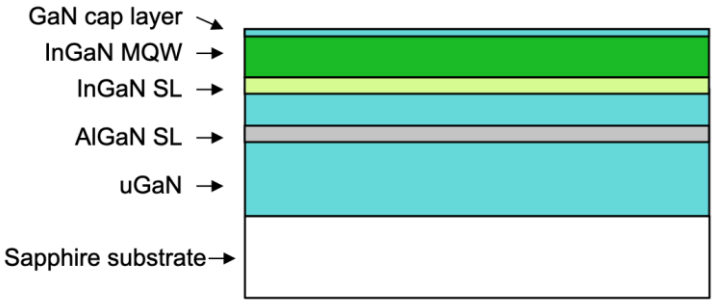

Figure 4.1. The crystal's layers structure of the sample.

Initially the 2µm uGaN (3 µm for the green set of samples) layer was grown at 1070 ^{o}C and 150 mBar reactor pressure. TMGa flow was 1.636×10^{-4} mol/min and NH_3 flow was 2.232×10^{-1} mol/min, with V/III ratio of 1.364×10^{3}. The AlGaN/GaN SL (further AlGaN SL) was buried inside the uGaN layer. The AlGaN SL is a periodic structure of thin (~2nm) AlGaN and GaN layers. The use of AlGaN SL can improve the material characteristics. Wang et. al. have shown, that AlGaN SL reduces the TD density, which is attributed to the strain relaxation inside SL [83]. It is usually buried inside the buffer GaN layer after the GaN has coalesced (at ~1.5 µm of uGaN). We have previously used different structures of SL and found that the best results are achieved when 5 periods AlGaN SL are used with a total thickness of 12.5nm and mean Al concentration in AlN/AlGaN of 25%. The measured carrier mobility of 3.5 µm uGaN without AlGaN SL was 100 $cm^2/V \times s$ and by incorporation AlGaN SL carrier mobility increased up to 265 $cm^2/V \times s$. The carrier concentration for uGaN without SL was 1.5×10^{18} cm^{-2} and with SL carrier concentration decreased to 5×10^{17} cm^{-2}. The AlGaN SL used in our samples was grown at 1075 ^{o}C with the reactor pressure of 150 mBar, TMAl flow was

5.729×10^{-6} mol/min, TMGa flow 2.1×10^{-5} mol/min and NH_3 flow 4.0×10^{-2} mol/min with III/V ratio of 1.491×10^{3}.

Further, the buffer layer growth was followed by the growth of InGaN/GaN SL. The InGaN/GaN SL (further InGaN SL) is a periodic thin layer InGaN and GaN structure (thickness of one period 1÷8 nm) that is used as a lattice mismatch buffer layer between the underlying uGaN and MQW layer. The InGaN SL can substantially improve the MQW characteristics, especially for the green MQW [84], [PMD1]. There have been many debates trying to define the true benefit of InGaN SL. It was commonly accepted, that the major role of InGaN SL is that it releases the residual strain in the MQW layer by shifting the lattice constant to the average value of the MQW region [85, 86]. Jia et. al. reported, that the insertion of the InGaN SL reduced the strain in InGaN MQW by 12.5% that results in a polarization field reduction as well as an increase in carrier overlap from 14% to 19% [48]. Also, SL helps to reduce V-pit density. According to Jia et. al. the V-pit density in InGaN MQWs with insertion of InGaN SL decreased from $4\text{-}5\times10^{8}cm^{-2}$ to $2\text{-}4\times10^{7}cm^{-2}$. In addition, InGaN SL is advantageous for the LED structure, because it can act as an electron reservoir and enhance the electron capture rate in the InGaN MQW as well as increase the EL up to 3 times [87].

Recent studies have proposed that the major role of InGaN SL is a significant reduction in the concentration of surface defects (SD) [88]. During the GaN growth not only dislocations are created, but point defects as well, such as vacancies or impurities. It is likely that the vacancies create SD, because it tends to diffuse towards the surface.

Further, point defects tend to segregate at the GaN surface or in the region near the surface creating a point defect reservoir. Such point defects strongly interact with In atoms, and are buried in InGaN layer, where they create a NRC [89, 90].

When no InGaN SL or underlayer (UL) is used, the SDs are incorporated into the InGaN MQW directly, thus hindering the quality of MQW. On the other hand, if the In containing layer (either InGaN UL or InGaN SL) is inserted before the MQW, it can significantly reduce the SD concentration inside the MQW. As mentioned before, InGaN SL has a benefit over the InGaN UL, because it adjust lattice constant closer to the average lattice constant of InGaN MQWs. Although, SL is composed of thin layers (few nm), which cannot be grown with all types of MOVPE reactors. Not all systems are able to address abrupt growth changes which leaves only one option – to use InGaN UL. Our MOVPE reactor is equipped with a relatively small close coupled showerhead, which is suitable for the growth of SL.

The GaN/InGaN SL growth temperature for each sample was set depending on the MQW growth temperature (see table 4.1). Reactor pressure during the InGaN SL growth was 400 mBar, NH_3 flow was 2.679×10^{-1} mol/min, TMG flow

3.191×10^{-6} mol/min, TMIn flow 7.222×10^{-6} mol/min, SiH_4 flow was 2.679×10^{-8} mol/min and the ratio of V/III was 2.572×10^{4}. During the growth of InGaN SL flow of TMG and NH_3 were constant, where the TMIn flow was periodically interrupted to switch between the InGaN and GaN layers. The SL structure consisted of 8 periods of InGaN and GaN layers with the total SL thickness of 24 nm and In concentration in InGaN layer of 5%. The thickness of each layer had to be relatively similar, because the growth time for the InGaN layer was 85s and for the GaN layer 90s.

GaN/InGaN SL was slightly doped with Si. It was shown that SL doping reduce dislocation density up to 2 times [91]. This effect is associated with a Si induced dislocation bending. Thus, in-plane stresses are relaxed, which reduce QCSE.

After the last GaN SL layer, the flow of MOs were shot, until the temperature and sources were adjusted for the growth of InGaN MQWs. Then growth of five period InGaN MQW was initiated by the growth of first QW.

The GaN/InGaN MQWs doped with Si were grown using a pulsed growth technique. The pulsed growth for InGaN QW layer was conducted by modulating the flow of TMIn, TMGa and SiH_4 precursors into the reactor chamber, while maintaining the flow of ammonia constant (see figure 4.2) [25]. The MO precursor pulse duration t_1 was modulated from 20 to 5s, the pause duration t_2 from 3 to 20 s, the number of pulses from 5 to 20. A summary of the pulsed growth parameters is given in the table 4.1.

The QWs in the two main sets of samples were grown at 780 °C and 800 °C temperature. Additional two sets of samples were grown at 810 °C and 830 °C. During the growth of QWs, NH_3 flow was 2.679×10^{-1} mol/min, TMGa flow 3.191×10^{-6} mol/min, TMIn flow 9.028×10^{-6} mol/min, SiH_4 flow was 2.679×10^{-8} mol/min and the ratio of V/III was 2.192×10^{4}.

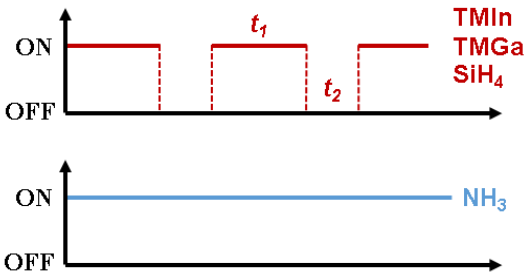

Figure 4.2. Timing of TMIn and TMGa precursors flow during pulse growth.

Table 4.1. Parameters of the InGaN/GaN MQWs pulse growth.

Sample	t_1,s	t_2,s	Pulses	T_{QW},°C	T_{QB},°C	T_{SL},°C
S1(ref.)	80	0	1	800	840	850
S2	20	3	5	800	840	850
S3	20	6	5	800	840	850
S4	20	9	5	800	840	850
S5	20	12	5	800	840	850
S6	20	15	5	800	840	850
S7(ref.)	80	0	1	780	850	860
S8	5	3	20	780	850	860
S9	5	6	20	780	850	860
S10	5	9	20	780	850	860
S11	5	12	20	780	850	860
S12	5	15	20	780	850	860
S13	10	3	10	780	850	860
S14	10	6	10	780	850	860
S15	10	9	10	780	850	860
S16	10	12	10	780	850	860
S17	10	15	10	780	850	860
S18	20	3	5	780	850	860
S19	20	6	5	780	850	860
S20	20	9	5	780	850	860
S21	20	12	5	780	850	860
S22	20	15	5	780	850	860
S23(ref.)	80	0	1	810	850	860
S24	20	3	5	810	850	860
S25	20	6	5	810	850	860
S26	20	9	5	810	850	860
S27	20	12	5	810	850	860
S28	20	15	5	810	850	860
S29	20	20	5	810	850	860
S30(ref.)	80	0	1	830	870	880
S31	20	3	5	830	870	880
S32	20	6	5	830	870	880
S33	20	9	5	830	870	880
S34	20	12	5	830	870	880
S35	20	15	5	830	870	880
S36(ref.)	80	0	1	790	860	870

Right after the InGaN QW growth ~1nm GaN cap layer was deposited to prevent In decomposition during the temperature ramp to GaN QB growth

temperature. During the temperature ramp, crystal growth was terminated by switching TMGa and SiH_4 flow off.

Previos studies have shown that MQW efficiency can be slightly enhanced by Si-doping QWs [92]. The improvement is mainly related with increased crystal quality of InGaN layer due to reduced compressive stress and defect concentration as Si atoms can be occupied at the point defects and supress them [93, 94].

QB doping has several advantages as well. First of all, GaN Si-doping leads to growth mode transition from step-flow to layer-by-layer growth mode. There are several posible explanations for such behavior, although the most likely is that Si atoms initiate production of preferential sites for island nucleation between the steps [95]. A change in the growth mode results in increased abruptness of the interfaces between the barrier and well, which reduce In-composition fluctuation in InGaN QW [96]. Also, Si doping in barrier layers create excess electrons, which enhances the Coulomb screening of QCSE [97].

QBs growth temperature was between 840 °C and 870 °C (see table 4.1). During the QB growth NH_3 flow was 2.679×10^{-1} mol/min, TMGa flow 3.023×10^{-5} mol/min, SiH_4 flow was 2.5×10^{-7} mol/min and the ratio of V/III was 8.861×10^{3}.

For comparison, five reference samples (S7, S36, S1, S23, S30) were grown conventionally without flow interruptions with QW growth temperatures of T_{growth} = 780, 790, 800, 810 and 830 °C respectively. All structures were finished with a thin (25-30 nm) GaN capping layers on top of the active layers.

5 STRUCTURAL AND PHYSICAL PROPERTIES OF PULSED GROWN InGaN MQWs

5.1 Structural Analysis of InGaN/GaN Multiple Quantum Wells

Initially, PL was measured for all samples, grown by the pulsed mode, to find the samples with the highest PL intensity for further structural investigation. The sets of samples grown with the t_1=20s pulses possessed highest PL intensity with the peak position in cyan color region (for the set of samples grown at T_{growth}=800 ^{o}C) and in green color region (for the set of samples grown at T_{growth}=780 ^{o}C). Further in this text for simplicity the S1-S6 set of samples will be regarded as "cyan set" and the set S7, S18-S22 will be regarded as "green set". Cyan and green sets were chosen for further structural investigation.

The TEM measurements were made for the samples S7 and S21 from the green set (figure 5.1). The estimated thickness of the QW and QB for the reference varied in the range of 1.6÷1.7 nm and 6.2÷7.9 nm, respectively. The calculated QW growth speed was 0.021 nm/s. The thickness of the QW grown in the pulsed mode was 1.8÷1.9 nm, which is similar to the thickness of reference QW. The QW growth speed was 0.019nm/s if only the pulses were considered and the QW growth speed was 0.012nm/s, if the time of pulses and the pauses were considered. A slight difference in the QW growth speed can be related to the MO switching conditions. In general, the growth speed during the pulsed growth is more sensitive to the growth temperature and pressure, especially when the pauses are longer. A higher interruption time enhances In and Ga desorption from the InGaN and decreases the growth speed substantially. The InGaN lattice constant depends on In concentration and is between 5.1850 Å (GaN) and 5.7033 Å (InN) [98]. Although a slight increase in the lattice constant is possible due to the biaxial strain in the InGaN QWs on GaN. If the growth speed was around 0.02 nm/s, more than 1 crystal monolayer was expected to grow during one t_1=20s pulse. Whereas for t_1=10s or t_1=5s pulse less than one monolayer was expected to grow during one cycle.

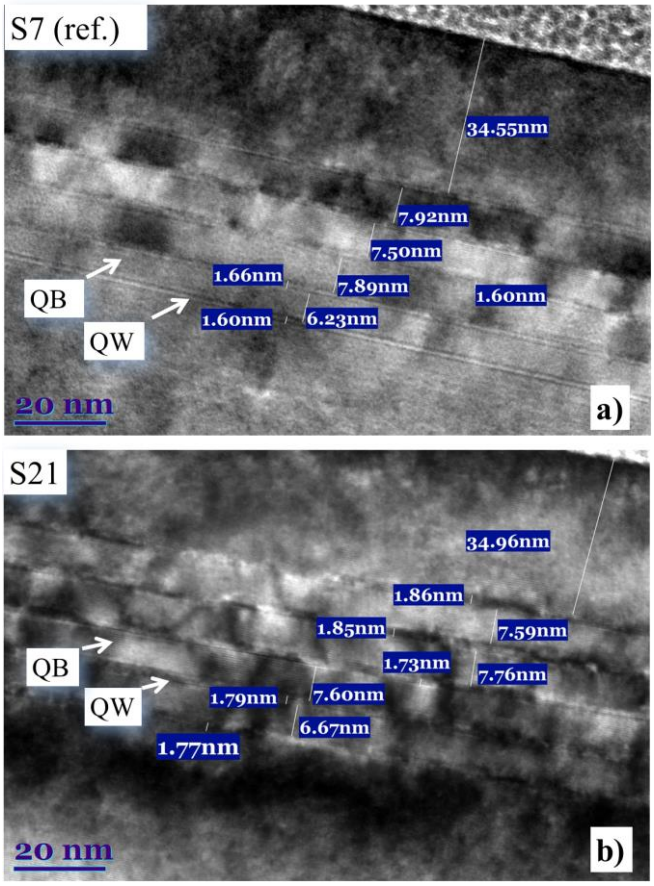

Figure 5.1. TEM pictures of: a) S7 reference sample and b) S21 sample grown by the pulse mode [PMD2].

STEM was measured for all cyan set of samples except for the sample S3 (see figure 5.2). STEM results for the samples S2 (3s pause) and S4 (9s pause) were similar, thus for economic reasons TEM was not measured for the sample S3 (6s pause). One can see in figure 5.2 that MQW and SL structures can be clearly seen in S2 and S5 samples. The S1, S4 and S6 have lower quality images, although MQW and SL can still be distinguished. The lower quality of images is not due to a lower crystal structure quality, but inherent to the measurement itself. The QW and QB thicknesses were calculated from these measurements and are presented in the table 5.1. Most noticeable, the QW thicknesses for the cyan set of samples have almost doubled if compared to the green set. As a result, 2 to 4 monolayers of InGaN were expected to grow during one t_1=20s pulse.

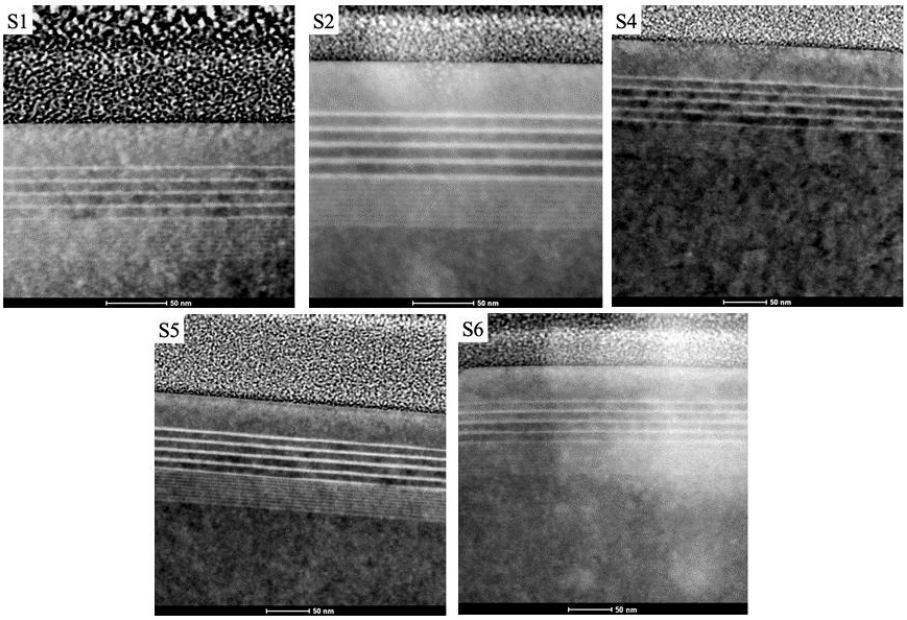

Figure 5.2. STEM images of reference (S1) and samples grown in pulsed regime (S2, S4, S5, S6).

Further, composition of samples was determined by measuring X-ray diffraction XRD. Figure 5.3 shows the MQWs ω − 2θ XRD scan from the (0002) plane of green samples and figure 5.4 presents the scans of the cyan set of samples. One can see, that the diffraction peaks, corresponding to the uGaN layer and InGaN/GaN MQWs are clearly expressed for both set of samples. Also, satellite peaks are resolved up to the minus fourth order and confirm the well-defined

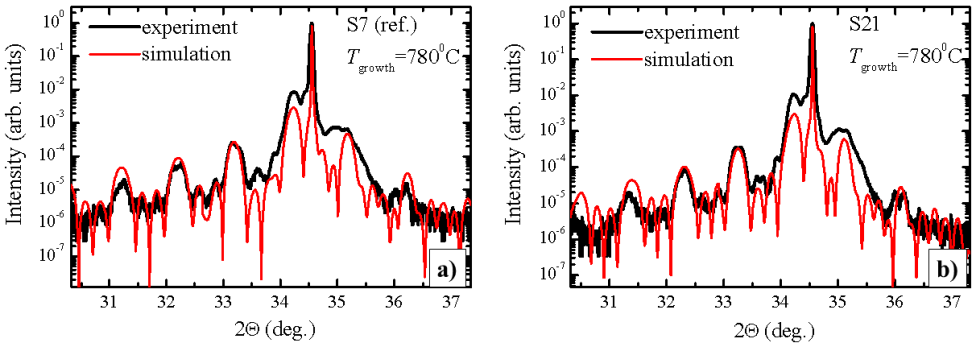

Figure 5.3. XRD scan of: a) S7 reference sample and b) S21 sample grown by the pulse mode [PMD2].

interfaces for the structure. By applying layer thicknesses measured with TEM, the In concentration in the SLs (X_{SL}) and in the QWs (X_{QW}) were calculated and presented in the table 5.1 (In concentration in QWs was later specified by measuring RSM).

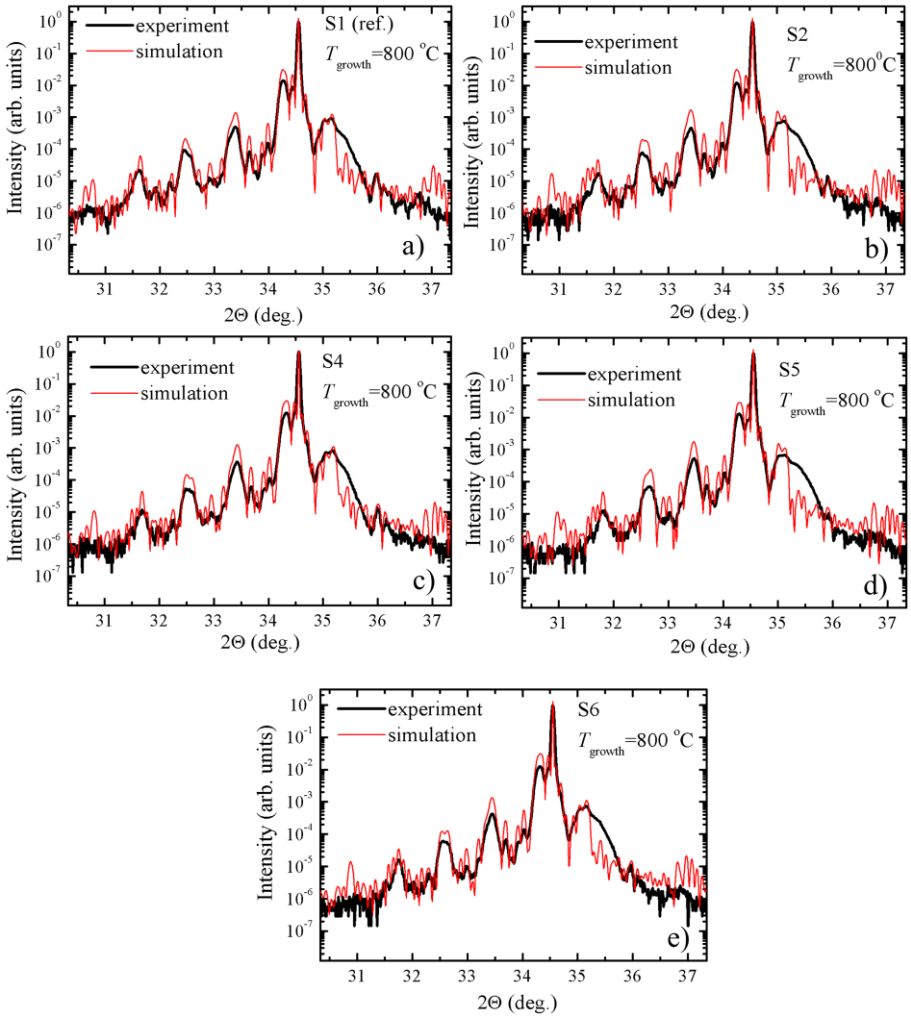

Figure 5.4. XRD rocking curves of the S1-S6 samples (a) – e) respectively).

The strains and In concentration in the MQW were evaluated by mapping reciprocal space (RSM) around the (105) reflection [72]. Figure 5.5 shows RSMs of pulsed grown and reference samples. One can see, in figure a) that the MQW peak reflections are shifted along the q_x axis from the main GaN peak (dash-dotted line). It represents the fact, that the InGaN MQW structure on a GaN template is no

longer coherently strained because it has slightly relaxed to accommodate the lattice constant difference [99]. As previously noted, lattice relaxation results in a slight tilt of a crystal as well as RSM peaks' displacement. The RSM of the sample S21 shows, that it has no lattice relaxation - the RSM peak of InGaN is vertically aligned with the GaN peak. Thus, by using pulsed growth technique fully strained InGaN MQWs were grown.

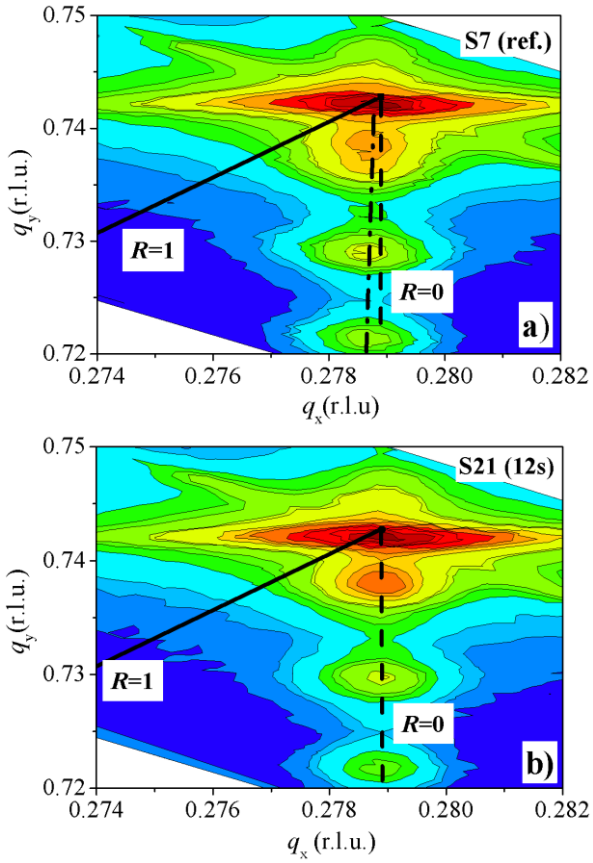

Figure 5.5. RSM around the (105) reflection of: a) S7 reference sample and b) S21 sample grown by the pulse mode. The dashed lines, passing through the GaN template reciprocal lattice points correspond to the fully strained (R = 0) state and solid lines corresponds to the fully relaxed (R = 1) state. The dash dotted line, in the image a) corresponds to a partially relaxed state [PMD2].

The average MQW lattice constants a and c were calculated by using equation (5.1) and (5.2) respectively.

$$a_{MQW} = \frac{\lambda}{\sqrt{3q_x}} \tag{5.1}$$

$$c_{MQW} = \frac{5\lambda}{2q_z} \tag{5.2}$$

Here λ is wavelength of the X-ray source (0.15406nm), and q_x and q_z are the reciprocal lattice points from the (105) reflection of MQW zero order peak. The relaxed GaN and InN lattice constants and Poisson ratios were: c_{GaN} = 5.1850 Å, a_{GaN} = 3.1892 Å, v_{GaN} = 0.2 and c_{InN} = 5.7033 Å, a_{InN} = 3.5378 Å, v_{InN} = 0.29 respectively.

The In concentrations, measured from the RSM mappings in the samples S7 and S21 were 27% and 20% respectively. The higher In concentration in the conventionally grown QWs (S7) compared to the pulsed grown sample (S21), may be related to the gradual strain relaxation through the defect formation, that facilitated In incorporation [100, 101]. On the other hand, lower In concentration in pulsed grown sample may be associated with the increased desorption of In during the MO flow interruption, which was presented in the previous studies of InGaN without cap layer annealing [102, 103].

Next, RSM was measured for the cyan set. RSM images of S1, S4 and S5 samples are presented in figure 5.6. It can be observed, that all samples were fully or almost fully strained - RSM reflections are aligned on the vertical *R*=0 line. In concentration values calculated in cyan QWs are presented in the 5.1 table. One can see, that with the growth temperature increase as for the cyan set of samples, the difference between In concentration of the samples decrease. Thus, the MQW In concentration sensitivity to the pulsed growth technique increases only, when the growth temperature is reduced.

Table 5.1. Layer thicknesses and In concentration in the reference and pulsed grown samples.

Sample	**S1**	**S2**	**S4**	**S5**	**S6**	**S7**	**S21**
d_{cap}, **nm**	28	28	28	28.5	28.5	34.5	35
d_{QB}, **nm**	6.6	6.7	7.2	6.7	6.8	7.4	7.4
d_{QW}, **nm**	3.8	4.1	3.8	4.1	4.1	1.6	1.8
$d_{InGaN\ SL}$, **nm**	1.8	1.8	1.85	1.85	1.85	1.8	1.8
$d_{GaN\ SL}$, **nm**	1.5	1.55	1.5	1.6	1.6	1.6	1.6
In X_{QW}	10.5%	10.5%	9.5%	10.0%	9.0%	27%	20%
In X_{SL}	5%	5%	4%	4%	4%	4%	4%

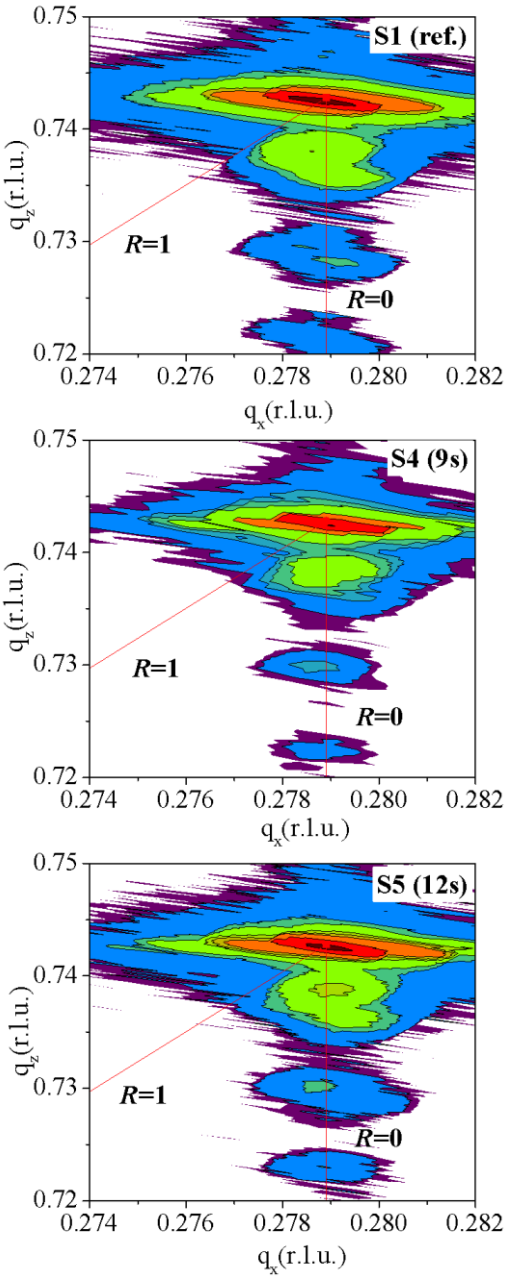

Figure 5.6. RSM around the (105) reflection of: S1 reference sample, S4 and S5 samples. The vertical lines, passing through the GaN template reciprocal lattice points correspond to the fully strained (R = 0) state and the inclined lines correspond to the fully relaxed (R = 1) state.

Further, AFM images were measured. Surface roughness and V-pit densities were evaluated from these measurements. AFM images of conventionally and pulsed grown samples of the green and cyan sets are presented in figures 5.7 and 5.8 respectively. The area root-mean-square (RMS) roughness was calculated and

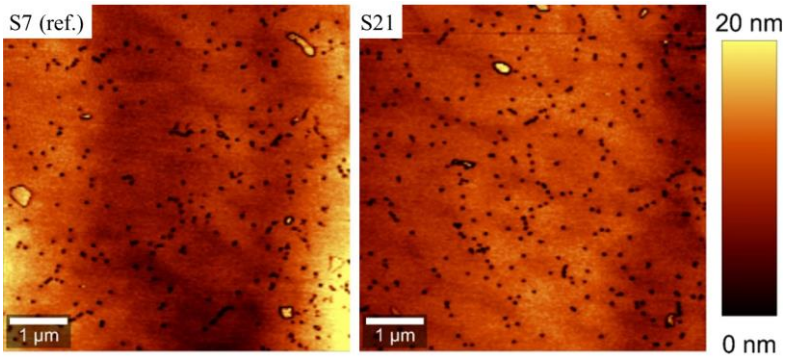

Figure 5.7. AFM images of green set reference (S7) and pulsed grown sample (S21). Dark color pits are regarded as V-shaped defects, bright spots contoured in black – as trench defects. The scan area is 6 × 6 μm^2 [PMD2].

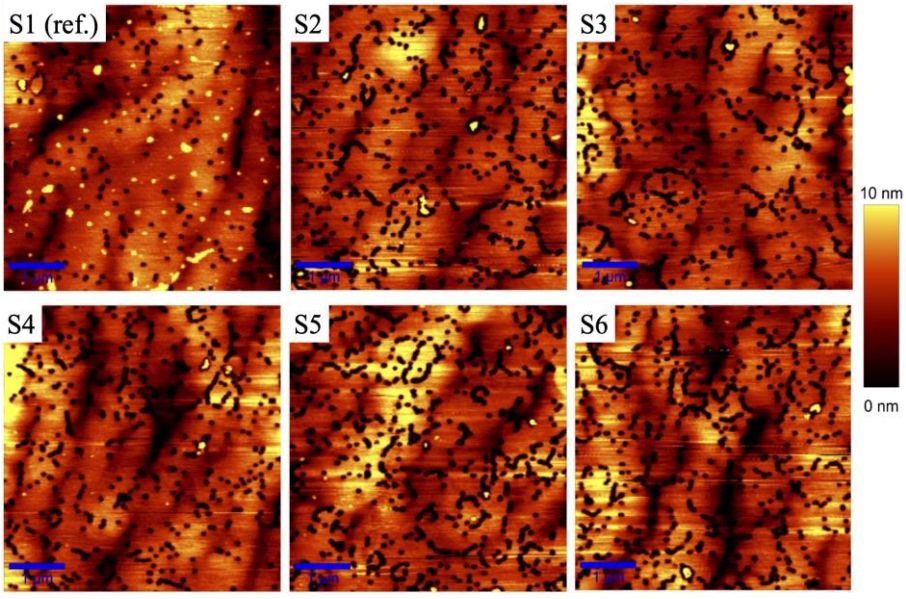

Figure 5.8. AFM images of cyan set reference (S1) and pulsed grown samples (S2-S6). Dark color pits are regarded as V-shaped defects, bright spots contoured in black – as trench defects. The scan area is 6 × 6 μm^2.

is presented in the table 5.2. The RMS of the S21 sample is lower than the reference S7 (3.0 and 2.2 nm respectively). The reduced surface roughness for the sample grown with interruptions can be associated to the prolonged In and Ga atoms surface migration due to the longer growth time. Also the increased V/III ratio may benefit the surface quality as interruptions provide extra time for the surface nitridization. Longer time for reactant atom migration and higher amount of nitrogen suppress any kind of metal clusterization in either lateral or vertical direction and improves layer-by-layer growth mode [104, 105].

On the other hand, surface roughness calculated for the cyan set slightly increases for the pulsed grown samples, comparing with the reference. Although, there is no clear tendency, on how the pulse duration may influence the values of the surface roughness.

Despite the type of MQW growth, high density of V-pits (7 - 9×10^{-8} cm^{-2}) were observed for the green set. The formation of V-pits begins at the threading dislocations. When In is introduced at the beginning of InGaN layer growth, In segregate around the cores of the threading dislocations. In atoms that are trapped and segregated around the core of a threading dislocation act as a mask, which hinders the Ga atom migration resulting in an opening of a pit. However, the enhancement of atom mobility and reduction of In segregation by using the pulsed growth technique is not sufficient to suppress the V-pit or the trench defect formation in the InGaN MQWs. Still, there is no clear evidence on how pulsed growth influence the V-pit formation.

The V-pit densities calculated for the cyan set of pulsed grown samples were slightly higher than for the green set of samples. The V-pit densities are: 8.5×10^{8} cm^{-2} in the reference S1 and slightly increases to 1.3×10^{9} cm^{-2} and 1.6×10^{9} cm^{-2} in the samples S2 and S6. The fact, that cyan set was grown at a higher temperature, which in accordance with the interruptions probably promoted material desorption and threading dislocation opening into the V-pits that resulted in a higher total V-pit density.

The trench defect densities were evaluated as well. The trench defect density was very similar for all the studied samples and ranged from 1×10^{7} to 2.4×10^{7} cm^{-2}, showing no clear correlation with the growth interruption length.

Table 5.2. AFM measured surface roughness of the references (S1 and S7) and pulsed grown samples (S2-S6, S21).

Sample	**S1**	**S2**	**S3**	**S4**	**S5**	**S6**	**S7**	**S21**
Surface average roughness (nm)	1.4	2.1	1.7	1.7	2.3	2.1	3.0	2.2

To conclude, in structural analysis we have found that QW thicknesses as well as In concentration between the same set of samples were similar: the thickness variation was ±0.2 nm, and the In concentration variation was ±0.5%. On the other hand, In concentration in pulsed green QWs grown at lower *T* have reduced from 27% to 20% when compared with the reference. The In concentration in cyan QWs grown at higher *T* was similar for all samples ~10%. Thus, In concentration sensitivity to pulsed growth technique increases as the growth temperature decreases. Second, pulsed QWs grown at lower temperature were fully strained, while the reference QWs were relaxed. All samples grown at higher temperature were fully strained. Finally, we have not found a clear tendency for how the pulsed growth technique influences surface roughness and V-pit density.

5.2 Optical Properties of InGaN MQWs

The PL was measured and studied for all samples. The influence on PL by the growth temperature and MO pulse and pause duration (t_1 and t_2) was analyzed. Figure 5.9 a) presents the room temperature PL (RTPL) spectra of green set of samples S19, S21 and S22 grown at 780 °C with t_1 = 20s pulses, with different pause durations and compared to the reference sample S7 grown conventionally without interruptions (figure 5.9 b) presents conventionally grown samples at different temperatures. By increasing the pause duration to t_2=12s for the sample S21 the PL intensity more than doubled, compared with the reference S7. The PL intensity increase indicates the decreasing contribution of nonradiative recombination due to either a reduction of the density of NRCs or the existence of a more favorable localizing potential – such as the increased total area of localization [PMD2]. With further increases in pause duration to t_2=15s, the PL spectra declines. This can also be seen in the normalized integrated PL intensity dependence on pause duration for the t_1=20s pulse duration samples in figure 5.10 a), where the PL peak intensity increases only until the pause duration reach t_2 = 12s and subsequently decreases. In addition, increasing the pause duration results in a slight blueshift of a few nm (5.10 b) t_1=20s graph). If we only relate the PL increase to localization profile, it turns out that growth with interruptions increase the density of carrier localization centers. Although, it is still not clear what is the impact of pulsed growth on NRC and how it changes as the pause duration is increased. Also, minor influence is expected due to absorption spectra difference between the samples, which we have not measured.

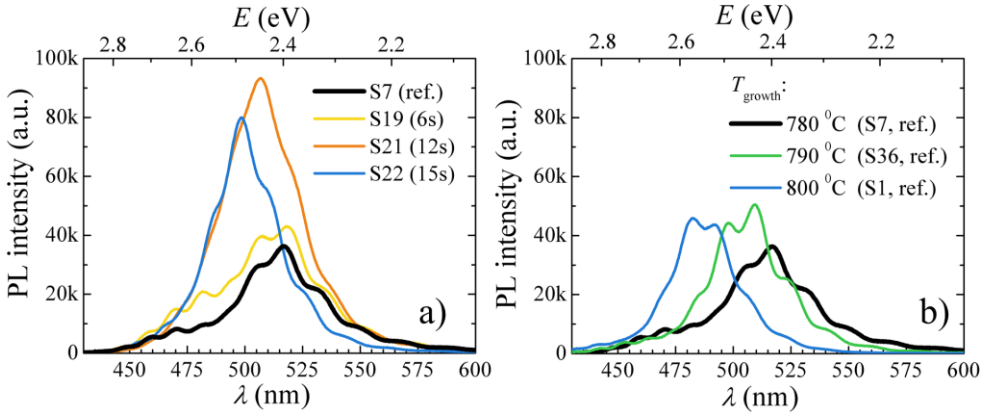

Figure 5.9. a) RTPL of conventionally and pulsed grown MQWS; b) RTPL of conventionally grown MQWs S7, S36 and S1 at 780 °C, 790 °C and 800 °C respectively [PMD2].

The degree of localization depends on FWHM. Higher fluctuation of localization results in a broader FWHM, while the narrower FWHMs accounts for a more homogenous distribution of the localization centers. The measured FWHM (figure 5.10 c)) of the pulsed grown samples has a general tendency to decrease when the pause duration is increased, which signifies an improvement of the QWs. However FWHM of t_1=20s from t_2=0s to t_2=6s increases sharply and with further increases in the pause duration FWHM decreases to the reference value.

The broad PL spectra at the short pause duration implies the increases in fluctuations of localizing potential, which may be caused by the reduction of In in defected areas, which due to the short pause duration forms uneven In concentration clusters. In atoms do not have sufficient time on a surface to migrate to the surface regions where they could create stable bonds – such as at layer step edges.

The influence of pulse duration on PL characteristics for t_1=10s pulses (S13 - S17) and t_1=5s pulses (S8-S12) were also studied. The integrated PL intensity for the samples with t_1=10s (figure 5.10 a)) increases with the increasing pause duration, although the peak value is lower and it is reached at a shorter pause of t_2 = 9s. The peak of integrated PL intensity is even lower for the samples, grown with t_1=5s pulses. The peak value is reached when t_2 = 3s, while further increases in pause duration result in a decrease of integrated PL intensity below the reference value. Thus, in the case of t_1=5s pulses, the amount of reactants transported to the substrate within a shorter time is lower and the adlayer is more vulnerable to the interruptions, even though the total time of growth is the same. Atomic indium has less time during one pulse to be incorporated from the adlayer to the crystal

structure, which makes it easier for In to desorb during the growth interruption. Thus, the average concentration of In decreases. As a result, carrier localization drops and the PL peak blueshifts. At a pause duration of t_2=15s the PL peak position shifts by ~35 nm for the sample t_1=10s and by ~75 nm for the sample t_1=5s. On the other hand, the change in FWHM is negligible and nearly unchanged for t_1=10s and t_1=5s samples - FWHM slightly decreases with the pause increase. The minor influence on FWHM by the pulse time reduction from t_1=10s and t_1=5s as well as increase in pause duration reveals that the degree of carrier localization has a threshold at a certain pulse duration length, after which, the change of carrier localization degree is minor. It is believed that growth with interruptions acts as a multiple annealing process, during which In desorption is elevated, especially from the In-rich clusters around the defect which decreased In segregation and new defect creation [106]. The lack of FWHM change between the shorter pulses even as the pause duration is increased indicates a lack of In-rich clusters and random distribution of In. Also, when the pulses are too short, or the pauses are too long the In concentration in InGaN QWs becomes too low for longer wavelength emission, while the carrier localization decrease reduces the PL intensity.

PL intensity can be simply increased by growing QWs at higher temperatures [107]. As an example, we grew conventionally three InGaN MQW samples at different temperatures: 780 °C, 790 °C, 800 °C (S7, S36, S1 respectively). The room temperature PL spectra was measured for all samples and presented in figure 5.9 b). The measurements were taken during the same approach as the PL spectra of pulsed grown samples presented in figure 5.9 a). Also, to highlight the differences between the spectra, the scales of 5.9 a) and 5.9 b) were unified.

As expected, the PL intensity, as well as, the blueshift increased when the QW growth temperature was increased. This tendency is the same, as the one, observed for the pulsed grown QWs at lower temperatures, although with a lower PL intensity increase. As a result, to enhance the MQW PL, pulsed growth technique can be used instead of using a higher QW growth temperature. By using pulsed growth, the PL peak intensity enhanced more than 2 times with a blueshift of ~8 nm. By growing QWs conventionally, and at 10 °C higher growth temperature (790 °C), the PL peak resulted in a similar blueshift ~9nm, although the PL intensity increased only 1.2 times or 12% of the PL intensity increase in the pulsed grown sample. In other words, the PL intensity increase in pulsed grown QWs is 7 times higher than the increase in conventionally grown QWs at higher growth temperature with the same PL peak blue-shift. Thus, pulsed growth technique is a superior PL intensity enhancing technique compared with the conventional QW growth technique at higher temperatures.

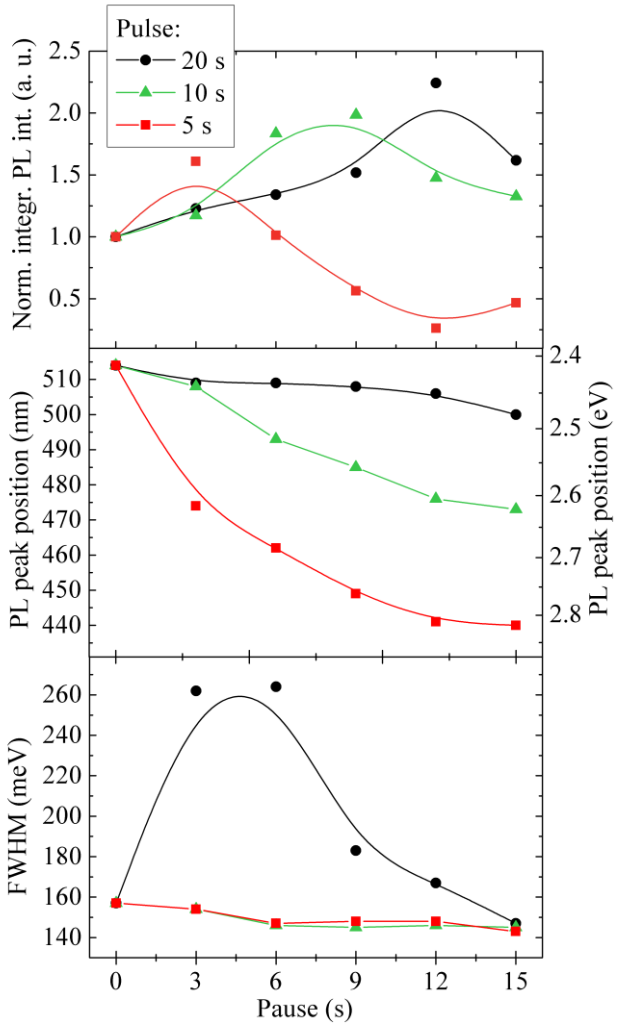

Figure 5.10. The PL measurement results for different growth pause and pulse durations from top to bottom: normalized PL amplitude, PL peak position and FWHM. Black, green and red symbols corresponds to samples grown with 20s (S18÷S22), 10s (S13÷S17) and 5s (S8÷S12) pulse durations. Reference sample - S7 [PMD2]. Lines are used as an eye-guides.

The temperature increase on the pulsed grown QWs was tested as well. Figure 5.11 presents PL results for the t_1=20s sets of samples grown at 780 °C (S7, S18÷S22), 810 °C (S23÷29) and 830 °C (S30÷S35) temperatures with different pause durations. Highest PL intensity reduced almost twice when the growth temperature was raised from 780 °C to 810 °C (figure 5.11 a)). Further increase in QW growth temperature resulted in even lower PL amplitude, which was reached at t_2=3s, and almost didn't change with the pause increase to 12s. The QW growth

at higher temperature has the similar effect on PL characteristics as in the case, when the growth pulse duration is reduced.

The PL peak position shown in Figure 5.11 b) blueshifted as the growth temperature was increased and blueshifted even more when the pause duration was increased. As the growth temperature is increased, the thickness of QW is expected to increase, resulting in lower effective bandgap. The QCSE has a stronger effect on the thicker QWs as well, which further reduces effective bandgap. On the other

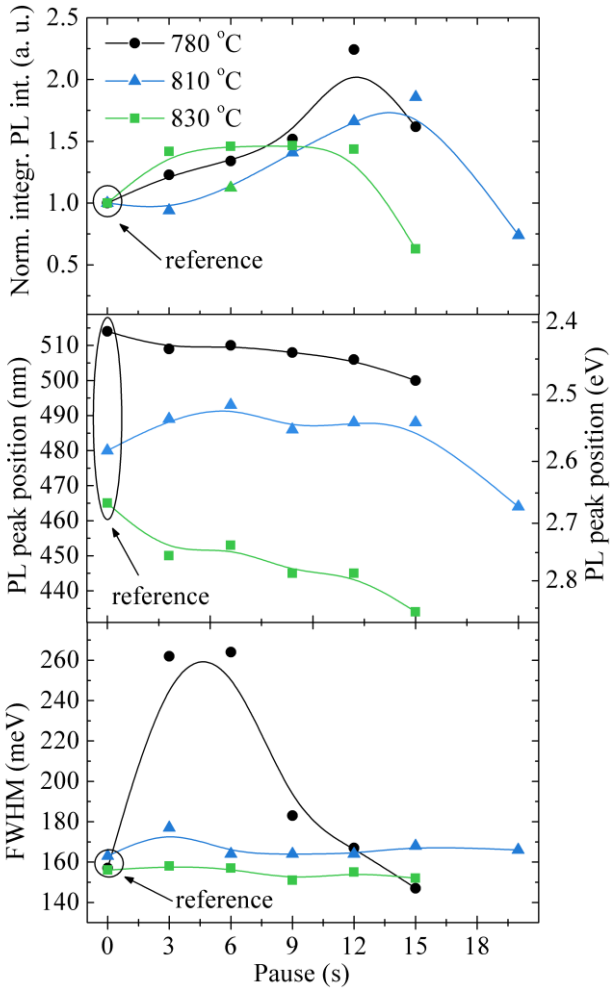

Figure 5.11. Normalized PL amplitude, PL peak position and FWHM dependences on the growth pause duration for three different QW growth temperatures: 780 °C (S7, S18÷S22), 810 °C (S23÷29) and 830 °C (S30÷S35).

hand, as the growth temperature increases, QW In concentration decreases, resulting in the bandgap increase. The latter effect is usually stronger than the former two resulting in a PL peak blueshift as the QW growth temperature is increased.

Although, for the samples grown at 810 °C, the application of a pulsed growth technique (t_2=3s) redshifted the PL peak position by ~10nm from ~480 nm as compared to the reference. With further pause increases to t_2=15s the peak position fluctuated around 490nm. Increasing the pause duration to t_2=20s blueshifted the PL peak. The higher QW growth temperature and pulsed growth technique has a positive more pronounced effect on reducing In segregation. Even though, some portion of In is etched during the interruptions and that amount of desorbed In increases with the pause duration increase, there still exist enough higher In concentration clusters, that act as an additional source of In. In decomposes from those clusters, migrates and compensates the desorbed In. Only when the pause is increased to t_2=20s the sources drain out and desorbed In is no longer fully compensated, which results in a decrease of carrier localization and a drop of PL.

The influence of higher growth temperature on FWHM is also very similar to reduced growth pulse duration – the values of FWHM of samples grown at 830 °C are barely below the values of the samples grown at 810 °C. For both sets of pulsed grown samples FWHM slightly decreases with the increase in pause duration. On the one hand, this proves, that there are fewer higher In concentration clusters that act as deep localization areas and contribute to the peak broadening. As a result, increasing growth pause duration should reduce total In concentration and result in a decrease of FWHM and a blueshift of the PL peak position. Contrary to such prediction, lack of FHWM change and the peak position initial redshift as the growth pause increase, for the set of samples, grown at 810 °C brings us to conclude that there must be some sort of In reservoirs acting as an In source and compensating desorbed In. There has to exist In clusters, or higher In concentration regions that initially do not contribute to the radiative emission – likely due to the vicinity of NRC. As the growth interruption increases, desorption takes place, and the adsorbed In can feed the regions, which contribute to radiative localization centers.

Further, the RTPL was measured for the cyan set of samples and presented in figure 5.12. The spectra were measured using low excitation (P~4W/cm^2), as to get the highest signal from the deeper states in localized areas. The observed PL oscillations are due to Fabry-Perot interference.

Further, from figure 5.12 we extracted spectra parameters: normalized integrated PL intensity, PL peak position and FWHM which are presented in figure 5.13. The cyan spectra had similar tendencies as the ones observed in a green set of samples analyzed before: the increase in growth interruptions resulted in a PL intensity increase up to 2 times (sample S4) and a blueshift of up to 11nm (sample S6). The FWHM increased from 151 meV (reference S1) to 166 meV in sample S2 and remained similar with further increases in pause duration. The different tendencies between PL results of the green and cyan set of samples is hypothesized to be related to the crystal quality. As the growth temperature increases, a decrease in defect density is expected, as well as modification in the localizing profile. As part of our research we did not investigate localizing profile changes of the pulsed grown samples, as the growth temperature changed. Thus, it is difficult to compare the two sets of samples.

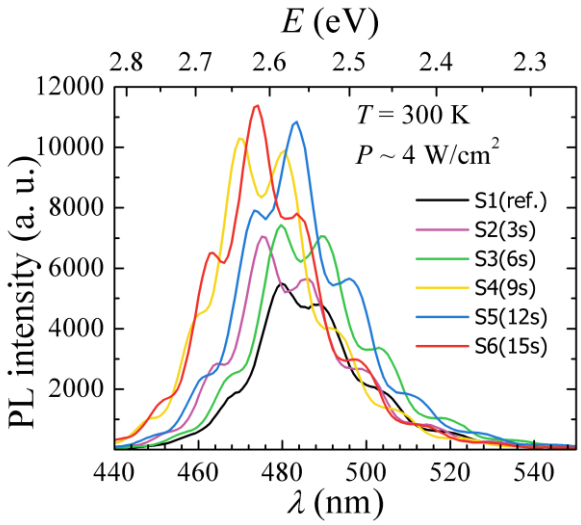

Figure 5.12. PL spectra of cyan set of samples (S1÷S6). PL measured under excitation power density of 4 W/cm^2 at room temperature.

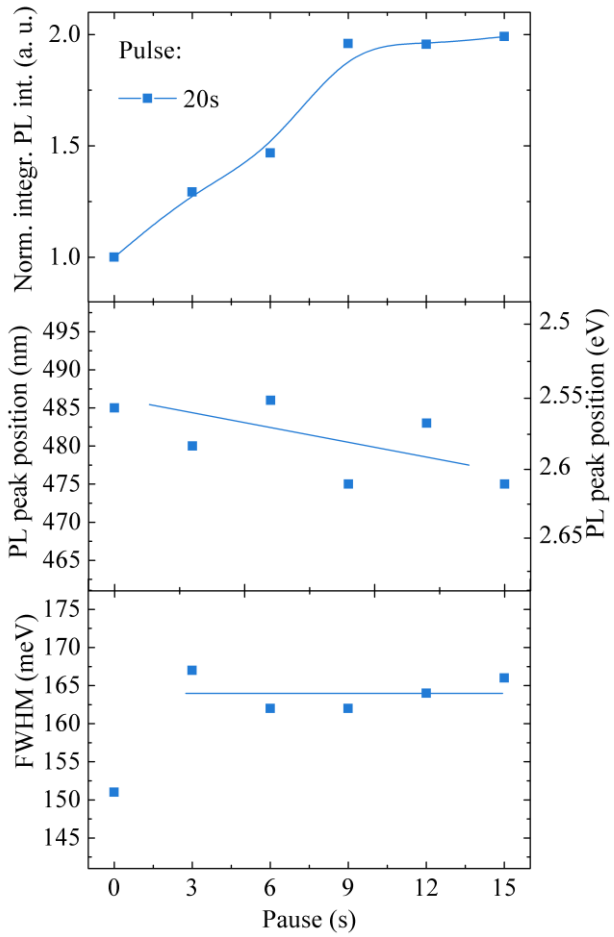

Figure 5.13. Normalized integrated PL intensity, PL peak position and FWHM dependence on growth pause duration for cyan samples grown with 20s pulses and different pause durations 3÷15s (S2÷S6) as well as reference S1. Lines are eye-guides.

However, we were able to analyze the carrier behavior properties of the cyan set of samples and relate them to the changes seen in the PL spectra. The carrier dynamics of our cyan set of samples were reported in a colleague's, Dr. K. Nomeika, thesis and are summarized here as they give additional insight into our work [108]. The IQE was calculated as an exact ratio between the emitted and absorbed photons for all samples (figure 5.14). The IQE enhances by ~7% if a pulsed growth technique is used (see sample S6, 15s pause and reference S1). This shows that the pulsed growth technique has a positive impact on IQE. However, if the pause duration is increased up to 6s from the reference sample (S1), the IQE drops significantly to 13%. Such behavior is suggestive of an increase in the defect density. We

hypothesize that this is because the pause duration is too short for In atoms to find the most energetically favorable sites to create stable bonds – such as at crystal step edges. Instead, due to insufficient In migration there is a higher likelihood to create defect areas and increase the carrier non-radiative recombination.

Further, by measuring excitation dependent carrier lifetimes they found a recombination rate (R) dependence on the carrier concentration (n) $R=An+Bn^2+Cn^3$. The A, B, C constants are Shockley-Read-Hall (SRH), radiative and Auger coefficients respectively. The SRH is a non-radiative carrier recombination through defect states and Auger is a non-radiative recombination due to the energy transfer to the third carrier. A, B, C constants were calculated and presented in figure 5.15. Here one can see that as the pause duration increases up to 6s the A increases, which indicates an increase in defect concentration. Also, radiative recombination (B) decreases, likely because a part of the localizing states become defective states. Thus, both an increase in defect concentration and a decrease in radiative recombination together lead to a drop in the IQE. With further pause increases to 9s and 15s A drops almost to its reference value and B increases ~ three times, which indicates an improvement in the crystal structural quality. At the 12s pause duration the IQE decreases by 7% again. The drop in B must account for such change due to the fact that A increases slightly, whereas C drops by half. Thus, the drop in IQE of 7% below the reference (S1) must be related to a change in the localizing potential. As the pause duration increases, the constant C, has an unclear tendency to change. Thus, its influence on the IQE remains unclear.

It is clear, that the improvement of IQE is primarily related to an increase in the carrier localization. For this reason we further analyzed how the change in pause duration influences the carrier localization in chapter 6.

To conclude, the pulsed growth of InGaN QWs is influenced by pause duration, temperature, and pulse duration. By increasing the growth pause, the PL intensity increases up to its maximum value, the PL peak blue-shifts and the FWHM increases. However, if the pulse growth technique is used at higher temperatures, the FWHM increases, but does not further change with increases in pause duration. Additionally, at higher temperatures the positive impact of the pulsed growth technique for PL intensity enhancement decreases. When shorter pulses are used, the pauses must be shorter as well to reach the highest PL intensity enhancement. And as the pulse duration decreases the peak position blueshifts significantly while the FWHM decreases.

Ultimately, the increase in PL intensity for the pulsed grown samples with longer pause durations (>6s) is related to the increase in IQE due to a transformation in the carrier localizing profile.

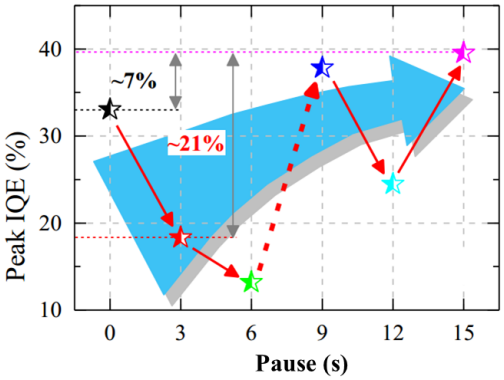

Figure 5.14. Peak IQE dependence on the pause duration for the cyan set of samples S1÷S6 [108].

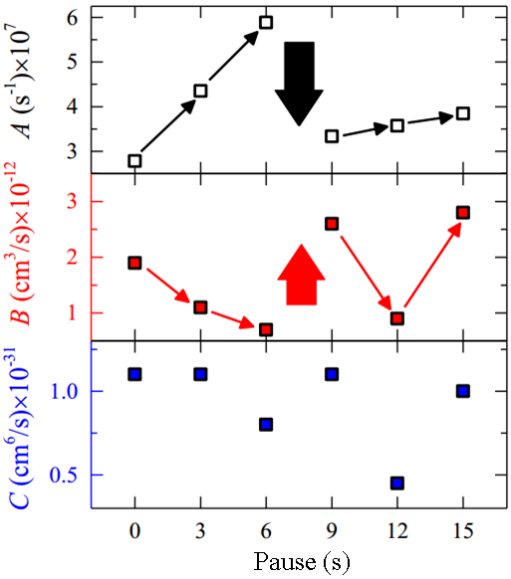

Figure 5.15. ABC modelling results representing Shockley-Read-Hall (*A*), bimolecular (*B*), and Auger (*C*) recombination coefficients' dependence on pause duration calculated for the cyan set of samples (S1÷S6) [108].

6 LOCALIZATION ISSUES AND DEFECTS IN InGaN MQW

6.1 Carrier Localization Profile of InGaN Multiple Quantum Wells

Further, we analyzed the correlation between the growth interruption and In segregation in the InGaN QWs from the cyan set of sample (S1 ÷ S6). The influence of the growth interruption length on the emission properties in InGaN MQWs is studied by using temperature-dependent PL (TDPL) and spatially-resolved PL spectroscopy (μPL). The correlation between the growth interruption length and the PL band parameters are analyzed on macro- and micro-scales and attributed to the variations of localizing potential [PMD3].

The carrier localization conditions of the InGaN/GaN MQWs were estimated by using the PL band peak position dependence on the measurement temperature. Figure 6.1 presents multiple spectra of S1 reference and S2 acquired at different temperatures from 8K to 300K. The PL intensity drops as the temperature of measurement increases. It is known that when the temperature is 8K or below the majority of carriers are localized and due to the lack of energy are unable to delocalize and migrate to NRC. Thus at 8K internal quantum efficiency is close to 100%. By comparing PL intensity at room temperature and at 8K it is possible to evaluate MQW internal quantum efficiency. Figure 6.2 presents the PL intensity of cyan set dependence on measurement temperature that was normalized to PL intensity at 8K.

Further, by using the data presented in figure 6.2, the internal quantum efficiency was calculated (figure 6.3). It can be clearly seen, that IQE increases as the growth pause duration is increased. Still, values of IQE are much lower if compared with the values calculated from the carrier dynamic measurements (Figure 5.14), which may be due to the specifics of each method. Here the highest increase in IQE is in the sample S4 (9s) – the same tendency as was previously observed.

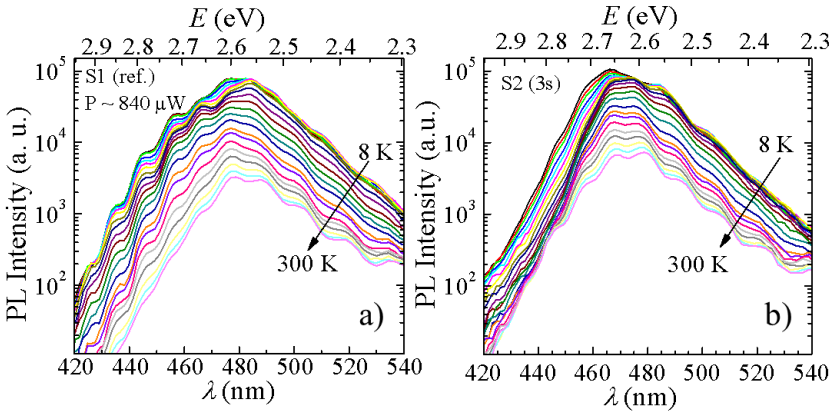

Figure 6.1. Multiple spectra acquired at different temperatures from 8K to 300K of: a) S1 reference and b) S2 pulsed grown sample [PMD3].

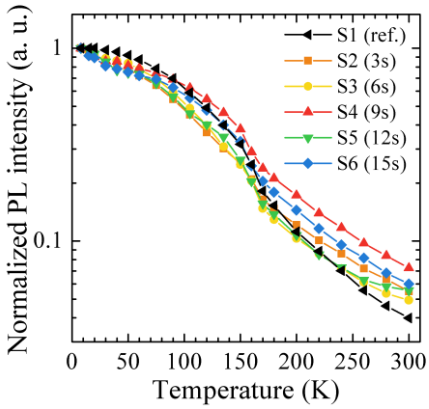

Figure 6.2. PL intensity dependence on measurement temperature. Values were normalized to the PL intensity at 8K temperature.

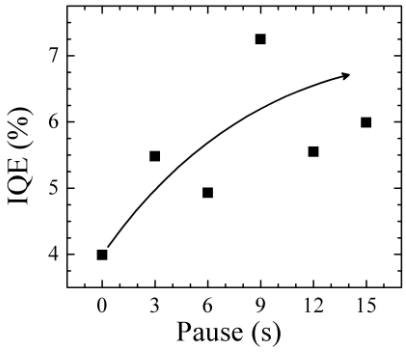

Figure 6.3. PL internal quantum efficiency cyan set of samples. The line is an eye-guide [PMD3].

Next, the PL spectra peak shift's dependence on PL measurement temperature was calculated and is presented in figure 6.4. The peak position shift was calculated with respect to the peak position at 8K. One can see in figure 6.4 that all samples exhibit three regions: redshift/blueshift/redshift - an S-shape tendency with temperature increases. Such S-shape tendencies that are typical for the III-N ternary compounds are usually attributed to the carrier hopping through localized states [109]. At low temperatures (0÷10K) carriers are randomly distributed in the potential minima. With the initial temperature increase (10÷70K) carriers still don't have sufficient thermal energy to overcome the localization potential so they redistribute by relaxing down to the lower energy level states, which results in reduced higher energy emission. By further increasing the temperature (70÷160 K) more carriers have sufficient thermal energy to delocalize and occupy higher energy level states, resulting in a peak blueshift. At (160÷300 K) the temperature-induced bandgap shrinkage becomes a dominating process causing the peak position to redshift again [110, 111]. Figure 6.4 summarizes the influence of growth interruption time on the S-shapes. The S-shapes slightly change when the growth interruption time is increased - the initial redshift becomes larger, while the peak blue shift decreases. The temperatures, at which the redshift-blueshift and blueshift-redshift turning points occur, are nearly constant for all samples, except for the sample S1, which exhibits its turning points at slightly lower temperatures.

The blueshift-redshift region of the S-shape can be approximated by the use of quantitative modeling linking it to the local potential fluctuations. At nondegenerate carrier occupation, the temperature dependence of the PL peak position can be expressed by the Eliseev modified Varshni equation (6.1).

$$E_{peak}(T) = E_g(0) - \frac{\alpha T^2}{\beta + T} - \frac{\sigma^2}{k_B T} \tag{6.1}$$

Here, $E_g(0)$ is the band gap at $T = 0$, α and β are the Varshni coefficients for the band gap reduction with increasing temperature and σ is the standard deviation of the Gaussian distribution, which depends on the band gap fluctuations either because of the random In content and/or QW width fluctuations

The 6.1 equation was used to approximate the S-shapes of the samples S1, S3 and S5 (solid lines in figure 6.4). The α and β values were interpolated between GaN and InN values [112, 113] and were 0.85 meV/K and 800 K respectively. The blueshift/redshift transition temperatures for the S3 and S5 are nearly the same and the estimated σ values were similar and equal to ~28 meV. Although, the blueshift/redshift change of the S1 occurred at slightly lower transition temperature and the estimated σ value was lower (~ 25 meV).

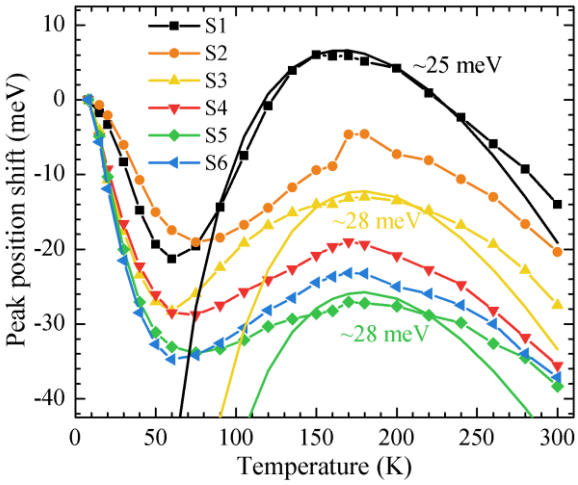

Figure 6.4. S-shape temperature dependences of PL band peak position shift in InGaN/GaN MQWs. Solid lines show the approximation by the Varshni equation [PMD3].

The room temperature PL measurements of the cyan set show that by introducing pulsed growth, localized states distribute in a slightly wider energy range (Figure 5.13 c)). On the other hand, the FWHM as well as σ values have a low variation between the samples with different interruption times, which indicates that the influence of growth interruption time duration for the aforementioned values is negligible. Nonetheless, the initial red shift value increases, as the pauses are increased, which points to the certain transformation of the localization profile. Initial low temperature redshift occurs due to the thermally activated carrier redistribution to the lower energy localization centers. Thus, a larger initial redshift suggests the existence of a higher density of deep localized states. The lower s-shape blueshift demonstrate that there exists a higher density of deeper states and lower density of shallow states.

On the other hand, room temperature PL peak blueshift with the interruption time increase implies that there exists a larger population of higher energy localized states comparing with the reference. This lead us to conclude that the pulsed growth increases the density of deep localized states, while the energy difference between the deep states and mobility edge – decreases.

6.2 Spatial Distribution of Localizing Potential of InGaN Multiple Quantum Wells

μPL was measured to gain insight into the properties of the localizing potential and how it changes with the growth interruption time increase. Figure 6.5 presents the μPL mapping of 60x60 μm^2 and 10x10 μm^2 intensity distribution. μPL was measured using 405nm low excitation (~0.3μW, ~420 W/cm^2) source. As can be seen in figure 6.5, the PL is emitted not homogenously but rather from the higher intensity spots that are dispersed on the lower intensity background.

Next, the μPL spectra were averaged over 10x10 μm^2 and 60x60 μm^2 areas and presented in figure 6.6. Data extracted from all of the samples μPL measurements were statistically averaged and are listed in table 6.1.

The differences in the 6.6 figure between the spectra intensities can be noticed. In figure 6.6 a) the highest PL intensity is emitted from the S2 sample, while in the macro PL measurements (Figure 5.12 a)) PL intensity of S2 sample was slightly higher than the intensity of the reference S1. The differences become even more surprising in the 60x60 μm^2 area μPL measurements (figure 6.6 b)). One can notice, that the intensity of the reference S1 is almost as high as the highest peaks from the pulsed grown samples. While the sample S5, which was noted to have twice the increased macro PL intensity here possesses the lowest intensity – almost 30% lower than the reference S1. This leads us to the conclusion, that the emission from the surface area is not homogenous throughout the whole sample. Although the PL peak positions of different samples remain almost the same regardless of the area, from which the spectra was collected. Thus, observed differences between intensities must be related only to the localization area distribution, but not to the difference in the localization profile itself.

To better understand the μPL, spatial distribution of S2 sample's μPL intensity was compared to the peak position distribution and presented in figure 6.7 a) and b). One can see in figure 6.7 a) that the distribution of PL intensity is inhomogeneous and composed of the higher emission intensity areas on a background of lower emission intensity. The spatial variation s – the standard deviation divided by the mean value was calculated for the PL intensity and peak positions. The spatial variation of PL intensity was almost the same for all of the samples ~0.47. The peak positions' distribution varied, although with rather small spatial variations from 3 to 4 nm (16 to 20 meV).

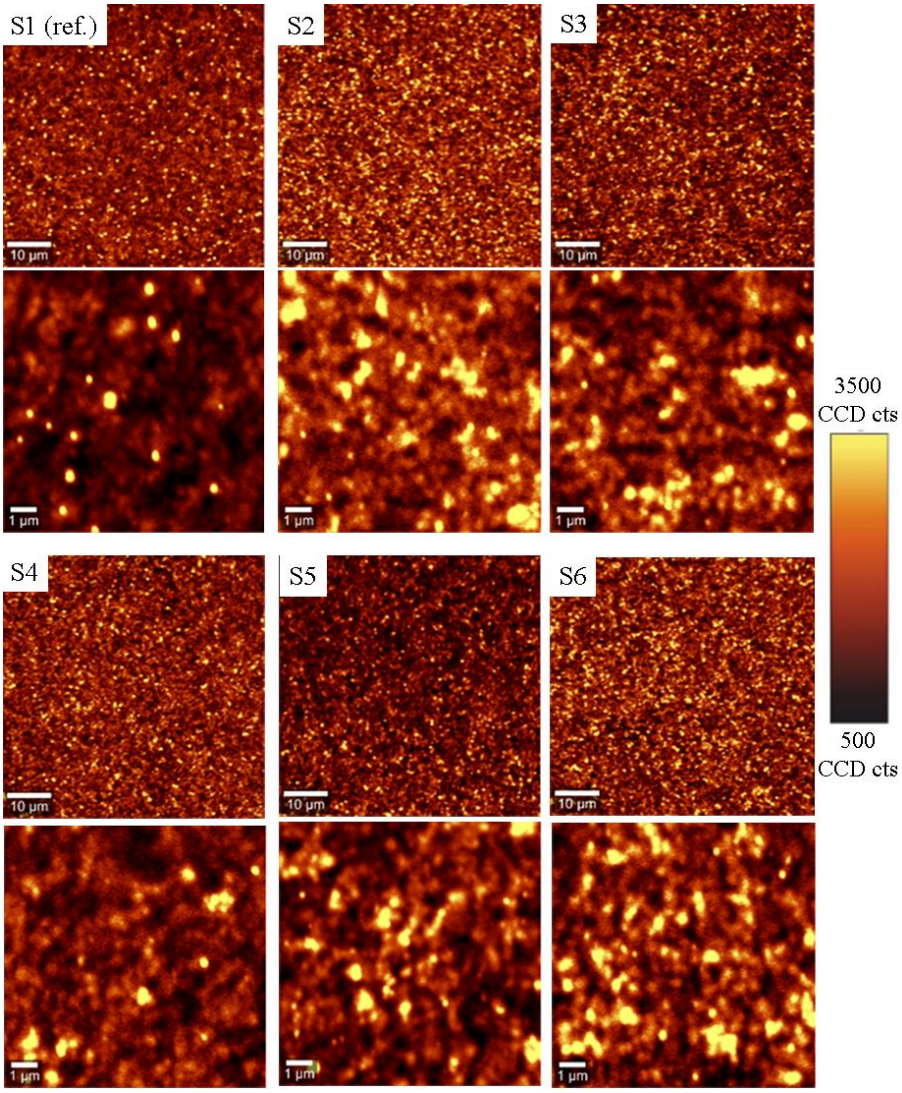

Figure 6.5. µPL intensity of the S1-S6 samples, collected from 60x60 μm^2 areas – upper images, below - magnified images of 10x10 μm^2 areas.

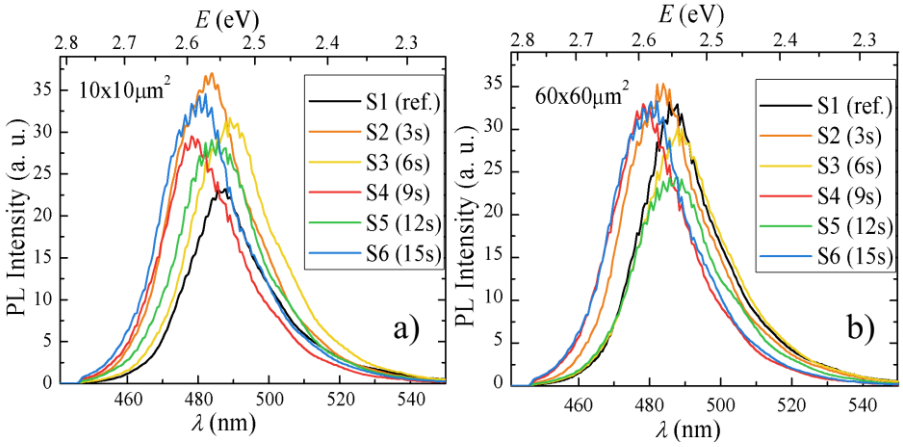

Figure 6.6. Room temperature μPL spectra of S1-S6 samples acquired from: a) 10x10 μm^2 and b) 60x60 μm^2 areas.

Random μPL dot spectra taken from darker and brighter areas are shown in figure 6.7 c). The detailed analysis of the single-pixel PL spectra revealed that some pixels (size of 50×50 nm^2), especially those that have higher intensity have a high increase in FWHM due to the emergence of a significantly red-shifted peak at ~510nm. While, the main spectra from the background was at ~480nm. Double peak characteristics can be seen in figure 6.7 for the B, E and A spectra. If the intensity of the red-shifted peak is high enough (curves E and A), it results in a strong redshift of the overall PL spectrum. Tao et. al. suggested, that such broad PL spectra having characteristics of double peaks can be assigned to the luminescence from the spots in vicinity of the V-pits [114]. The high In content regions that form ring-shaped quasi potential traps exist around the V-pits in InGaN epi-layers. These quasi potential traps can attract carriers and suppress non-radiative recombination. The long wavelength peaks are assigned to the emission from the spontaneously formed In-rich regions around the V-pits. While the short wavelength peaks are due to the emission from the V-pits [115]. The MQW on the side of the V-pits walls are thinner than the rest of the MQW, and due to the increased quantum confinement bandgap increases, resulting in a spectral blueshift. In addition to that, emission in the vicinity of trench defects and especially from the surrounded regions by the trench defects accounts for the blueshifted PL band with higher intensity [39]. The blue shift occurs mainly due to the InGaN strain relaxation and reduction of QCSE effect.

As it was mentioned in the chapter 5.1, V-pit densities for the cyan set of samples were in the range between 8.5×10^8 cm^{-2} and 1.6×10^9 cm^{-2} with no clear correlation as the pauses of the pulsed growth increased.

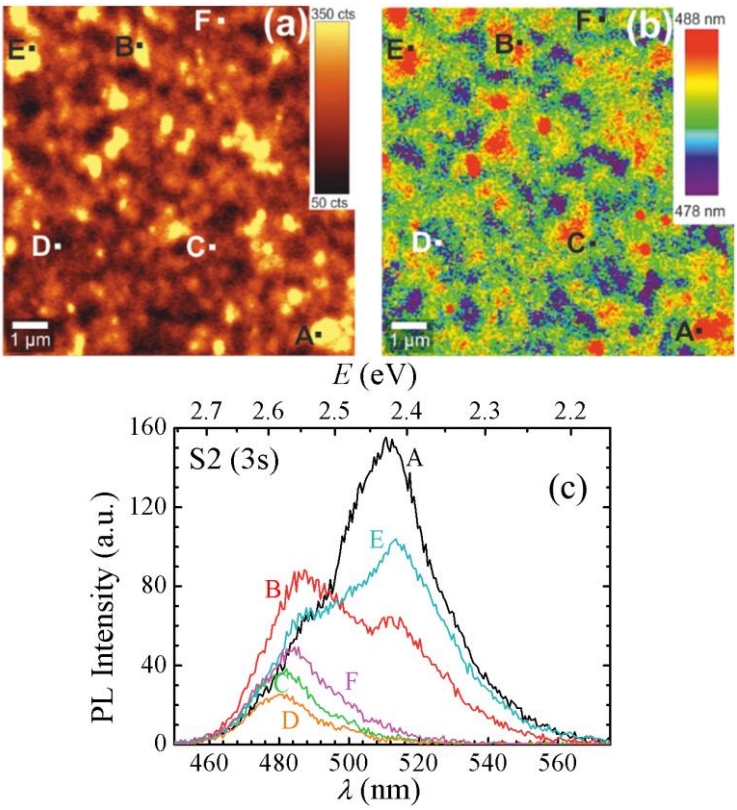

Figure 6.7. μPL measurements of sample S2: a) spatial distribution in 10×10 μm^2 area of spectrally-integrated PL intensity, b) PL peak wavelength spatial distribution, and c) several PL spectra taken from indicated spots [PMD3].

The total defect density can be resolved not only from AFM measurements, but from the μPL measurements as well. As noted previously, the spots in the vicinity of the V-pits tend to account for a strong peak redshift. The typical V-pit diameter is ~80 nm and the spatial resolution of confocal PL measurements is ~250 nm, due to the blur effect, strong redshift significantly increases the individual pixel band-width (more than 1.5 standard deviation *s* of the band-width). Thus, the approximate V-pit density can be measured by calculating the individual pixels that have FWHM of more than 1.5 standard deviations *s* of band width distribution. Although, lower resolution (than the one requeired to distiguish individual V-pits) effectively reduces the resolved V-pit density up to an order of magnitude.

As an example, the spatial distribution of the PL bandwidth collected from the sample S2 is presented in figure 6.8. Here the individual pixels having a band-width of more than 1.5 standard deviations *s* of FWHM are marked with black

masks. Such masks were applied for other samples as well by calculating individual pixels with a band-width of more than 1.5 standard deviations *s* of a particular sample's FWHM and presented in figure 6.9 as the yellow regions.

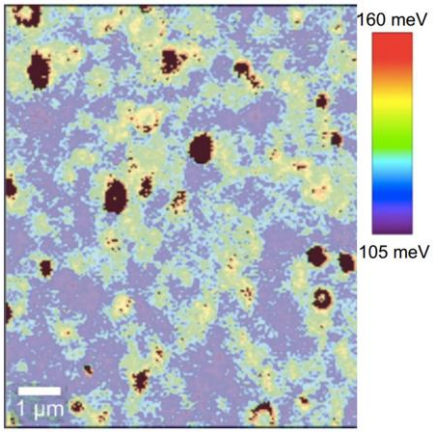

Figure 6.8. Spatial distribution of PL bandwidth within an area of 10×10 µm^2 of InGaN/GaN MQWs sample S2. The PL band width in marked pixels is above average by at least 1.5*s*, where *s* is the standard deviation of band width distribution [PMD3].

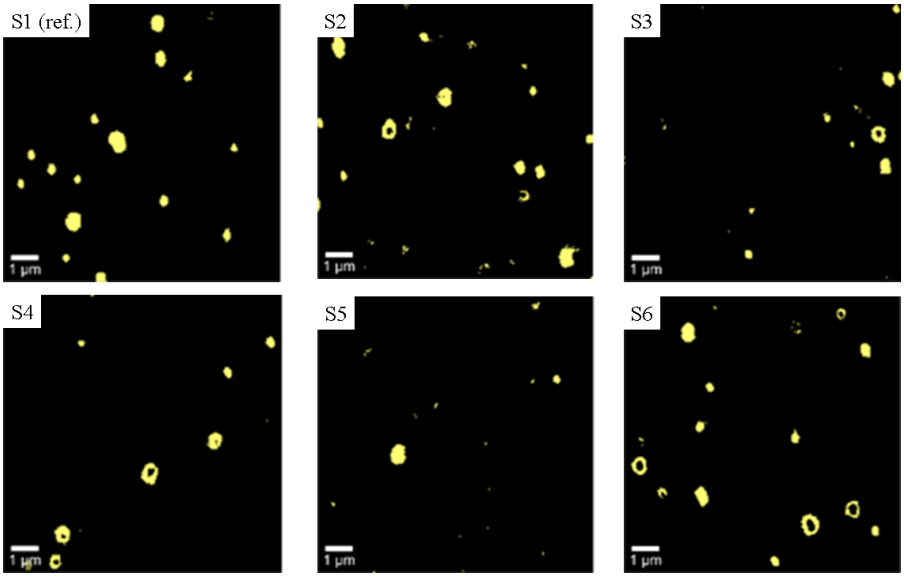

Figure 6.9. µPL images of V-pits and trench defects for the set of samples S1÷S6. Yellow masks represent selected pixels from µPL band-width images that were above average band-width by at least 1.5*s*, where *s* is the standard deviation of band width distribution.

The total resolvable defect density from μPL bandwidth distribution in the S1 sample was 1×10^8 cm^{-2}, and $(1.5\text{-}1.7)\times10^8$ cm^{-2} in other samples. It was found that such pixels take only ~3-4% of the total area and they do not considerably affect mean values of the spatially integrated PL band.

Trench defects are the other type of defects that could potentially influence the PL spectra outcomes. As for the V-pits, the vicinity of trench defects manifests themselves with the PL redshift and higher intensity spectra. Also, the diameter of trench defects is in the range of hundreds of nm, thus it can be distinguished from the μPL measurements more easily by counting only the "trench" like regions. As mentioned in chapter 5.1, the trench defect density change showed no clear tendency, as the growth interruptions increased. The lack of considerable correlation between the growth interruption time and the defect densities are not sufficient to evaluate the pulsed growth influence on NRCs. Also, the area that was covered by the trench defects was less than 2%.

A significant portion of the remaining area was covered by the pixels with relatively large FWHM ranging between 110 to 125 meV. The large FWHM from such individual pixels suggests the existence of the double-scaled potential profile – the existence of large and small scale inhomogeneities. The large areas in the size range of hundreds of nm manifest the peak wavelength variations. The small areas in the size range of a few nm that are the part of the large areas are revealed through the inhomogeneous broadening of the local PL spectra. These observations demonstrate the presence of a double-scaled potential profile - band-gap fluctuations due to different average indium content within the In-rich regions, which is usually observed in InGaN/GaN MQW structures [116, 117].

To understand the carrier localization properties we calculated PL intensity and the count of spots (μPL individual pixels) with certain PL parameters for the cyan set of samples that were depicted in figure 6.10. The influence of growth interruptions to deep localized states was analyzed, by choosing spectra from pixels having peak positions higher than the standard peak position deviation. The average peak positions from deep localized states were calculated and presented for each sample in figure 6.10 with red arrows. Blue arrows point to the position of the average overall PL peak position.

Reference S1 has a wide distribution of high intensity pixels throughout the spectra with a low count number. On the other hand, the highest count number was noted in the shorter wavelength pixels having lower intensity. The average PL peak position of S1 is 487 nm, in the mid where the highest number of pixels was counted. There are a lot of pixels with a high intensity, but a low count number distributed in a wide range on the longer wavelength side. Although, it doesn't

seem, that these discrete pixels have a high impact on the average peak position. Spectra is mostly governed by the high number of counts.

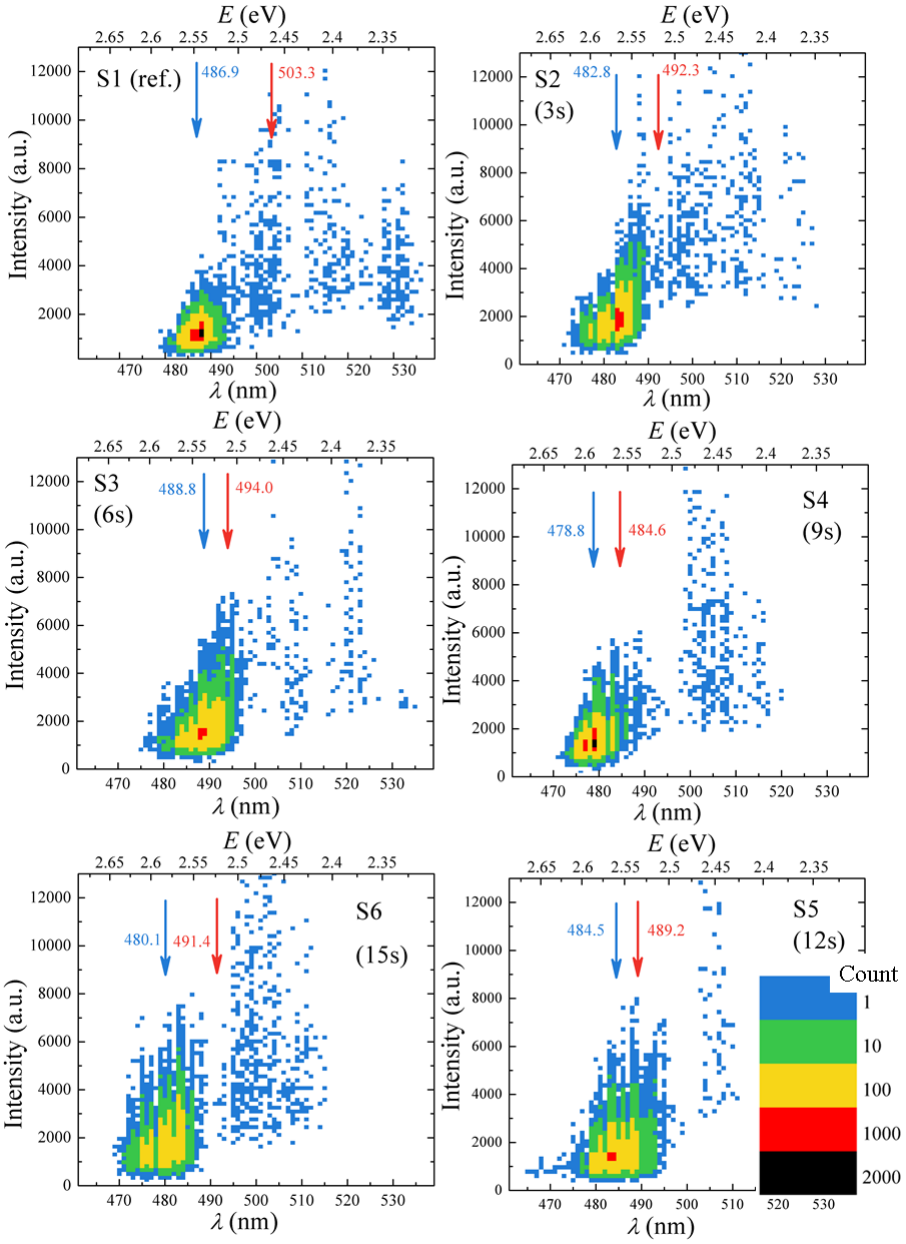

Figure 6.10. Intensity and count distribution throughout the spectrum. Blue arrows shows peak position mean values, red arrows - average peak position in deep localized states – with a peak positions of more than a standard deviation.

None the less, as previously discussed, it is expected that a pulsed growth technique increases the density of deep localization centers. However, the region, having a higher pixel count density (>100) ranges more than the standard peak position deviation. As the growth interruption increases, deep localization centers become distributed more homogeneously – region of high count pixels above the standard peak position deviation shrinks and number of individual high intensity redshifted pixels decreases. Finally, the difference between the average peak position of deep localization and overall average peak position decreases (from 16.4 to 4.7 nm in reference S1 and S5 respectively) consistently with the PL band blue shift.

Further, the data from μPL measurements was used to calculate Pearson correlation coefficient (PCC) ρ between the PL peak position and PL intensity for the cyan set of samples (see figure 6.11). The ρ can have values between +1 and -1, where ρ =1 means the total positive linear correlation, ρ =0 means, that there is no linear correlation and ρ =-1 means that the linear correlation is totally negative [118]. The correlation between the PL peak position and PL intensity was positive and PCC was in the range of ~ (0.2÷0.7). The PCC had a trend to decrease with the growth interruption time increases. The correlation between the PL peak position and PL intensity is usually positive for the InGaN materials and is caused by the lower probability of carriers, localized in deeper energy levels to reach NRCs and a higher probability for those carriers to recombine radiatively at longer wavelengths [119]. Decreasing PCC signify, that the density of NRC is lower - carriers localized at shallower energy levels maintain a lower probability to reach NRC, which results in a higher PL intensity at longer wavelength. As a result, the peak position blueshifts and the FWHM increases.

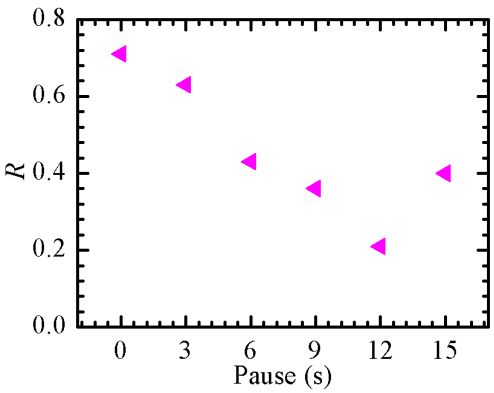

Figure 6.11. Peak wavelength-to-peak intensity Pearson's correlation coefficient calculated from the 10x10 μm^2 μPL scans with ~18.4kW/cm^2 power density excitation for the samples S1÷S6.

In figure 6.10 we have observed, that the PL spectra is most likely governed by the highest pixel number which was centered at the average PL peak position. Thus, it is most likely that the carriers will localize in this range. However, the pulsed growth technique primarily had an influence on the deep localized states.

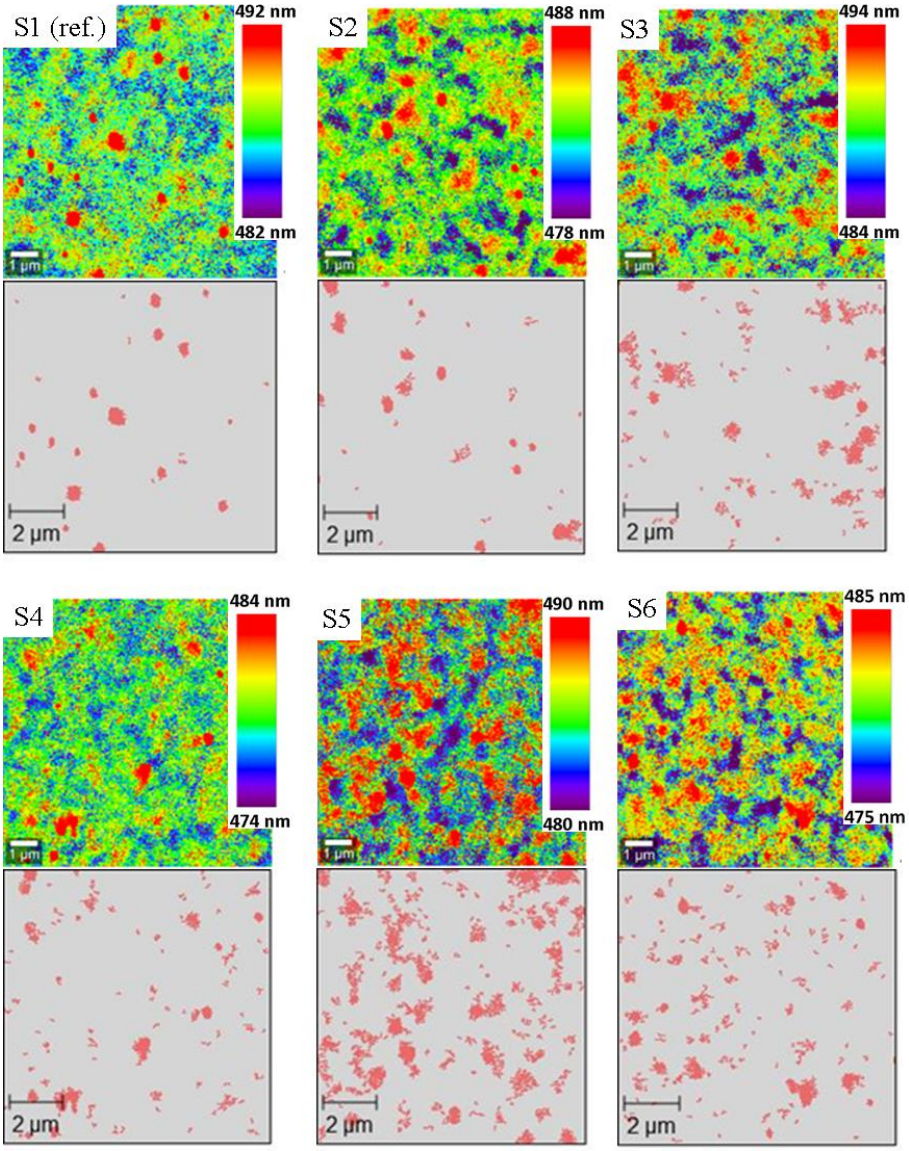

Figure 6.12. µPL spectral mappings of 10x10 µm^2 areas from the samples S1-S6 and the deep localization regions – redshifted more than the standard deviation from the average peak position (below each µPL mapping).

To study the effect of the growth interruption time on the deep localized states, we selected the μPL pixels (areas) from the μPL spectral images of cyan samples with the peak positions higher than the standard deviation from the average PL peak value. Figure 6.12 presents the μPL spectral images of cyan samples with the peak position of ±5nm from average μPL peak position for each sample. Bellow each image, the spatial distributions of selected areas are presented.

Table 6.1. The data of the InGaN MQW growth conditions and μPL measurements calculated from 10x10 μm^2 μPL scans.

Sample	S1	S2	S3	S4	S5	S6
Growth interruption length (s)	0	3	6	9	12	15
PL intensity mean (a. u.)	1210	1980	1740	1520	1590	1850
Intensity variation	0.48	0.43	0.44	0.43	0.47	0.54
Peak wavelength mean (nm)	487	483	489	479	485	480
Peak wavelength deviation (nm)	4.0	3.4	3.2	3.0	3.3	3.7
FWHM mean (meV)	110	125	125	121	123	124
FWHM deviation (meV)	20	17	15	15	13	18
σ (meV)	25	28	28	28	28	28
Peak wavelength-to-peak intensity Pearson correlation coefficient	0.58	0.61	0.47	0.56	0.31	0.48

The number of grains, the mean grain area and the total area of grains were estimated for all samples and presented in figure 6.13. One can see that increasing the growth interruption time resulted in a reduction of the mean grain area, although, the number of grains, as well as the total area of these grains increased.

Our experimental observations support the idea that the change of InGaN MQW PL band properties in the samples grown with a pulsed growth technique are caused by the modification of localizing potential. As the time of growth interruptions increases, the supply of NH_3 is increased. Choi et al. suggested, that extra time for the surface nitridization and In atom migration suppresses any kind of In segregation both – laterally and vertically [104]. Also, Kadir et. al. has shown, that extended V/III ratio produces smaller and denser localization islands – the same result as observed in our samples, when the growth interruption time was increased [120].

Thus, we believe that the smaller clusters have a higher density of deep localized states with reduced difference between the states and mobility edge. This fact is supported by our previous observations of a constant blueshift with an increase in time of growth interruption. On the other hand, due to the increase in the density of clusters, the total area covered by the clusters increased. Thus, a

higher number of grains contains a higher number of total density of localized states. Localization, as well as, the carrier suppression from migration to NRC is increased. As a result, increasing growth interruption time results in PL intensity increases up to 2 times, despite the increase in V-pit density. When the growth interruptions are too long, the positive effects of the pulsed growth technique decrease, because of the higher influence of In re-evaporation or thermal etching, as it was observed for the sample S6, where the total number of grains as well as the total area of clusters decreased.

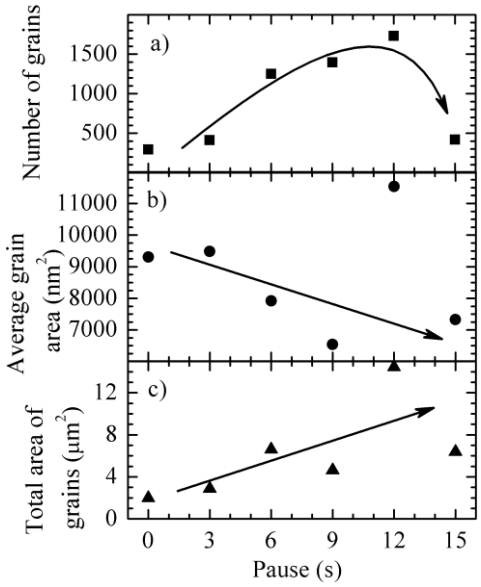

Figure 6.13. The number of grains, mean grain area and the total area of grains as a function of pause duration. Arrows are presented as an eye-guides [PMD3].

To conclude, we have found that the increase in PL intensity as the growth pause duration increases is governed by the increase in the density of deep localization states. Also, with the growth pause increase the difference between the average energy of deep localization states and mobility edge decreases. Finally, as the QWs are grown using pulsed growth technique, carriers distribute in a slightly wider range of energy of deep localization states, although the pause duration increase has a minor influence on the range of energy.

7 PULSED GROWN MQWs IN LIGHT EMITTING DIODE STRUCTURE

After developing the pulsed growth technique it was applied during the growth of MQWs in light emitting diodes (LEDs). Three LEDs were grown (LED1, LED2, LED3) having the same structure (see schematic representations in figure 7.1). LEDs consisted of 2.5 µm uGaN layer with AlGaN/GaN SL, 1.2 µm nGaN layer, 4nm InGaN/GaN SL, 5 period of InGaN QWS d_{QW}=(3÷4)nm, In=(15÷20)%, d_{QB}=6nm, ~25 nm pAlGaN layer and 200nm pGaN layer. QWs were grown using the pulsed growth technique applying 6 t_1=15s pulses with t_2=12s pauses. The only difference between the LED fabrications was that each LED had the QWs grown at different temperatures: 793 °C, 797 °C and 803 °C for the LED1, LED2 and LED3 respectively.

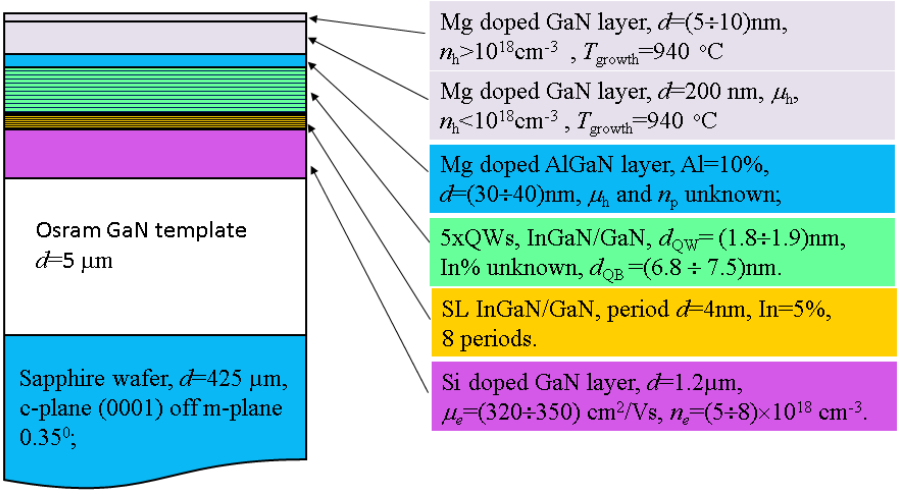

Figure 7.1. Schematic layer structure of LEDs.

The optical characteristics of LEDs were measured at *TopGaN* Company. Figure 7.2 presents the PL spectra of all samples measured with continuous wave (cw) 325nm excitation. As it can be expected, growth of LED2 and LED3 at higher temperatures resulted in a PL peak increase and peak position blue-shift. Such tendencies as discussed in chapter 5.2 can be related to the lower In concentration, which is expected in the samples grown using higher growth temperature, leading to the peak blueshift, and decreased defect density, as well as lower NRC, which leads to the higher intensity of luminescence. One can notice in figure 7.2 that PL consist of fringes, which are due to the Fabri-Perot interference.

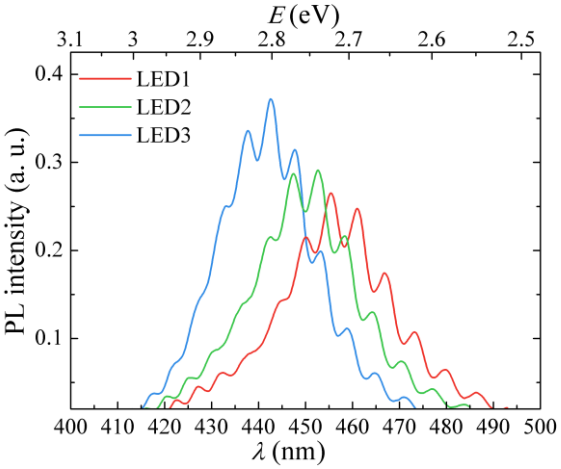

Figure 7.2. PL spectra of LED1-LED3

Further, electro luminescence (EL) at 20mA current was measured for all LED structures and presented in figure 7.3. Spectra was collected using sphere, thus Fabri-Perot interference is not present. The EL spectra has the same tendency as the one observed for PL measurements – as the QW growth temperature increased, LED spectra increased and blueshifted.

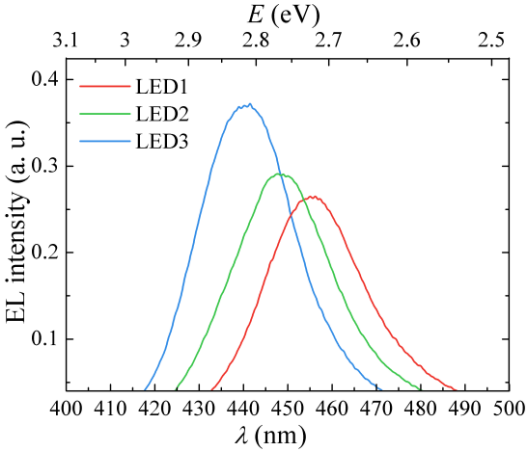

Figure 7.3. Electro-luminescence of LEDs.

Figure 7.4 presents external quantum efficiencies (EQE) calculated for the LEDs as a function of applied current. It was found that the highest EQE was measured for the LED3, which reached 2% with a forward current of 100 mA. EQE of LED1 and LED2 were similar with the peak values of 1.2% and 1.4% respectively. From the

EQE measurements, the internal quantum efficiency (IQE) was evaluated and the light extraction efficiency (LEE) was calculated at *STR* Company.

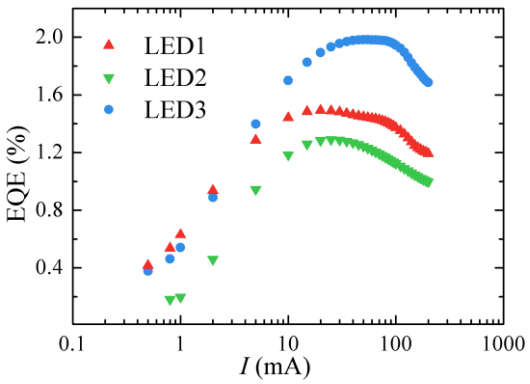

Figure 7.4. External quantum efficiencies of LEDs.

The IQE maximum value η_i^{max} was calculated by using EQE measurement results and ABC-model calculations (7.2 equation) that were presented in the paper published by Titkov et. al. [121]. The ABC model describes the case of recombination rate *R*, when electrons and holes are equally injected into the active region (see 7.1 equation, where A, B and C stands for Shockley-Read-Hall, radiative and Auger coefficients respectively and n- carrier concentration. The relation between EQE maximum efficiency η_e^{max} and EQE $\eta_e(p)$ in equation 7.2 (dependence on normalized optical power p) were measured, quality factor Q was calculated after finding ABC parameters (equation 7.3) and the normalized optical power extrapolated (7.4).

$$R = An + Bn^2 + Cn^3 \tag{7.1}$$

$$\frac{\eta_e^{max}}{\eta_e(p)} = \eta_i^{max} + \frac{p^{1/2} + p^{-1/2}}{Q + 2} \tag{7.2}$$

$$Q = \frac{B}{(AC)^{\frac{1}{2}}} \tag{7.3}$$

$$p^{1/2} + p^{-1/2} \to 0 \tag{7.4}$$

$$\eta_e(p) = \eta_{ext}\eta_i \tag{7.5}$$

EQE is a product of IQE η_i and the light extraction efficiency (LEE) η_{ext} (equation 7.5). Thus, when the IQE and EQE values are known, LEE can be simply calculated. The IQE and LEE values are presented in table 7.1. As it was expected, LEDs grown at higher temperature possessed higher structural quality that led to higher IQE values with the highest IQE of 42,8% of LED3. The LED surfaces were not texturized, thus the LEE values were low. On the other hand this had a major impact on EQE values, which were only a few percent.

Table 7.1. Optical parameters of LEDs.

Sample	LED1	LED2	LED3
λ, nm	455	447	443
IQE max, %	28,6	35,5	42,8
LEE, %	4,5	4,4	4,6

CONCLUSIONS

1. PL intensity in InGaN QWs can be increased if during one pulsed growth cycle no less than 1 InGaN crystal monolayer is grown. By using five 20s duration pulses a pause duration of 12s (9s) and a growth temperature of 780 ^{o}C (800 ^{o}C), the PL intensity of green (cyan) light emitting MQW was enhanced up to two times with a minor peak blueshift compared with conventionally grown structures.

2. The pulsed growth technique is superior at enhancing PL intensity as compared to QW grown at higher temperatures using a conventional growth method. The PL intensity increase is 7 times higher when compared with the PL intensity increase in conventionally grown QWs at higher growth temperature with the same PL peak blue-shift.

3. There is preliminary evidence that when the pulse duration is reduced (<20s) without a change in the pause duration (12s), Indium desorption increases particularly from higher In concentration regions resulting in a lower density and shallower localized states. As a result the PL intensity decreases and the PL peak blueshifts.

4. Using 20s pulses and increasing the growth pause duration (≥9 s) creates a higher density of indium-rich clusters resulting in a larger total density of localized states and PL intensity increase (~2 times). While the average In concentration in In-rich cluster decrease. As a result energy of deep localized states is shifted towards the mobility edge resulting in a PL peak blueshift (~8nm).

5. The InGaN MQW pulse growth method has been applied in technological research to grow a complete LED structure.

SANTRAUKA

Įvadas

Šviesos diodai (šviestukai) bei lazeriniai diodai (LD) yra šviesą emituojantys optoelektronikos prietaisai turintys plačias pritaikymai galimybes tiek namų apyvokos, tiek ir mokslinių tyrimų srityse. Indžio galio nitridas (InGaN) yra universali medžiaga plačiai naudojama optoelektronikos prietaisuose. Unikali InGaN savybė yra ta, jog keičiant indžio (In) koncentraciją galima modifikuoti emisijos spektrą, kuris apima visą regimąją spektro dalį [1, 2]. Nuo tada, kai devyniasdešimtųjų metų pradžioje buvo atrastas mėlynas InGaN šviestukas [3], InGaN heterostruktūrų vystymosi eiga kietakūnio apšvietimo srityje patyrė didelį technologinį šuolį [2]. Per pastaruosius dešimtmečius ženkliai išaugo InGaN šviestukų efektyvumas, sumažėjo energijos sąnaudos bei padidėjo galimybės išauginti šviestukus platesnėje spalvinėje gamoje.

Deja, palyginus eksperimentines efektyvumo vertes su teorinėmis, InGaN struktūros užaugintos epitaksiškai naudojant metalo-organikos nusodinimo iš garų fazės metodą (MOVPE) ant safyro padėklų, dar nėra pasiekusios teorinio potencialo, ypač žalioje spektro dalyje. Šiuo metu egzistuoja keletas iššūkių, ribojančių galimybes pasiekti teorines efektyvumo vertes. Viena iš problemų yra tai, jog InGaN dažniausiai auginami ant skirtingą kristalinės gardelės periodą turinčių safyro padėklų. Dėl šios priežasties atsiranda vidiniai kristalo įtempimai, kurie lemia vidinių pjezoelektrinių laukų atsiradimą bei dislokacijų susiformavimą. Be to, dideli gardelės nesutapimai skatina didesnės indžio koncentracijos sričių formavimą (indžio segregaciją). Šios sritys neretai susiformuoja greta gardelės dislokacijų ir taip mažina struktūros efektyvumą [4]. Norint užauginti struktūras žalioje spektro srityje reikalinga įterpti didesnį In kiekį į InGaN struktūrą, o tam reikalinga auginimus atlikti žemesnėje temperatūroje [5]. Esant žemesnei auginimo temperatūrai ir didesnei In koncentracijai sumažėja In tirpumas, o dėl tarpsluoksniams naudojamų skirtingų medžiagų, išauga koherentiniai medžiagos įtempimai. Šie įtempimai lemia spinodinį medžiagos skylimą bei In atomų, esančių paviršiniame sluoksnyje segregaciją į didesnės In koncentracijos sritis ar atskiras In metalo salas [6]. Netolygus medžiagos pasiskirstymas lemia energijos juostų fliuktuacijas. Dėl šios priežasties emisijos spektras pasislenka į raudonąją sritį, o piko pusplotis (FWHM) išplinta. Dėl pjezoelektrinio efekto krūvininkai žaliuose šviestukuose turi ilgą gyvavimo trukmę, dėl kurios didelė dalis krūvininkų nepasiekia lokalizacijos centrų ir rekombinuoja nespinduliniu būdu [7].

Krūvininkai pasiekę lokalizacijos centrus lokalizuojasi, ko pasėkoje sumažėja bendras efektyvus liuminescencijos paviršiaus plotas, o tuo pačiu ir vidinis kvantinis našumas (IQE). Priedo, dėl to, jog dalyje lokalizacijos centrų egzistuoja dislokacijos, sumažėja tikimybė, jog lokalizuoti krūvininkai rekombinuos spinduliniu būdu, dėl ko dar labiau sumažėja IQE [8].

Ne paslaptis, jog egzistuoja keletas metodų leidžiančių užauginti struktūras pasižyminčias didesniu kvantiniu našumu. Vienas iš metodų, leidžiančių padidinti aktyviosios srities IQE, yra prieš kvantinės duobės auginimą trumpam į sistemą tiekti TMIn [9, 10]. Esant didesnei atominio In koncentracijai, In atomai gali sudaryti ryšius ties dislokacijos šerdimis, tokiu būdu sustabdant tolesnį dislokacijos plitimą daugybinių kvantinių duobių auginimo metu. Nors šis metodas ir leidžia padidinti IQE, tačiau jis nesumažina In segregacijos. Kitas metodas leidžiantis padidinti struktūros efektyvumą yra auginti InGaN ant pusiau-polinių GaN padėklų [11, 12]. Pusiau-polinių GaN padėklų gardelė yra artimesnė InGaN gardelei nei įprastai auginimams naudojamo c-plokštumos safyro. Dėl šios priežasties auginant InGaN ant pusiau-polinių GaN padėklų sluoksniai yra mažiau įtempti, o tai lemia pjezoelektrinio efekto sumažėjimą bei galimybę užauginti homogeniškus didesnės In koncentracijos InGaN sluoksnius. Deja, pusiau-poliniai GaN padėklai yra sąlyginai brangūs, dėl to išlieka paklausa ieškoti alternatyvių sprendimo būdų, leidžiančių sumažinti In segregaciją InGaN kvantinėse duobėse, auginamose ant c-plokštumos safyro padėklų. Alternatyvus sprendimo būdas galimai leidžiantis sumažinti In segregaciją yra kvantines duobes auginti naudojant MOVPE technologijai pritaikytą impulsinį auginimo metodą [13, 14]. Šis metodas paremtas principu, jog TMIn tiekimas yra periodiškai pertraukiamas, palaikant pastovų amoniako ir TMGa tiekimą. TMIn pertrūkio metu dalis In atomų desorbuojasi, dėl ko sumažėja nehomogeniškas In pasiskirstymas. Impulsinis auginimo metodas nėra pilnai ištirtas, kadangi nėra žinoma kokia yra impulsų trukmės, impulsų skaičiaus, pauzės tarp impulsų ir temperatūros įtaka kvantinių duobių struktūriniams ir optiniams parametrams. Pastarųjų impulsinio auginimo duomenų stoka paskatino šiame darbe ištirti bei visapusiškai įvertinti impulsinio auginimo parametrų įtaką InGaN kvantinių duobių struktūrai ir nustatyti optimalius impulsinio auginimo parametrus.

Darbo tikslas

Šio darbo tikslas buvo sukurti MOVPE impulsinio InGaN kvantinių duobių auginimo technologiją skirtą didesniam kvantinių duobių efektyvumui pasiekti ir pritaikyti šią technologiją žalių šviestukų struktūrų auginimui bei paaiškinti priežastis lėmusias optinių savybių pokyčius.

Disertacijos darbo uždaviniai suformuoti remiantis FP7 NEWLED projekto tikslu sukurti naujus technologinius metodus (In,Ga,Al)N ir (In,Ga,Al)(As,P) pagrindu regimojo spektro šviesos šviestukų struktūrų auginimui. Vienas iš projekto uždavinių buvo sukurti ir optimizuoti InGaN/GaN kvantinių duobių struktūrų MOVPE impulsinį auginimo būdą. Projekto metu vykdyti tyrimai ir gauti rezultatai pristatytas šioje disertacijoje.

Darbo uždaviniai

- Sukurti InGaN kristalinių sluoksnių MOVPE impulsinio auginimo technologiją skirtą Aixtron su dušo galvutės dujų tiekimo sistema tipo reaktoriui naudojant moduliuotą laike metalo-organikos prekursorių tiekimo metodą.
- Tiriant bandinių struktūrines bei optines savybes nustatyti optimalius laikinius MO srauto parametrus prie skirtingų auginimo temperatūrų, su kuriais užauginamos didžiausio intensyvumo InGaN/GaN kvantinių duobių struktūros.
- Charakterizuoti krūvininkų lokalizacijos profilį impulsiniu ir standartiniu būdu užaugintose InGaN kvantinėse duobėse.
- Pritaikyti optimizuotą impulsinį auginimo metodą didelio šviesos intensyvumo žalių InGaN šviestukų struktūrų auginimui.

Darbo naujumas ir svarba

Mūsų žiniomis, šiame darbe pirmą kartą atlikti nuodugnūs impulsinio auginimo metodo tyrimai parodant kokia yra InGaN auginimo parametrų (impulsų/pauzių trukmių bei temperatūros) įtaka struktūrinėms ir optinėms QW savybėms, kuomet auginimo parametrai keičiami palaipsniui. Taip pat nustatyti optimalūs impulsinio InGaN auginimo parametrai žalią šviesą spinduliuojančioms MQWs struktūroms.

Ginamieji teiginiai

- Didžiausias PL intensyvumo padidėjimas impulsiniu būdu užaugintose InGaN kvantinėse duobėse gaunamas kuomet pauzės trukmė optimizuojama atsižvelgus į auginimo temperatūrą bei vieno impulsinio auginimo ciklo metu užauga tarp 1 ir 4 InGaN monosluoksnių.

- Impulsinis auginimo metodas, kaip būdas padidinti kvantinių duobių liuminescencijos intensyvumą yra pranašesnis lyginant su kvantinių duobių auginimo temperatūros didinimu, abiem atvejais esant vienodai PL spektro smailės poslinkio į mėlynąją sritį vertei.

- PL intensyvumo padidėjimas impulsiniu būdu užaugintose InGaN kvantinėse duobėse yra susijęs su krūvininkų lokalizacijos potencialo pokyčiu dėl auginimo metu padidėjusios In atomų paviršinės migracijos ir mažesnio diametro, bet didesnio tankio daug In turinčių sričių kvantinėse duobėse susiformavimo.

1 EKSPERIMENTINĖS METODIKOS

1.1 Bandinių auginimas

InGaN kvantinių duobių struktūros (MQW) buvo auginamos ant safyro padėklų naudojant "AIXTRON", 2 in. skersmens 3 padėklų uždaro dušo galvutės tipo rektorių. Bandinių struktūrinė schema pateikta paveiksle 1.1. Bandiniai buvo sudaryti iš: safyro padėklo, 2µm storio GaN buferinio sluoksnio, kuriame 1,5 µm gylyje buvo suformuota 5 periodų ~12,5µm storio AlGaN/GaN supergardelė (SG). Toliau sekė 8 periodų 24nm storio InGaN/GaN SG legiruota Si, SG In koncentracija buvo ~5%. Galiausiai buvo suformuota daugybinė InGaN kvantinių duobių GaN (QW) bei GaN kvantinių barjerų (QB) 5 periodų struktūra, taipogi legiruota Si, o pabaigai padengtas GaN dengiamasis sluoksnis ("cap layer"). Metalo-organikos junginiai (MO): trimetil-galis (TMGa), trimetil-indis (TMIn), trimetil-aliuminis (TMAl) ir amoniakas buvo naudojami atitinkamai kaip Ga, In, Al ir N šaltiniai. Vandenilis buvo naudojamas GaN buferinio sluoksnio ir AlGaN SG auginimo metu kaip aplinkos dujos ir kaip dujos nešėjos. N_2 buvo naudojamos kaip aplinkos dujos ir kaip dujos nešėjos InGaN SG bei InGaN MQW auginimo metu.

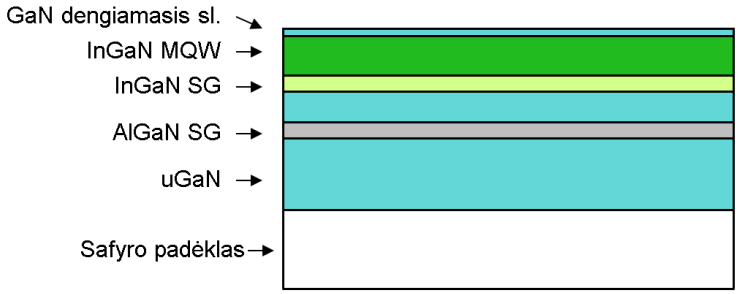

1.1 pav. Bandinius sudarančių sluoksnių struktūra.

Šio darbo metu buvo užauginti du pagrindiniai bandinių rinkiniai, kurių InGaN/GaN MQW buvo augintos T_{aug} = 780 ir 800 °C temperatūrose bei papildomi du bandinių rinkiniai, kurių InGaN QW buvo augintos T_{aug} = 810 ir 830 °C temperatūrose. QB visuose bandiniuose buvo auginami 850÷880 °C temperatūrų ribose.

Visų bandinių QW buvo auginamos impulsiniu būdu periodiškai įjungiant ir išjungiant TMIn ir TMGa tiekimą, o amoniako tiekimą išlaikant nepakitusį (paveiksle 1.2 pateikta dujų tiekimo schema). MO impulsų trukmė t_1 buvo keičiama nuo 5 iki 20 s, o pauzių trukmė t_2 – nuo 3 iki 20 s.

Palyginimui buvo užauginti penki palyginamieji bandiniai įprastiniu būdu, kurių QW auginimo metu buvo išlaikomas pastovus dujų tiekimas, kiekvieną bandinį auginant skirtingoje temperatūroje: T_{aug} = 780, 810 ir 830 °C. Visų bandinių, naudotų šiame darbe numeriai bei InGaN SG ir kvantinių duobių (MQW) auginimo parametrai pateikti lentelėje 1.1.

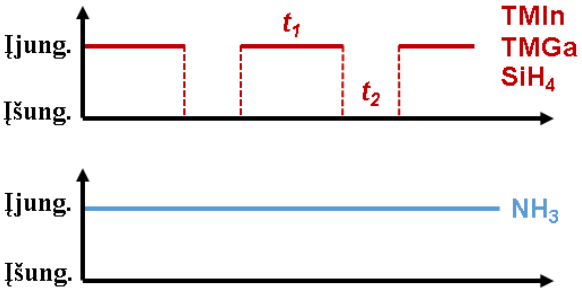

1.2 pav. Impulsinio auginimo dujų tiekimo schema.

1.2 Bandinių struktūrinių tyrimų metodikos

Bandinių struktūriniai parametrai buvo nustatomi naudojant elektronų pralaidumo mikroskopą (TEM), rentgeno spindulių difraktometrą (XRD) bei atominių jėgų mikroskopą (AFM).

TEM matavimai buvo atliekami naudojant *FEI Tecnai G2 F20 X-TWIN* mikroskopą su 200kV elektronų spinduliu. Šio darbo metu TEM matavimai buvo atliekami TEM bei skanuojančiu TEM (STEM) režimu.

XRD matavimams buvo pasitelktas *Rigaku, SmartLab* difraktometras. Bandiniai buvo analizuojami $K_{\alpha 1}$ (λ=1.56054Å) rentgeno spinduliais. Elementinė bandinių sudėtis buvo matuojama ω-2Θ režime ir analizuojama *GlobalFit* modeliavimo programa pritaikant sluoksnių storius išmatuotus su TEM. Vidiniai gardelės įtempimai buvo įvertinami atlikus atvirkštinės erdvės žemėlapių matavimus (RSM).

Bandinių paviršiaus savybėms nustatyti buvo atlikti AFM matavimai naudojant *Witec Alpha 300* mikroskopą veikiantį kontaktiniu rėžimu. Iš pastarųjų matavimų buvo apskaičiuotas bandinių vidutinis paviršiaus šiurkštumas bei vidutinis V-skylučių ir tranšėjinių defektų tankis.

Lentelė 1.1. InGaN kvantinių duobių auginimo parametrai.

Bandinio Nr.	t_1, s	t_2, s	Impulsai	T_{aug}, °C	T_{QB},°C	T_{SG},°C
S1(atr.)	80	0	1	800	840	850
S2	20	3	5	800	840	850
S3	20	6	5	800	840	850
S4	20	9	5	800	840	850
S5	20	12	5	800	840	850
S6	20	15	5	800	840	850
S7(atr.)	80	0	1	780	850	860
S8	5	3	20	780	850	860
S9	5	6	20	780	850	860
S10	5	9	20	780	850	860
S11	5	12	20	780	850	860
S12	5	15	20	780	850	860
S13	10	3	10	780	850	860
S14	10	6	10	780	850	860
S15	10	9	10	780	850	860
S16	10	12	10	780	850	860
S17	10	15	10	780	850	860
S18	20	3	5	780	850	860
S19	20	6	5	780	850	860
S20	20	9	5	780	850	860
S21	20	12	5	780	850	860
S22	20	15	5	780	850	860
S23(atr.)	80	0	1	810	850	860
S24	20	3	5	810	850	860
S25	20	6	5	810	850	860
S26	20	9	5	810	850	860
S27	20	12	5	810	850	860
S28	20	15	5	810	850	860
S29	20	20	5	810	850	860
S30(atr.)	80	0	1	830	870	880
S31	20	3	5	830	870	880
S32	20	6	5	830	870	880
S33	20	9	5	830	870	880
S34	20	12	5	830	870	880
S35	20	15	5	830	870	880
S36(atr.)	80	0	1	790	860	870

1.3 Bandinių optinių tyrimų metodikos

Bandinių optiniai parametrai buvo nustatomi atliekant foto-liuminescencijos (PL) bei foto-liuminescencijos su erdvine skyra (μPL) matavimus. PL matavimai buvo atliekami bandinius žadinant nuostovios veikos 405 nm bangos ilgio, 4 W/cm^2 galios tankio lazeriniu diodu (LD), o liuminescencija buvo registruojama *Princeton Instruments Acton SP2300* spektrometru ir analizuojama *Pixis 256* CCD kamera.

Temperatūriniai PL matavimai (TDPL) buvo atliekami nuostovaus žadinimo režime naudojant He-Cd lazerį (325 nm). Liuminescencija buvo registruojama dvigubu monochromatoriumi (*Jobin Yvon HRD-1*) ir detektuojama fotodaugintuvu (*Hamamatsu*). Matavimai buvo atliekami 8 ÷ 300 K temperatūros ribose, kuri buvo palaikoma uždaro ciklo helio kriostatu.

μPL matavimai buvo atliekami skanuojančiu konfokaliniu mikroskopu *Witec Alpha 300*. Bandinys buvo žadinamas LD (λ_{exc}=405 nm).

2 REZULTATAI

2.1 Struktūriniai tyrimai

Struktūriniai tyrimai buvo atlikti daliai pasirinktų bandinių. Visų pirma, siekiant nustatyti bandinių rinkinį pasižymintį geresnėmis optinėmis savybėmis lyginant su atraminiu bandiniu (stipri liuminescencija, siauras smailės pusplotis, smailė nėra žymiai pasislinkusi į mėlynąją sritį) buvo išmatuoti bandinių PL spektrai. Bandiniai auginti naudojant 20s impulsus pasižymėjo stipriausio intensyvumo PL smailėmis ties ciano (bandinių rinkinys augintas T_{growth}=800 ^{o}C) bei žalios spalvos sritimis (bandinių rinkinys augintas T_{growth}=780 ^{o}C). Toliau paprastumo dėlei bandinių rinkinys S1-S6 bus vadinamas "cianiniu rinkiniu" ir S7, S18-S22 bus vadinamas "žaliu rinkiniu". Cianiniai ir žali bandinių rinkiniai užauginti naudojant 20s impulsų trukmes buvo pasirinkti tolimesnei struktūrinei bandinių analizei.

Iš TEM ir STEM matavimų buvo nustatyti žalių bandinių S7, S21 ir cianinių bandinių S1, S2, S4, S5, S6 QW bei QB storiai ir pateikti lentelėje 2.1. Kaip pavyzdys paveiksle 2.1 pateikti atraminio bandinio S7 ir impulsiškai užauginto S21 bandinio TEM vaizdai. Buvo nustatyta, jog esant 0.02nm/s augimo tempui tikėtina, jog vieno t_1=20s arba t_1=10s impulso metu užaugo tarp 1 ir 4 InGaN monosluoksnių.

Toliau buvo atliekami XRD matavimai iš kurių buvo nustatoma QW ir SG vidutinė In koncentracija (apskaičiuoti In koncentracijos duomenys pateikti lentelė 2.1). Kaip pavyzdys paveiksle 2.2 pateiktos S7 ir S21 bandinio XRD svyravimo kreivės. Nustatyta, jog In koncentracija impulsiškai užaugintame žaliame bandinyje S21 sumažėja lyginant su atraminiu bandiniu S7. Manoma, jog viena priežasčių galėjusių lemti In koncentracijos sumažėjimą - dalies In desorbcija ilgesnių pauzių metu [102, 103]. Kitą vertus, neimpulsiškai užaugintuose bandiniuose buvo palankesnės sąlygos įtempimų relaksacijai formuojantis defektams, kurie palengvina In įterpimą [100, 101].

Tuo tarpu In koncentracijos skirtumas sumažėja tarp bandinių augintų su skirtingomis pauzių trukmėmis bei aukštesnėje temperatūroje (cianinio rinkinio). Tad galima teigti, jog In koncentracijos jautrumas impulsiniam auginimo metodui padidėja tik tuomet kai auginimai atliekami žemesnėje temperatūroje.

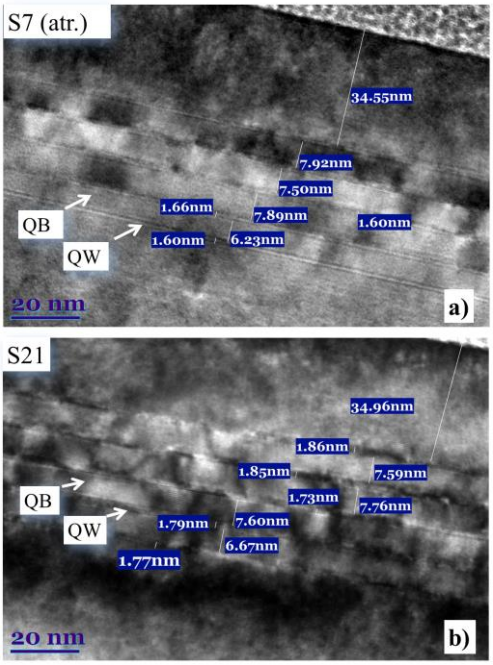

2.1 pav. TEM išmatuoti MQW skerspjūviai: a) atraminio bandinio S7, b) bandinio užauginto impulsiniu būdu S21 [PMD2].

Gardelės įtempimai ir In koncentracija buvo papildomai įvertinti atlikus RSM matavimus aplink (105) atspindį. Paveiksle 2.3 pateikti S7 ir S21 bandinių RSM vaizdai. Paveiksle 2.3 a) galima matyti, jog atraminio bandinio RSM atspindžių išsidėstymas (taškuota - punktyrinė linija) yra pasislinkęs nuo pilnai įtempto sluoksnio (punktyrinė linija atitinkanti GaN padėklo atvirkštinės gardelės taškus) link pilnai relaksavusio InGaN sluoksnio (ištisinė linija). Tikėtina, jog šią relaksaciją lėmė palankesnės defektų formavimo sąlygos, kuomet auginimai atliekami neimpulsiniu būdu [99]. Tuo tarpu impulsiškai užaugintos InGaN MQW buvo pilnai įtemptos (paveikslas 2.3 b).

Kitą vertus išmatavus cianinio bandinių rinkinio RSM buvo nustatyta, jog visų bandinių gardelės buvo pilnai arba beveik pilnai įtemptos. Tad stebėtai atraminio žalio bandinio relaksacijai lemiamą įtaką turėjo žemesnė auginimo temperatūra.

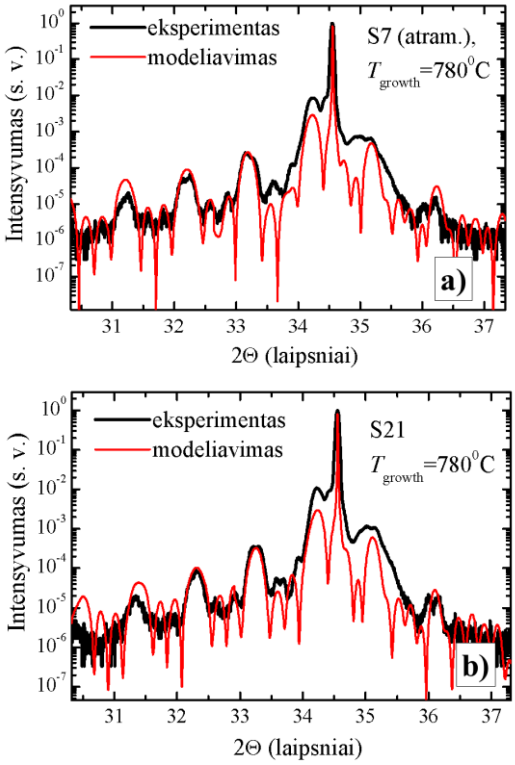

2.2 pav. XRD matavimo svyruojančios kreivės a) atraminio bandinio S7, b) bandinio užauginto impulsiniu būdu S21.

Lentelė 2.1 Išmatuoti pavienių sluoksnių storiai ir In koncentracija juose.

Bandinio Nr.	**S1**	**S2**	**S4**	**S5**	**S6**	**S7**	**S21**
d_{cap}, **nm**	28	28	28	28.5	28.5	34.5	35
d_{QB}, **nm**	6.6	6.7	7.2	6.7	6.8	7.4	7.4
d_{QW}, **nm**	3.8	4.1	3.8	4.1	4.1	1.6	1.8
$d_{InGaN\ SG}$, **nm**	1.8	1.8	1.85	1.85	1.85	1.8	1.8
$d_{GaN\ SG}$, **nm**	1.5	1.55	1.5	1.6	1.6	1.6	1.6
In X_{QW}	10.5%	10.5%	9.5%	10.0%	9.0%	27%	20%
In X_{SG}	5%	5%	4%	4%	4%	4%	4%

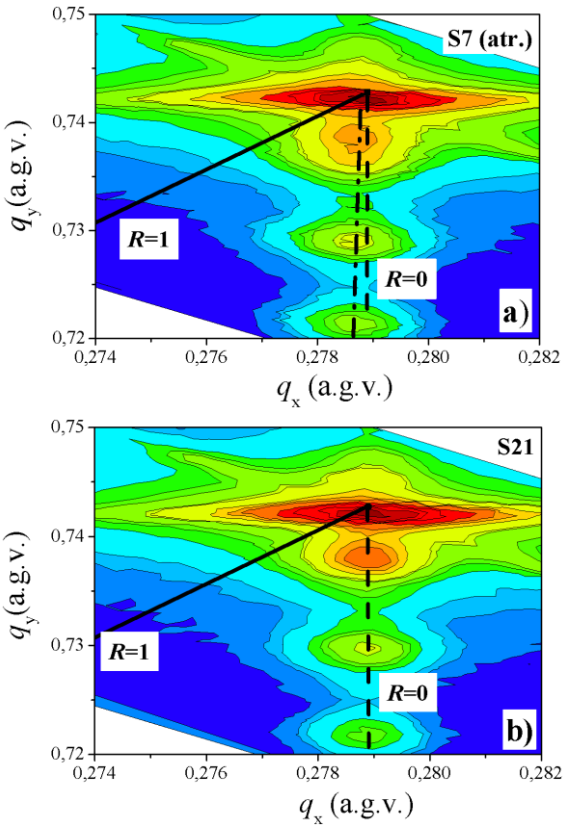

2.3 pav. RSM vaizdai išmatuoti aplink (105) atspindį a) atraminio bandinio S7, b) bandinio užauginto impulsiniu būdu S21. RSM ašys – atvirkštinės gardelės vienetai (a.g.v.). Punktyrinės linijos kertančios GaN padėklą atitinka pilnai įtemptą (R = 0) būseną. Punktyrinė – taškuota linija paveiksle a) atitinka dalinai atsipalaidavusį sluoksnį [PMD2].

Atlikus AFM matavimus buvo nustatytas bandinių paviršiaus šiurkštumas (lentelė 2.2). Pritaikius impulsinį auginimo metodą paviršiaus šiurkštumas šiek tiek padidėja lyginant su atraminiu bandiniu, tačiau aiškios tendencijos kokią įtaką impulsinis auginimas daro paviršiaus šiurkštumui nebuvo įžvelgta. Kaip pavyzdys paveiksle 2.4 pateikti S1 ir S3 bandinių AFM vaizdai.

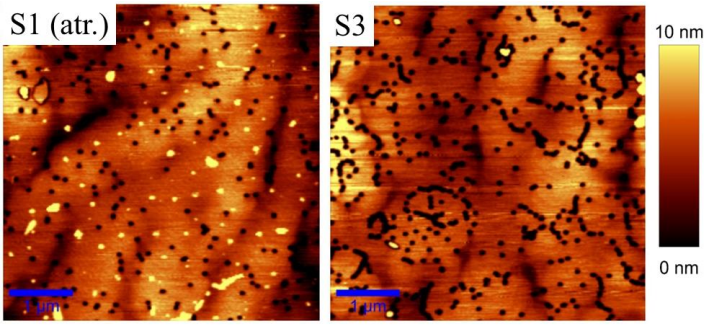

2.4 pav. AFM bandinių S1 ir S3 paviršiaus vaizdai [PMD2].

Lentelė 2.2. AFM išmatuoti atraminių (S1 ir S7) ir impulsiškai užaugintų bandinių (S2-S6, S21) paviršiaus šiurkštumai.

Bandiniai	**S1**	**S2**	**S3**	**S4**	**S5**	**S6**	**S7**	**S21**
Paviršiaus vidutinis šiurkštumas, nm	1.4	2.1	1.7	1.7	2.3	2.1	3.0	2.2

2.2 Optiniai tyrimai

PL spektrai buvo išmatuoti visiems bandiniams. Paveiksle 2.5 a) pateikti žalių bandinių PL spektrai. Galima matyti, jog didinant pauzės trukmę iki t_2=12s (S21 bandinys), PL spektrinis intensyvumas išauga virš dviejų kartų, o smailė pasislenka į mėlynąją sritį. Intensyvumo padidėjimą gali lemti arba sumažėjęs defektų tankis, lemiantis mažesnę nespindulinių rekombinacijos kanalų įtaką bandinio emisijai arba susidaręs palankesnis lokalizacijos potencialas. Didinant pauzės trukmę iki t_2 = 15s lokalizacijos potencialas sumažėja ir PL intensyvumas pradeda kristi.

Vienas gerai žinomų metodų PL intensyvumui padidinti yra kvantines duobes auginti aukštesnėje temperatūroje. Paveiksle 2.5 b) pateikti PL spektrai išmatuoti įprastiniu būdų užaugintuose atraminiuose bandiniuose taikant skirtingas kvantinių duobių auginimo temperatūras (780÷800 ^{o}C). Auginimo temperatūrą pakėlus 10 ^{o}C (nuo 780 iki 790 ^{o}C), integruotas PL intensyvumas išaugo ~1,2 kartus, o spektrinė smailė pasislinko ~9 nm. Pastarojo bandinio (S36) PL spektrinis poslinkis yra panašus į aukščiausią PL intensyvumą turinčio impulsiškai užauginto bandinio S21 spektrinį poslinkį (~8nm). Tačiau atraminio bandinio auginto aukštesnėje temperatūroje PL intensyvumo padidėjimas sudarė tik 12% PL intensyvumo padidėjimo impulsiškai užaugintame bandinyje. Arba kitaip tariant impulsiškai užauginto bandinio PL intensyvumas išauga 7 kartus daugiau nei auginimus atliekant įprastu auginimo metodu, bet aukštesnėje temperatūroje.

Paveiksle 2.6 a) galima matyti, jog taikant trumpesnes impulsų trukmes (t_1 = 5, 10 s), integruoto intensyvumo stiprėjimo tendencija, ilginant pauzės trukmę išlieka, tačiau maksimaliai pasiekiama integruoto intensyvumo vertė mažėja ir yra pasiekiama ties trumpesnėmis pauzėmis. Impulsų trukmės mažinimas taipogi lemia vis stipresnį PL smailės padėties poslinkį į mėlynąją sritį (2.6 b)).

Toliau buvo įvertinta žalio bandinių rinkinio impulsų trukmės įtaką PL charakteristikoms. Paveiksle 2.6 pateiktos a) PL intensyvumo, b) PL smailės padėties bei c) puspločio priklausomybės nuo pauzės trukmės esant skirtingoms impulsų trukmėms (t_1 = 5, 10, 20 s).

Tuo tarpu pusplotis esant trumpesniems impulsams (t_1 = 5, 10 s) išlieka beveik nepakitęs (2.6 c)). Verta pastebėti, jog t_1 = 20s pusplotis ties t_2 = 3s smarkiai išauga, o vis labiau ilginant pauzės trukmei sumažėja iki pradinės atraminio bandinio vertės. Toks reiškinys galimai siejamas su padidėjusia In desorbcija iš defektuotų sričių ir naujų skirtingo gylio spindulinės rekombinacijos centrų formavimu.

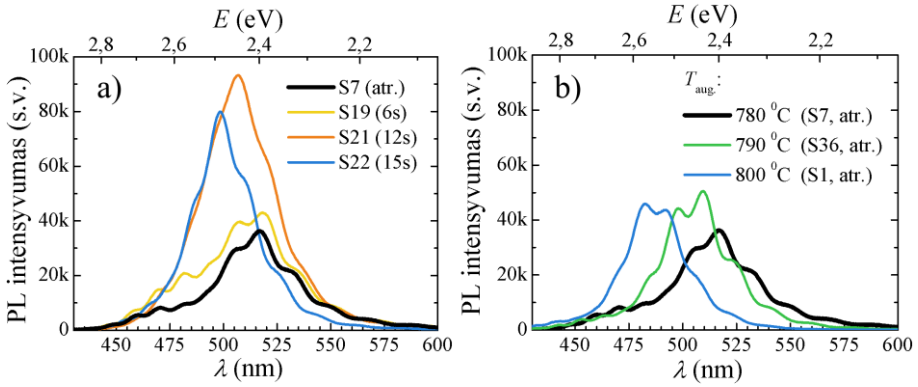

2.5 pav. Kambario temperatūros PL matavimai a) impulsiškai ir neimpulsiškai užaugintų žalių bandinių, b) atraminių bandinių augintų skirtingose temperatūrose [PMD2].

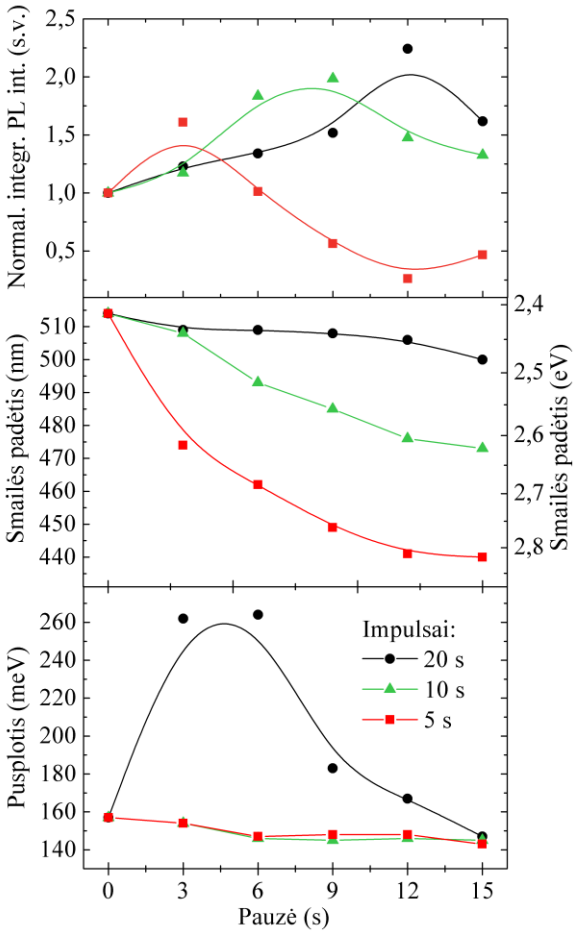

2.6 pav. Žalio bandinių rinkinio normalizuota integruota PL amplitudė, PL smailės padėtis ir smailės pusplotis kaip priklausomybė nuo auginimo pauzės trukmės esant skirtingiems auginimo impulsų intervalams. Juodi, žali ir raudoni simboliai žymi impulsiškai užaugintus bandinius su 20s (S18÷S22), 10s (S13÷S17) ir 5s (S8÷S12) impulsais bei atraminį bandinį S7. Linijomis pažymėtos tendencijos [PMD2].

Paveiksle 2.7 pateikti cianinio bandinių rinkinio PL spektrai, o paveiksle 2.8 apibendrintos PL spektrų vertės. Cianiniuose bandiniuose kaip ir žaliuose didėjant impulsinio auginimo pauzės trukmei išauga PL intensyvumas iki dviejų kartų, tačiau maksimalios PL vertės pasiekiamos jau ties 9s pauzės trukme (S4 bandinys) ir išlieka panašios iki 15s. Tuo tarpu PL smailės padėtis pasižymi tendencija slinkti į mėlynąją spektro pusę iki 10nm skirtumo bandinyje S6 lyginant su atraminiu bandiniu S1. Spektro pusplotis išlaiko tendenciją didėti sulig pauzės trukmės

augimu nuo 151 meV (S1) iki 166 meV. Kadangi In koncentracijos ir QW storio vertės išliko panašios visuose bandiniuose, PL spektro pokyčius tikėtina lėmė lokalizacijos potencialo arba NRC tankio modifikacija.

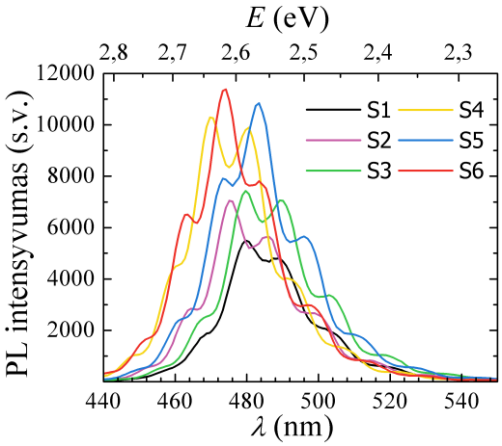

2.7 pav. Kambario temperatūros PL matavimai impulsiškai ir neimpulsiškai užaugintų cianinių bandinių.

Siekiant įvertinti auginimo temperatūros įtaką impulsiniam auginimui buvo atlikta bandinių su t_1=20s impulsų trukme, užaugintų 780 °C, 810 °C ir 830 °C temperatūrose, PL spektrų analizė.

Paveiksle 2.9 galima stebėti, jog auginimo temperatūros kėlimas turi panašią įtaką PL charakteristikoms kaip ir impulsų trukmės mažinimas. Kuo aukštesnė impulsinio auginimo temperatūra (810, 830 °C), tuo mažesnė maksimali impulsinio auginimo PL intensyvumo vertė, o spektras vis labiau pasislinkęs į mėlynąją sritį. Tuo tarpu pusplotis pakeliant auginimo temperatūrą nuo 780 °C iki 810 °C sumažėja, o keliant temperatūrą iki 830 °C išlieka beveik panašus kaip ir 810 °C temperatūros atveju.

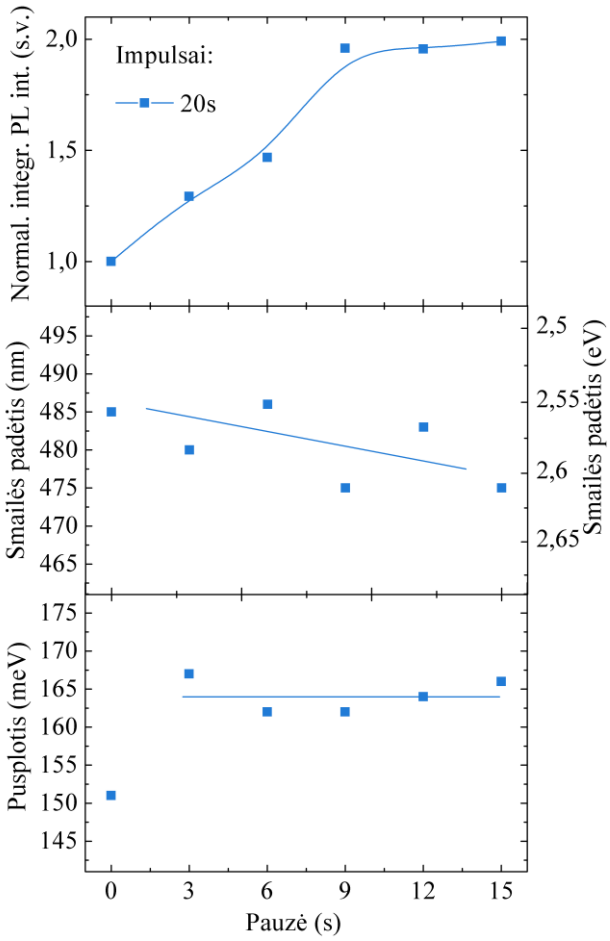

2.8 pav. Cianinio bandinių rinkinio normalizuota integruota PL amplitudė, PL smailės padėtis ir smailės pusplotis kaip priklausomybės nuo auginimo pauzės trukmės. Tirti bandiniai su 20s auginimo impulsais (S2÷S6) bei atraminis bandinys S1. Linijos žymi tendencijas.

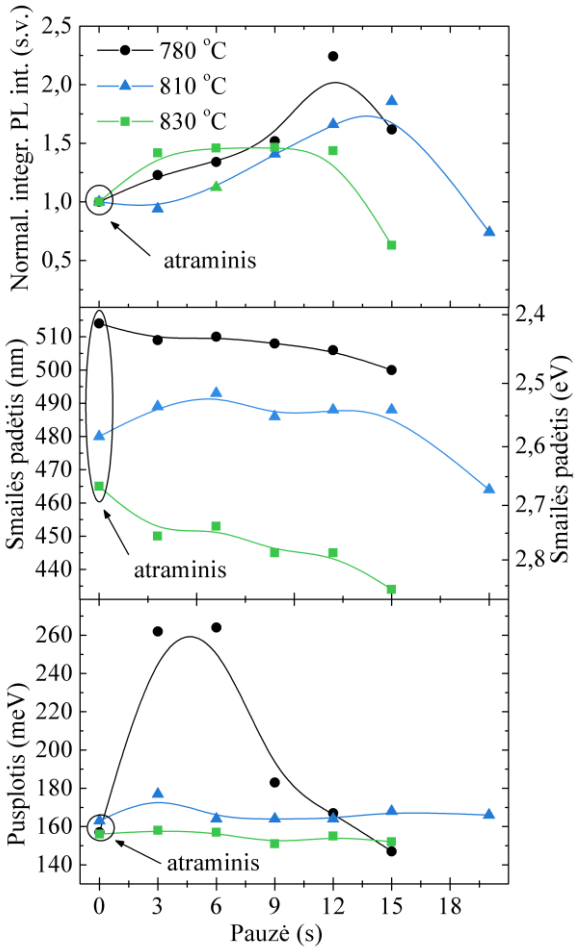

2.9 pav. Normalizuotų integruotų PL amplitudžių, PL piko padėčių bei puspločių priklausomybės nuo pauzės trukmės esant skirtingoms QW auginimo temperatūroms: 780 °C (S7, S18÷S22), 810 °C (S23÷29) ir 830 °C (S30÷S35). Linijos žymi tendencijas.

2.3 Krūvininkų lokalizacija InGaN MQW

Siekiant įvertinti krūvininkų lokalizacijos specifikas buvo išmatuotos PL smailės padėties priklausomybės nuo matavimo temperatūros ir atidėtos paveiksle 2.10. Galima matyti, jog kreivės turi S-formos tendencijas kurios yra įprasta III-N trinarių junginių temperatūrinės PL smailių priklausomybėms [109]. Didėjant pauzės trukmei pastebimos dvi S-formos pokyčio tendencijos – išauga pradinio raudonojo poslinkio vertės bei sumažėja mėlynasis poslinkis. Didesnis pradinis raudonasis poslinkis atsiranda dėl didesnės gilių lokalizacijos būsenų

koncentracijos. Šią idėją papildo mėlynojo poslinkio sumažėjimas, atsirandantis dėl didesnės gilių būsenų ir mažesnės seklių būsenų koncentracijos. Atsižvelgiant į prieš tai rezultatuose stebėtą tendenciją, jog didinant pauzės trukmę PL smailės padėtis slenka į mėlynąją sritį, galima daryti išvadą, jog impulsinis auginimo metodas sukuria daugiau gilių būsenų, tačiau skirtumas tarp gilių būsenų padėties ir juostos judrumo krašto sumažėja.

Priedo prie šių rezultatų buvo paskaičiuotos draustinių juostų tarpo fliuktuacijų Gauso pasiskirstymo standartinio nuokrypio σ vertės, kurios leidžia įvertinti In koncentracijos arba/ir sluoksnio storio fliuktuacijas. Impulsiškai užaugintuose bandiniuose σ vertės beveik nesiskyrė ir buvo ~ 28meV. Tuo tarpu atraminio bandinio standartinis nuokrypis buvo šiek tiek mažesnis ~25meV, kadangi S-formos kilpos taškas buvo ties žemesne temperatūra. Panašios In koncentracijos vertės, mažas skirtumas tarp σ verčių ir prieš tai minėti spektriniai pokyčiai leidžia manyti, jog PL intensyvumas išauga pagrinde dėl lokalizacijos potencialo pokyčių.

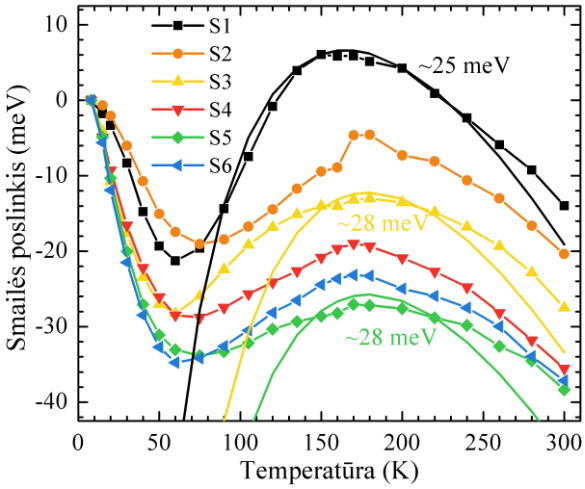

2.10 pav. S-formos temperatūrinės PL smailės padėties priklausomybės InGaN MQW. Ištisinės kreivės yra Varšni aproksimacijos, virš kreivių pateiktos Gauso pasiskirstymo standartinio nuokrypio *σ* vertės.

Siekiant tiksliau įvertinti lokalizacijos potencialo savybes ir kokią įtaką jo pokyčiams turi impulsinis auginimo metodas cianiniam bandinių rinkiniui buvo atlikti µPL matavimai. Paveiksle 2.11 pateikti S2 bandinio µPL matavimo rezultatai: 2.11 a) PL intensyvumo pasiskirstymas, b) spektrinis pasiskirstymas ir c) atsitiktinių taškų parinktų iš µPL žemėlapio PL spektrai. Galima matyti paveiksle 2.11 a), jog PL intensyvumas pasiskirstęs netolygiai – didesnio intensyvumo sritys pasiskirsčiusios žemesnio intensyvumo fone. Spektrinis pasiskirstymas paveiksle

2.11 b) taip pat netolygus. Atsitiktinai pasirinktuose matavimo taškų spektruose (2.11 c)) atsiranda papildoma smailė, pasislinkusi į raudonąją sritį ir lemianti bendrą spektro išplitimą. Jei šios smailės intensyvumas pakankamai didelis ji gali lemti bendro spektro vidutinės padėties poslinkį į raudonąją sritį. Tokios sritys, pasižyminčios stipriu spektriniu poslinkiu į raudonąją sritį dažnai egzistuoja artimoje V-tipo skylučių aplinkoje [114]. Atsižvelgus į sritis turinčias didesnį pusplotį nei 1,5 standartinio puspločio nuokrypio buvo nustatyta, jog tokios sritys užima tik 3-4% bendro paviršiaus ploto ir nedaro didelės įtakos bendram PL spektrui.

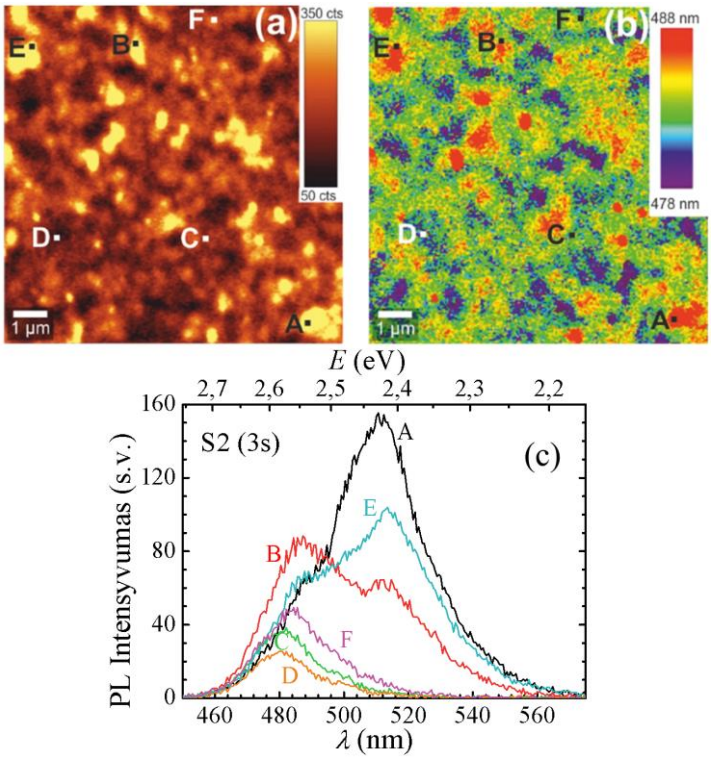

2.11 pav. µPL bandinio S2 matavimų rezultatai: a) spektriškai integruoto PL intensyvumo erdvinis pasiskirstymas 10×10 μm^2 ploto erdvėje, b) PL piko bangos ilgio erdvinis pasiskirstymas ir c) atskirų taškų (A-D) spektriniame pasiskirstyme PL spektrai.

Nustačius, jog spektriniai pokyčiai, pritaikius impulsinį auginimo metodą, tikėtiniausia pasireiškia dėl pokyčių giliose lokalizacijos srityse, toliau buvo

atliekama analizė kaip keitėsi gilios lokalizacijos sritys didinant impulsinio auginimo pauzės trukmę.

Kiekviename cianinio bandinio μPL paveiksle buvo paskaičiuota kiek konkretaus bandinio atveju buvo registruota atitinkamo bangos ilgio ir intensyvumo pikselių. Gautas pikselių pasiskirstymas buvo atidėtas grafiškai (paveiksle 2.12 pateikti atraminio S1 ir impulsinio S5 bandinių matavimų rezultatai). Tuomet buvo paskaičiuoti vidutiniai bangos ilgiai giliose lokalizacijos

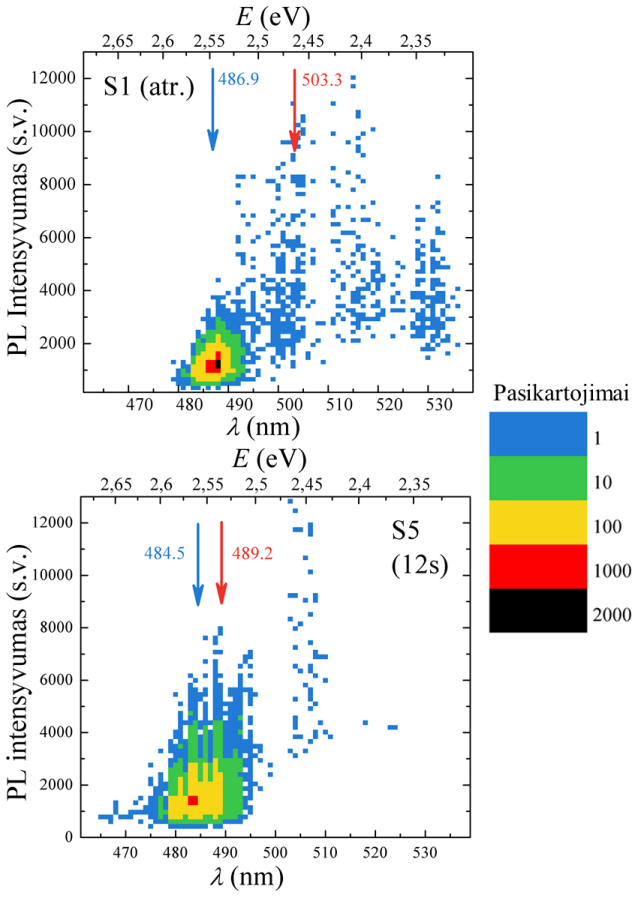

2.12 pav. Spektrinis pikselių intensyvumo ir skaičiaus išsidėstymas atraminiame bandinyje S1 ir impulsiškai užaugintame bandinyje S5. Mėlynos rodyklės žymi absoliutų spektro vidutinį bangos ilgį, raudonos rodyklės – vidutinį bangos ilgį giliose lokalizacijos srityse.

srityse įtraukiant tik sritis turinčias didesnį nei standartinio nuokrypio bangos ilgį ir pažymėti raudonomis rodyklėmis (mėlynos rodyklės žymi bendrą kiekvieno bandinio vidutinę PL smailės padėtį). Paveiksle 2.12 galima matyti, jog lyginant

impulsiškai užaugintą bandinį su atraminiu, skirtumas tarp bendro spektro vidutinio bangos ilgio ir vidutinio bangos ilgio giliose lokalizacijos srityse sumažėja nuo 16.4 iki 4.7 nm. Tai patvirtina pirminę idėją, jog impulsinis auginimo metodas sumažina skirtumą tarp gilių lokalizacijos sričių ir juostos judrumo krašto. Taip pat galima matyti, jog pikselių išsibarstymas ties ilgesniais bangos ilgiais sumažėja – lokalizacijos sritys tampa homogeniškesnės.

Toliau tęsiant gilių lokalizacijos sričių analizę buvo paskaičiuota kokį paviršiaus plotą užima sritys su bangos ilgiu didesniu nei standartinis nuokrypis. Kaip palyginimas atraminio bandinio ir vieno iš impulsinio bandinio spektrinio µPL pasiskirstymo bei gilių lokalizacijos sričių išsidėstymas pateiktas paveiksle 2.13. Buvo paskaičiuotas, jog vidutinis lokalizacijos sričių plotas sumažėja, tačiau jų skaičius išauga ir tuo pačiu padidėja bendras gilių lokalizacijos sričių užimamas plotas nuo 2 iki 14,5 µm^2 lyginant atitinkamai bandinius S1 ir S5. Tad galima teigti, jog padidėjęs gilesnių lokalizacijos sričių skaičius buvo pagrindinė priežastis lėmusi PL integruoto intensyvumo padidėjimą iki 2 kartų.

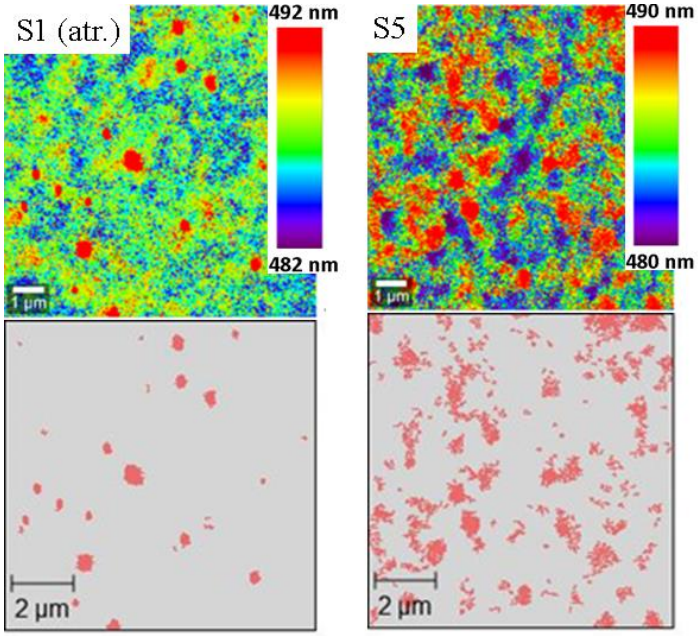

2.13 pav. Atraminio bandinio S1 ir impulsiškai užauginto bandinio S5 spektrinis pasiskirstymas (viršuje) ir sritys su bangos ilgiu didesniu nei standartinis nuokrypis (apačioje).

2.4 Impulsinio auginimo taikymas LED struktūroms

Išdirbus impulsinio auginimo technologiją, ji buvo pritaikyta LED struktūros auginimui. Viso buvo užaugintos 3 LED struktūros (LED1, LED2, LED3) identiškomis sąlygomis išskyrus kvantinių duobių auginimo temperatūras, kurios buvo 793 °C, 797 °C ir 803 °C, atitinkamai LED1, LED2 ir LED3 bandiniams. LED struktūros buvo sudarytos iš 2.5 µm uGaN sluoksnio su AlGaN/GaN SG, 1,2 µm nGaN sluoksniu, 4nm InGaN/GaN SG, 3 periodai QW d_{QW}=(3÷4)nm, In=(15÷20)%, d_{QB}=6nm, ~25 nm pAlGaN sluoksnio ir 200nm pGaN sluoksnio. QW buvo auginamos impulsiniu būdu taikant šešis 15s impulsus ir 12s pauzes tarp impulsų.

LED struktūrų optiniai matavimai buvo atliekami "TopGaN" kompanijoje. Paveiksle 2.14 pateikti trijų bandinių elektroliuminescencijos (EL) spektrai. EL buvo matuojama fiksuojant 20mA srovę ir registruojant EL spektrą sferoje.

Tikėtina, jog aukštesnė QW auginimo temperatūrą lėmė mažesnę QW In koncentraciją, dėl ko pagerėjo aktyviosios srities kristalinė kokybė (sumažėjo defektų), o tai lėmė spektrinio intensyvumo padidėjimą, tačiau tuo pačiu ir spektro smailės poslinkį į mėlynąją sritį.

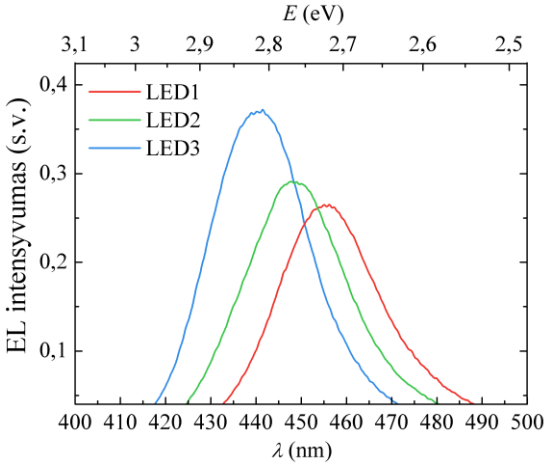

2.14 pav. LED struktūrų EL.

Toliau, buvo paskaičiuoti LED struktūrų efektyvumai. Pastarieji skaičiavimai buvo atlikti "STR" kompanijoje. Išmatavus išorinį kvantinį našumą (EQE) bei atlikus ABC modelio skaičiavimus, buvo paskaičiuotas vidinis kvantinis našumas (IQE) [121]. Žinant EQE ir IQE buvo rastas šviesos ištrūkos efektyvumas (LEE). Paskaičiuotos efektyvumų vertės pateiktos lentelėje 2.3. Galima pastebėti, jog EQE vertės labai mažos, tačiau kadangi EQE tiesiogiai susijęs su LEE ir IQE, galima matyti, jog labai mažos LEE vertės lėmė mažas EQE vertes.

2.3 lentelė: LED struktūrų apskaičiuoti efektyvumai.

Bandinys	LED1	LED2	LED3
λ, nm	455	447	443
IQE max, %	28,6	35,5	42,8
EQE max, %	1,5	1,3	2,0
LEE, %	4,5	4,4	4,6

IŠVADOS

1. PL intensyvumą InGaN QWs galima padidinti jei vieno auginimo impulso metu InGaN užauga nemažiau kaip 1 kristalinis monosluoksnis. Naudojant penkis 20s impulsus, 12s (9s) pauzes, 780 ^{o}C (800 ^{o}C) temperatūroje užaugintų žalios (ciano) spalvos šviesą spinduliuojančių InGaN QW PL intensyvumas buvo 2 kartus didesnis lyginant su standartiniu būdu užaugintomis struktūromis, PL spektro smailei nežymiai pasislenkant į mėlynąją spektro sritį.

2. Impulsinis auginimo metodas, kaip būdas užauginti InGaN kvantines duobes su didesniu PL efektyvumu yra pranašesnis nei kvantinių duobių auginimas aukštesnėje temperatūroje standartiniu būdu. Impulsiniu būdu užaugintų InGaN QW PL intensyvumo procentinis padidėjimas yra 7 kartus didesnis nei QW, užaugintų aukštesnėje temperatūroje neimpulsiniu būdu, abiem atvejais esant vienodam PL spektro smailės poslinkiu į mėlynąją spektro sritį.

3. Naudojant trumpesnius auginimo impulsus (<20s), tačiau nekeičiant pauzių (12s), padidėja In atomų desorbcija ypač iš didesnę In koncentraciją turinčių sričių, lemianti mažesnį tankį bei seklesnes lokalizuojančias būsenas. Dėl to sumažėja PL intensyvumas, o spektro smailė pasislenka į mėlynąją sritį.

4. Naudojant 20s impulsus ir ilginant pauzės trukmę (≥9 s) padidėja didesnį In kiekį turinčių sričių tankis, dėl ko išauga lokalizuotų būsenų tankis lemiantis PL intensyvumo padidėjimą (~2 kartus). Tuo tarpu vidutinė In koncentracija gilias lokalizacijos būsenas turinčiose srityse sumažėja, tad vidutinė gilių lokalizuotų būsenų energija pasislenka link judrumo krašto, o spektro smailės padėtis pasislenka į mėlynąją sritį (~8nm).

5. InGaN QW impulsinis auginimo metodas buvo pritaikytas technologiniuose tyrimuose pilnos šviestuko struktūros auginimuose.

TRUMPOS ŽINIOS APIE DISERTANTĄ

Vardas Pavardė	Mantas Dmukauskas
Gimimo data	1990 08 30
El. paštas	mantasdmuk@gmail.com
Santrauka	Fizikos doktorantūros kandidatas su 10 metų laboratorinių tyrimų patirtimi optoelektronikos srityje. Ekspertizės sritis apima III-N medžiagų auginimą, charakterizavimą bei prietaisų kūrimą (šviestukai ir detektoriai). Bendradarbiavimo patirtis su multidisciplininėmis ir tarptautinėmis grupėmis. Įgūdžiai: kristalinių struktūrų auginimas taikant MOVPE technologiją, medžiagos ir defektų charakterizavimas (PL, SEM, TEM, XRD), ataskaitų ir publikacijų rašymas bei patentų analizė.
Išsilavinimas	2015-2019 Doktorantūra, Fizika, Vilniaus Universitetas, Vilnius 2013-2015 Magistrantūra, Optoelektronika, Vilniaus Universitetas, Vilnius 2009-2013 Bakalauro studijos, Taikomoji fizika, Vilniaus Universitetas, Vilnius 2009 Vidurinis išsilavinimas, Kauno jėzuitų gimnazija, Kaunas
Darbo patirtis	2017-2018 Jaunesnysis mokslo darbuotojas, Vilniaus Universitetas, Vilnius 2013-2017 Inžinierius, Vilniaus Universitetas, Vilnius 2010-2013 Technikas, Vilniaus Universitetas, Vilnius
Publikacijos	9 publikacijos (ISI), 19 pristatymų (žod. ir stend.)

REFERENCES

[1] S. Nakamura, N. Senoh, N. Iwasa, S.I. Nagahama, High-brightness ingan blue, green and yellow light-emitting-diodes with quantum-well structures, Japanese Journal of Applied Physics Part 2-Letters & Express Letters, 34 (1995) L797-L799.

[2] J.Y. Tsao, M.H. Crawford, M.E. Coltrin, A.J. Fischer, D.D. Koleske, G.S. Subramania, G.T. Wang, J.J. Wierer, R.F. Karlicek, Toward Smart and Ultra-efficient Solid-State Lighting, Advanced Optical Materials, 2 (2014) 809-836.

[3] S. Nakamura, T. Mukai, M. Senoh, High-power gan p-n-junction blue-light-emitting diodes, Japanese Journal of Applied Physics Part 2-Letters & Express Letters, 30 (1991) L1998-L2001.

[4] Z. Deng, Y. Jiang, W.X. Wang, L.W. Cheng, W. Li, W. Lu, H.Q. Jia, W.M. Liu, J.M. Zhou, H. Chen, Indium segregation measured in InGaN quantum well layer, Scientific Reports, 4 (2014).

[5] M.S. Kumar, Y.S. Lee, J.Y. Park, S.J. Chung, C.H. Hong, E.K. Suh, Surface morphological studies of green InGaN/GaN multi-quantum wells grown by using MOCVD, Materials Chemistry and Physics, 113 (2009) 192-195.

[6] Y.S. Lin, K.J. Ma, C. Hsu, S.W. Feng, Y.C. Cheng, C.C. Liao, C.C. Yang, C.C. Chou, C.M. Lee, J.I. Chyi, Dependence of composition fluctuation on indium content in InGaN/GaN multiple quantum wells, Applied Physics Letters, 77 (2000) 2988-2990.

[7] A. Kaneta, M. Funato, Y. Kawakami, Nanoscopic recombination processes in InGaN/GaN quantum wells emitting violet, blue, and green spectra, Physical Review B, 78 (2008).

[8] N. Duxbury, U. Bangert, P. Dawson, E.J. Thrush, W. Van der Stricht, K. Jacobs, I. Moerman, Indium segregation in InGaN quantum-well structures, Applied Physics Letters, 76 (2000) 1600-1602.

[9] M.S. Kumar, J.Y. Park, Y.S. Lee, S.J. Chung, C.H. Hong, E.K. Suh, Improved internal quantum efficiency of green emitting InGaN/GaN multiple quantum wells by in preflow for InGaN well growth, Japanese Journal of Applied Physics, 47 (2008) 839-842.

[10] Y.J. Lee, Y.C. Chen, T.C. Lu, Improvement of quantum efficiency in green light-emitting diodes with pre-TMIn flow treatment, Journal of Physics D-Applied Physics, 44 (2011).

[11] M. Funato, A. Kaneta, Y. Kawakami, Y. Enya, K. Nishizuka, M. Ueno, T. Nakamura, Weak Carrier/Exciton Localization in InGaN Quantum Wells for Green Laser Diodes Fabricated on Semi-Polar {2021} GaN Substrates, Applied Physics Express, 3 (2010).

[12] M. Ueno, Y. Yoshizumi, Y. Enya, T. Kyono, M. Adachi, S. Takagi, S. Tokuyama, T. Sumitomo, K. Sumiyoshi, N. Saga, T. Ikegami, K. Katayama, T. Nakamura, InGaN-based true green laser diodes on novel semi-polar {2021} GaN substrates, Journal of Crystal Growth, 315 (2011) 258-262.

[13] C.H. Du, Z.G. Ma, J.M. Zhou, T.P. Lu, Y. Jiang, P. Zuo, H.Q. Jia, H. Chen, Enhancing the quantum efficiency of InGaN yellow-green light-emitting diodes by growth interruption, Applied Physics Letters, 105 (2014).

[14] M. Dmukauskas, A. Kadys, T. Malinauskas, T. Grinys, I. Reklaitis, K. Badokas, M. Skapas, R. Tomasiunas, D. Dobrovolskas, S. Stanionyte, I. Pietzonka, M. Strassburg, H.J. Lugauer, Influence of metalorganic precursors

flow interruption timing on green InGaN multiple quantum wells, Journal of Physics D-Applied Physics, 49 (2016).
[15] J. Patterson, B.C. Bailey, Solid-State Physics Introduction to the Theory, Springer-Verlag Berlin Heidelberg (2010).
[16] Peter YU, M. Cardona, Fundamentals of Semiconductors: Physics and Materials Properties, Springer Berlin Heidelberg, (2005).
[17] H. Ibach, H. Lüth, Solid-State Physics An Introduction to Principles of Materials Science, (2009).
[18] M. Goiran, M. Millot, J.M. Poumirol, I. Gherasoiu, W. Walukiewicz, J. Leotin, Electron cyclotron effective mass in indium nitride, Applied Physics Letters, 96 (2010).
[19] H. Morkoç, Handbook of Nitride Semiconductors and Devices, Materials Properties, Physics and Growth, Wiley (2009).
[20] G. Orsal, Y. El Gmili, N. Fressengeas, J. Streque, R. Djerboub, T. Moudakir, S. Sundaram, A. Ougazzaden, J.P. Salvestrini, Bandgap energy bowing parameter of strained and relaxed InGaN layers, Optical Materials Express, 4 (2014) 1030-1041.
[21] Safa Kasap, P. Capper, Springer Handbook of Electronic and Photonic Materials, Springer International Publishing (2017).
[22] O. Ambacher, J. Smart, J.R. Shealy, N.G. Weimann, K. Chu, M. Murphy, W.J. Schaff, L.F. Eastman, R. Dimitrov, L. Wittmer, M. Stutzmann, W. Rieger, J. Hilsenbeck, Two-dimensional electron gases induced by spontaneous and piezoelectric polarization charges in N- and Ga-face AlGaN/GaN heterostructures, Journal of Applied Physics, 85 (1999).
[23] U.W. Pohl, Epitaxy of Semiconductors: Introduction to Physical Principles, Springer Berlin Heidelberg (2013).
[24] A. Zoroddu, F. Bernardini, P. Ruggerone, V. Fiorentini, First-principles prediction of structure, energetics, formation enthalpy, elastic constants, polarization, and piezoelectric constants of AlN, GaN, and InN: Comparison of local and gradient-corrected density-functional theory, Physical Review B, 64 (2001).
[25] N.A. Fichtenbaum, C. Schaake, T.E. Mates, C. Cobb, S. Keller, S.P. DenBaars, U.K. Mishra, Electrical characterization of p-type N-polar and Ga-polar GaN grown by metalorganic chemical vapor deposition, Applied Physics Letters, 91 (2007).
[26] F. Bernardini, V. Fiorentini, D. Vanderbilt, Spontaneous polarization and piezoelectric constants of III-V nitrides, Physical Review B, 56 (1997).
[27] S. Mokkapati, C. Jagadish, III-V compound SC for optoelectronic devices, Materials Today, 12 (2009) 22-32.
[28] D.-J. Kim, Y.-T. Moon, K.-M. Song, I.-H. Lee, S.-J. Park, Effect of growth pressure on indium incorporation during the growth of InGaN by MOCVD, Journal of Electronic Materials, 30 (2001) 99-102.
[29] J. Nord, K. Albe, P. Erhart, K. Nordlund, Modelling of compound semiconductors: analytical bond-order potential for gallium, nitrogen and gallium nitride, Journal of Physics: Condensed Matter, 15 (2003) 5649-5662.
[30] D.D. Koleske, J.J. Wierer, A.J. Fischer, S.R. Lee, Controlling indium incorporation in InGaN barriers with dilute hydrogen flows, Journal of Crystal Growth, 390 (2014) 38-45.

[31] Jian-Jang Huang, Hao-Chung Kuo, S.-C. Shen, Nitride Semiconductor Light-Emitting Diodes (LEDs): Materials, Technologies and Applications, Elsevier Science (2014).
[32] N. Yoshimoto, T. Matsuoka, T. Sasaki, A. Katsui, Photoluminescence of InGaN films grown at high temperature by metalorganic vapor phase epitaxy, Applied Physics Letters, 59 (1991) 2251-2253.
[33] S. Kasap, P. Capper, Springer Handbook of Electronic and Photonic Materials, Springer, US, (2006).
[34] A. Hirako, K. Kusakabe, K. Ohkawa, Modeling of reaction pathways of GaN growth by metalorganic vapor-phase epitaxy using TMGa/NH3/H-2 system: A computational fluid dynamics simulation study, Japanese Journal of Applied Physics Part 1-Regular Papers Brief Communications & Review Papers, 44 (2005) 874-879.
[35] Dirk Ehrentraut, Elke Meissner, M. Bockowski, Technology of Gallium Nitride Crystal Growth, Springer, Berlin Heidelberg (2010).
[36] H.K. Choa, J.Y. Lee, C.S. Kim, G.M. Yang, N. Sharma, C. Humphreys, Microstructural characterization of InGaN/GaN multiple quantum wells with high indium composition, Journal of Crystal Growth, 231 (2001) 466-473.
[37] T. Tanikawa, K. Ohnishi, M. Kanoh, T. Mukai, T. Matsuoka, Three-dimensional imaging of threading dislocations in GaN crystals using two-photon excitation photoluminescence, Applied Physics Express, 11 (2018).
[38] R. Chierchia, T. Bottcher, H. Heinke, S. Einfeldt, S. Figge, D. Hommel, Microstructure of heteroepitaxial GaN revealed by x-ray diffraction, Journal of Applied Physics, 93 (2003) 8918-8925.
[39] F.C.P. Massabuau, S.L. Sahonta, L. Trinh-Xuan, S. Rhode, T.J. Puchtler, M.J. Kappers, C.J. Humphreys, R.A. Oliver, Morphological, structural, and emission characterization of trench defects in InGaN/GaN quantum well structures, Applied Physics Letters, 101 (2012).
[40] M. Shiojiri, C.C. Chuo, J.T. Hsu, J.R. Yang, H. Saijo, Structure and formation mechanism of V defects in multiple InGaN/GaN quantum well layers, Journal of Applied Physics, 99 (2006).
[41] T. Sugahara, M. Hao, T. Wang, D. Nakagawa, Y. Naoi, K. Nishino, S. Sakai, Role of dislocation in InGaN phase separation, Japanese Journal of Applied Physics Part 2-Letters, 37 (1998) L1195-L1198.
[42] H.P. Lei, J. Chen, P. Ruterana, Role of c-screw dislocations on indium segregation in InGaN and InAlN alloys, Applied Physics Letters, 96 (2010).
[43] H.K. Cho, J.Y. Lee, G.M. Yang, C.S. Kim, Formation mechanism of V defects in the InGaN/GaN multiple quantum wells grown on GaN layers with low threading dislocation density, Applied Physics Letters, 79 (2001) 215-217.
[44] J. Smalc-Koziorowska, E. Grzanka, R. Czernecki, D. Schiavon, M. Leszczynski, Elimination of trench defects and V-pits from InGaN/GaN structures, Applied Physics Letters, 106 (2015).
[45] S.Y. Karpov, R.A. Talalaev, I.Y. Evstratov, Y.N. Makarov, Indium Segregation Kinetics in MOVPE of InGaN-Based Heterostructures, physica status solidi (a), 192 (2002) 417-423.
[46] W. Bi, H. Kuo, P. Ku, B. Shen, Handbook of GaN Semiconductor Materials and Devices, CRC Press (2017).
[47] C.L. Tsai, Effects of underlying InGaN/GaN superlattice structures on the structural and optical properties of InGaN LEDs, Journal of Luminescence, 174 (2016) 36-41.

[48] C.Y. Jia, T.J. Yu, H.M. Lu, C.T. Zhong, Y.J. Sun, Y.Z. Tong, G.Y. Zhang, Performance improvement of GaN-based LEDs with step stage InGaN/GaN strain relief layers in GaN-based blue LEDs, Optics Express, 21 (2013) 8444-8449.
[49] A. Dussaigne, B. Damilano, N. Grandjean, J. Massies, In surface segregation in InGaN/GaN quantum wells, Journal of Crystal Growth, 251 (2003) 471-475.
[50] M. Auf der Maur, A. Pecchia, G. Penazzi, W. Rodrigues, A. Di Carlo, Efficiency Drop in Green InGaN/GaN Light Emitting Diodes: The Role of Random Alloy Fluctuations, Physical Review Letters, 116 (2016) 027401.
[51] Y. Wang, X.J. Pei, Z.G. Xing, L.W. Guo, H.Q. Jia, H. Chen, J.M. Zhou, Effects of barrier growth temperature ramp-up time on the photoluminescence of InGaN/GaN quantum wells, Journal of Applied Physics, 101 (2007).
[52] R.A. Oliver, F.C.P. Massabuau, M.J. Kappers, W.A. Phillips, E.J. Thrush, C.C. Tartan, W.E. Blenkhorn, T.J. Badcock, P. Dawson, M.A. Hopkins, D.W.E. Allsopp, C.J. Humphreys, The impact of gross well width fluctuations on the efficiency of GaN-based light emitting diodes, Applied Physics Letters, 103 (2013).
[53] A.F. Tsatsulnikov, W.V. Lundin, A.V. Sakharov, A.E. Nikolaev, E.E. Zavarin, S.O. Usov, M.A. Yagovkina, M.J. Hytch, M. Korytov, N. Cherkashin, Formation of Three-Dimensional Islands in the Active Region of InGaN Based Light Emitting Diodes Using a Growth Interruption Approach, Science of Advanced Materials, 7 (2015) 1629-1635.
[54] W.V. Lundin, A.E. Nikolaev, A.V. Sakharov, M.A. Yagovkina, A.F. Tsatsulnikov, Properties of InGaN/GaN heterostructures obtained using growth interruption under various conditions, Technical Physics Letters, 40 (2014) 365-368.
[55] Y. Sun, Y.-H. Cho, H.M. Kim, T.W. Kang, S.Y. Kwon, E. Yoon, Effect of growth interruption on optical properties of In-rich InGaN/GaN single quantum well structures, Journal of Applied Physics, 100 (2006) 043520.
[56] A. Kadys, T. Malinauskas, T. Grinys, M. Dmukauskas, J. Mickevicius, J. Aleknavicius, R. Tomasiunas, A. Selskis, R. Kondrotas, S. Stanionyte, H. Lugauer, M. Strassburg, Growth of InN and In-Rich InGaN Layers on GaN Templates by Pulsed Metalorganic Chemical Vapor Deposition, Journal of Electronic Materials, 44 (2015) 188-193.
[57] J. Song, S.-P. Chang, C. Zhang, T.-C. Hsu, J. Han, Significantly Improved Luminescence Properties of Nitrogen-Polar (0001 □) InGaN Multiple Quantum Wells Grown by Pulsed Metalorganic Chemical Vapor Deposition, ACS Applied Materials & Interfaces, 7 (2015) 273-278.
[58] M. Moseley, B. Gunning, J. Greenlee, J. Lowder, G. Namkoong, W.A. Doolittle, Observation and control of the surface kinetics of InGaN for the elimination of phase separation, Journal of Applied Physics, 112 (2012) 014909.
[59] K. Nomeika, M. Dmukauskas, R. Aleksiejunas, P. Scajev, S. Miasojedovas, A. Kadys, S. Nargelas, K. Jarasiunas, Enhancement of quantum efficiency in InGaN quantum wells by using superlattice interlayers and pulsed growth Lithuanian Journal of Physics, 55 (2015) 255-263.
[60] W.C. Lai, C.H. Yen, S.J. Chang, GaN-Based Green-Light-Emitting Diodes with InN/GaN Growth-Switched InGaN Wells, Applied Physics Express, 6 (2013).

[61] U. Rossow, L. Hoffmann, H. Bremers, E.R. Buss, F. Ketzer, T. Langer, A. Hangleiter, T. Mehrtens, M. Schowalter, A. Rosenauer, Indium incorporation processes investigated by pulsed and continuous growth of ultrathin InGaN quantum wells, Journal of Crystal Growth, 414 (2015) 49-55.
[62] H.M. Manasevit, The use of metalorganics in the preparation of semiconductor materials: Growth on insulating substrates, Journal of Crystal Growth, 13-14 (1972) 306-314.
[63] G. Stringfellow, Organometallic Vapor-Phase Epitaxy: Theory and Practice 2 ed, Academic Press (1999).
[64] R.D. Dupuis, P.D. Dapkus, Continuous room-temperature operation of $Ga_{(1-x)}Al_xAs$-GaAs double-heterostructure lasers grown by metalorganic chemical vapor deposition, Applied Physics Letters, 32 (1978) 406-407.
[65] R.R. Saxena, V. Aebi, C.B.C. III, M.J. Ludowise, H.A.V. Plas, B.R. Cairns, T.J. Maloney, P.G. Borden, P.E. Gregory, High-efficiency AlGaAs/GaAs concentrator solar cells by organometallic vapor phase epitaxy, Journal of Applied Physics, 51 (1980) 4501-4503.
[66] R.R. Bradley, MOCVD growth and characterisation of GaAlAs/GaAs double heterostructures for opto-electronic devices, Journal of Crystal Growth, 55 (1981) 223-228.
[67] H. Amano, M. Kito, K. Hiramatsu, I. Akasaki, P-Type Conduction in Mg-Doped GaN Treated with Low-Energy Electron Beam Irradiation (LEEBI), Japanese Journal of Applied Physics, 28 (1989) L2112-L2114.
[68] S. Nakamura, GaN growth using GaN buffer layer, Japanese Journal of Applied Physics Part 2-Letters & Express Letters, 30 (1991) L1705-L1707.
[69] T. Webb, 3x2FT System, System Manual, Edition 06/2009 rev 1.6, AIXTRON Ltd, (2009).
[70] K.P. Killeen, W.G. Breiland, in-situ spectral reflectance monitoring of III-V epitaxy, Journal of Electronic Materials, 23 (1994) 179-183.
[71] T. Nishinaga, Handbook of Crystal Growth, Thin Films and Epitaxy: Basic Techniques, Elsevier (2015).
[72] M.A. Moram, M.E. Vickers, X-ray diffraction of III-nitrides, Reports on Progress in Physics, 72 (2009).
[73] Y. Waseda, E. Matsubara, K. Shinoda, X-Ray Diffraction Crystallography, Springer-Verlag, Berlin Heidelberg, (2011).
[74] B.B. He, Two-dimensional X-ray Diffraction, Second Edition, John Wiley & Sons, Inc., (2018).
[75] L. Reimer, H. Kohl, Transmission Electron Microscopy, Springer-Verlag New York, (2008).
[76] FEI Tecnai G2 F20 X-TWIN data sheet, (2004).
[77] J. Thomas, T. Gemming, Analytical Transmission Electron Microscopy, An Introduction for Operators, Springer, Netherlands, (2014).
[78] E. Meyer, Atomic force microscopy, Progress in Surface Science, 41 (1992) 3-49.
[79] F.J. Giessibl, Advances in atomic force microscopy, Reviews of Modern Physics, 75 (2003) 949-983.
[80] M. Dmukauskas, Doped InGaN multiple quantum well growth using pulsed MOCVD technique, Vilnius University, (2015).
[81] B.V.R. Tata, B. Raj, Confocal laser scanning microscopy: Applications in material science and technology, Bulletin of Materials Science, 21 (1998).

[82] D. Dobrovolskas, Study of Carrier Dynamics in InGaN Using Spatially Resolved Photoluminescence Techniques, Vilnius University, (2013).
[83] C.L. Wang, M.C. Tsai, J.R. Gong, W.T. Liao, P.Y. Lin, K.Y. Yen, C.C. Chang, H.Y. Lin, S.K. Hwang, Influence of AlGaN/GaN superlattice inserted structure on the performance of InGaN/GaN multiple quantum well light emitting diodes, Materials Science and Engineering B-Solid State Materials for Advanced Technology, 138 (2007) 180-183.
[84] W.V. Lundin, A.E. Nikolaev, A.V. Sakharov, E.E. Zavarin, S.O. Usov, V.S. Sizov, A.L. Zakgeim, A.E. Chernyakov, A.F. Tsatsul'nikov, High-efficiency InGaN/GaN/AlGaN light-emitting diodes with short-period InGaN/GaN superlattice for 530-560 nm range, Technical Physics Letters, 36 (2010) 1066-1068.
[85] N. Niu, H.B. Wang, J.P. Liu, N.X. Liu, Y.H. Xing, J. Han, J. Deng, G.D. Shen, Enhanced luminescence of InGaN/GaN multiple quantum wells by strain reduction, Solid-State Electronics, 51 (2007) 860-864.
[86] K. Lee, C.R. Lee, J.H. Lee, T.H. Chung, M.Y. Ryu, K.U. Jeong, J.Y. Leem, J.S. Kim, Influences of Si-doped graded short-period superlattice on green InGaN/GaN light-emitting diodes, Optics Express, 24 (2016).
[87] J.W. Ju, E.S. Kang, H.S. Kim, L.W. Jang, H.K. Ahn, J.W. Jeon, I.H. Leea, J.H. Baek, Metal-organic chemical vapor deposition growth of InGaN/GaN high power green light emitting diode: Effects of InGaN well protection and electron reservoir layer, Journal of Applied Physics, 102 (2007).
[88] C. Haller, J.F. Carlin, G. Jacopin, W. Liu, D. Martin, R. Butte, N. Grandjean, GaN surface as the source of non-radiative defects in InGaN/GaN quantum wells, Applied Physics Letters, 113 (2018).
[89] C. Haller, J.F. Carlin, G. Jacopin, D. Martin, R. Butte, N. Grandjean, Burying non-radiative defects in InGaN underlayer to increase InGaN/GaN quantum well efficiency, Applied Physics Letters, 111 (2017).
[90] C. Haller, J.-F. Carlin, M. Mosca, M.D. Rossell, R. Erni, N. Grandjean, InAlN underlayer for near ultraviolet InGaN based light emitting diodes, Applied Physics Express, 12 (2019) 034002.
[91] K. Lee, C.-R. Lee, J.H. Lee, T.-H. Chung, M.-Y. Ryu, K.-U. Jeong, J.-Y. Leem, J.S. Kim, Influences of Si-doped graded short-period superlattice on green InGaN/GaN light-emitting diodes, Optics Express, 24 (2016).
[92] P.A. Grudowski, C.J. Eiting, J. Park, B.S. Shelton, D.J.H. Lambert, R.D. Dupuis, Properties of InGaN quantum-well heterostructures grown on sapphire by metalorganic chemical vapor deposition, Applied Physics Letters, 71 (1997) 1537-1539.
[93] S.-N. Lee, J. Kim, K.-K. Kim, H. Kim, H.-K. Kim, Thermal stability of Si-doped InGaN multiple-quantum wells for high efficiency light emitting diodes, Journal of Applied Physics, 108 (2010) 102813.
[94] D.-B. Li, Y.-H. Liu, T. Katsuno, K. Nakao, K. Nakamura, M. Aoki, H. Miyake, K. Hiramatsu, Enhanced emission efficiency of InGaN films with Si doping, physica status solidi c, 3 (2006) 1944-1948.
[95] A. Munkholm, G.B. Stephenson, J.A. Eastman, O. Auciello, M.V.R. Murty, C. Thompson, P. Fini, J.S. Speck, S.P. DenBaars, In situ studies of the effect of silicon on GaN growth modes, Journal of Crystal Growth,221 (2000).
[96] Z. Lin, R. Hao, G. Li, S. Zhang, Effect of Si doping in barriers of InGaN/GaN multiple quantum wells on the performance of green light-emitting diodes, Japanese Journal of Applied Physics, 54 (2015) 022102.

[97] Y.-L. Li, W.-C. Lai, Y.-C. Chang, Excess carrier dynamics of InGaN/GaN multiple-quantum-well light-emitting diodes with various silicon barrier doping profiles, Applied Physics Letters, 92 (2008) 152109.
[98] I. Vurgaftman, J.R. Meyer, Band parameters for nitrogen-containing semiconductors, Journal of Applied Physics, 94 (2003) 3675-3696.
[99] Y.H. Kim, C.S. Kim, S.K. Noh, S.I. Ban, S.G. Kim, K.Y. Lim, B.S. O, Structural characterization of InGaN/GaN multi-quantum well structures using high-resolution XRD, Journal of the Korean Physical Society,42 (2003).
[100] X. Guo, H. Wang, D.S. Jiang, Y.T. Wang, D.G. Zhao, J.J. Zhu, Z.S. Liu, S.M. Zhang, H. Yang, Evaluation of both composition and strain distributions in InGaN epitaxial film using x-ray diffraction techniques, Chinese Physics B, 19 (2010).
[101] W.C. Tsai, C.H. Hsu, S.F. Fu, F.W. Lee, C.Y. Chen, W.C. Chou, W.K. Chen, W.H. Chang, Optical properties associated with strain relaxations in thick InGaN epitaxial films, Optics Express, 22 (2014) A416-A424.
[102] G.X. Ju, S. Fuchi, M. Tabuchi, Y. Takeda, In situ X-ray Reflectivity Measurements on Annealed InxGa1-xN Epilayer Grown by Metalorganic Vapor Phase Epitaxy, Japanese Journal of Applied Physics, 52 (2013).
[103] G.X. Ju, Y. Honda, M. Tabuchi, Y. Takeda, H. Amano, In situ X-ray investigation of changing barrier growth temperatures on InGaN single quantum wells in metal-organic vapor phase epitaxy, Journal of Applied Physics, 115 (2014).
[104] S. Choi, T.H. Kim, S. Wolter, A. Brown, H.O. Everitt, M. Losurdo, G. Bruno, Indium adlayer kinetics on the gallium nitride (0001) surface: Monitoring indium segregation and precursor-mediated adsorption, Physical Review B, 77 (2008).
[105] J. Neugebauer, Surfactants and antisurfactants on group-III-nitride surfaces, physica status solidi (c), 0 (2003) 1651-1667.
[106] A. Chakraborty, A. Bag, P. Mukhopadhyay, S. Ghosh, D. Biswas, Elimination of V-shaped pits in InGaN/GaN/AlN/GaN heterostructure by metal modulation growth technique, Semiconductor Science and Technology, 33 (2018).
[107] F. Chen, A.N. Cartwright, P.M. Sweeney, M.C. Cheung, Influence of growth temperature on emission efficiency of InGaN/GaN multiple quantum wells, in: J.E. Northrup, J. Neugebauer, D.C. Look, S.F. Chichibu, H. Riechert (Eds.) Gan and Related Alloys-2001,(2002).
[108] K. Nomeika, Novel ways of improving quantum efficiency of InGaN LED active layers by controlling carrier diffusivity, Vilnius University, (2019).
[109] K.S. Ramaiah, Y.K. Su, S.J. Chang, B. Kerr, H.P. Liu, I.G. Chen, Characterization of InGaN/GaN multi-quantum-well blue-light-emitting diodes grown by metal organic chemical vapor deposition, Applied Physics Letters, 84 (2004) 3307-3309.
[110] T.Y. Lin, J.C. Fan, Y.F. Chen, Effects of alloy potential fluctuations in InGaN epitaxial films, Semiconductor Science and Technology, 14 (1999).
[111] A. Mohanta, S.F. Wang, T.F. Young, P.H. Yeh, D.C. Ling, M.E. Lee, D.J. Jang, Observation of weak carrier localization in green emitting InGaN/GaN multi-quantum well structure, Journal of Applied Physics, 117 (2015).
[112] I. Vurgaftman, J.R. Meyer, L.R. Ram-Mohan, Band parameters for III-V compound semiconductors and their alloys, Journal of Applied Physics, 89 (2001) 5815-5875.

[113] J. Wu, W. Walukiewicz, W. Shan, K.M. Yu, J.W. Ager, S.X. Li, E.E. Haller, H. Lu, W.J. Schaff, Temperature dependence of the fundamental band gap of InN, Journal of Applied Physics, 94 (2003) 4457-4460.
[114] T. Tao, T. Zhi, B. Liu, Y. Li, Z. Zhuang, Z.L. Xie, D.J. Chen, P. Chen, R. Zhang, Y.D. Zheng, Spatially localised luminescence emission properties induced by formation of ring-shaped quasi-potential trap around V-pits in InGaN epi-layers, Physica Status Solidi a-Applications and Materials Science, 211 (2014) 2823-2827.
[115] N. Okada, H. Kashihara, K. Sugimoto, Y. Yamada, K. Tadatomo, Controlling potential barrier height by changing V-shaped pit size and the effect on optical and electrical properties for InGaN/GaN based light-emitting diodes, Journal of Applied Physics, 117 (2015).
[116] K. Kazlauskas, G. Tamulaitis, P. Pobedinskas, A. Zukauskas, M. Springis, C.F. Huang, Y.C. Cheng, C.C. Yang, Exciton hopping in $In_xGa_{1-x}N$ multiple quantum wells, Physical Review B, 71 (2005).
[117] K. Gelzinyte, R. Ivanov, S. Marcinkevicius, Y. Zhao, D.L. Becerra, S. Nakamura, S.P. DenBaars, J.S. Speck, High spatial uniformity of photoluminescence spectra in semipolar (2021) plane InGaN/GaN quantum wells, Journal of Applied Physics, 117 (2015).
[118] J. Lee Rodgers, W.A. Nicewander, Thirteen Ways to Look at the Correlation Coefficient, The American Statistician, 42 (1988) 59-66.
[119] J. Mickevicius, D. Dobrovolskas, J. Aleknavicius, T. Grinys, A. Kadys, G. Tamulaitis, Spatial redistribution of photoexcited carriers in InGaN/GaN structures emitting in a wide spectral range, Journal of Luminescence, 199 (2018) 379-383.
[120] A. Kadir, K. Bellmann, T. Simoneit, M. Pristovsek, M. Kneissl, Influence of group III and group V partial pressures on the size and density of InGaN quantum dots in MOVPE, Physica Status Solidi a-Applications and Materials Science, 209 (2012) 2487-2491.
[121] I.E. Titkov, S.Y. Karpov, A. Yadav, V.L. Zerova, M. Zulonas, B. Galler, M. Strassburg, I. Pietzonka, H. Lugauer, E.U. Rafailov, Temperature-Dependent Internal Quantum Efficiency of Blue High-Brightness Light-Emitting Diodes, IEEE Journal of Quantum Electronics, 50 (2014) 911-920.

Peer reviewed publications and reprints

[PMD1] K. Nomeika, **M. Dmukauskas**, R. Aleksiejūnas, P. Ščajev, S. Miasojedovas, A. Kadys, S. Nargelas, K. Jarašiūnas, Enhancement of quantum efficiency in InGaN quantum wells by using superlattice interlayers and pulsed growth, Lithuanian Journal of Physics, 55 (2015) 255-263.

[PMD2] **M. Dmukauskas**, A. Kadys, T. Malinauskas, T. Grinys, I. Reklaitis, K. Badokas, M. Skapas, R. Tomašiūnas, D. Dobrovolskas, S. Stanionytė, I. Pietzonka, M. Strassburg, H.J. Lugauer, Influence of metalorganic precursors flow interruption timing on green InGaN multiple quantum wells, Journal of Physics D-Applied Physics, 49 (2016).

[PMD3] **M. Dmukauskas**, J. Mickevičius, D. Dobrovolskas, A. Kadys, S. Nargelas, G. Tamulaitis, Correlation between growth interruption and indium segregation in InGaN MQWs, Journal of Luminescence, 221, (2020).

Paper I

Enhancement of quantum efficiency in InGaN quantum wells by using superlattice interlayers and pulsed growth

K. Nomeika, M. Dmukauskas, R. Aleksiejūnas, P. Ščajev, S. Miasojedovas, A. Kadys, S. Nargelas, K. Jarašiūnas

Lithuanian Journal of Physics, 55 (2015) 255-263.
DOI: 10.3952/physics.v55i4.3221

Lithuanian Journal of Physics, Vol. **55**, No. 4, pp. 255–263 (2015)

ENHANCEMENT OF QUANTUM EFFICIENCY IN InGaN QUANTUM WELLS BY USING SUPERLATTICE INTERLAYERS AND PULSED GROWTH

K. Nomeika, M. Dmukauskas, R. Aleksiejūnas, P. Ščajev, S. Miasojedovas, A. Kadys,

S. Nargelas, and K. Jarašiūnas

Institute of Applied Research, Vilnius University, Saulėtekio 9, LT-10222 Vilnius, Lithuania

E-mail: kazimieras.nomeika@tmi.vu.lt

Received 22 June 2015; revised 21 July 2015; accepted 29 September 2015

Enhancement of internal quantum efficiency (IQE) in InGaN quantum wells by insertion of a superlattice interlayer and applying the pulsed growth regime is investigated by a set of time-resolved optical techniques. A threefold IQE increase was achieved in the structure with the superlattice. It was ascribed to the net effect of decreased internal electrical field due to lower strain and altered carrier localization conditions. Pulsed MOCVD growth also resulted in twice higher IQE, presumably due to better control of defects in the structure. An LED (light emitting diode) structure with a top *p*-type contact GaN layer was manufactured by using both growth techniques with the peak IQE equal to that in the underlying quantum well structure. The linear recombination coefficient was found to gradually increase with excitation due to carrier delocalization, and the latter dependence was successfully used to fit the IQE droop.

Keywords: light emitting diodes, nitride semiconductors, photoluminescence, carrier recombination, carrier diffusion

PACS: 73.21.Fg, 78.67.-n, 78.47.-p

1. Introduction

GaN-based structures for light emitting diodes (LEDs) and other optoelectronic devices are grown predominantly on sapphire substrates by the MOCVD technique, because GaN substrates for homoepitaxial growth remain to be expensive and difficult to obtain. A large mismatch of the lattice constants and the thermal expansion coefficients between GaN and sapphire result in considerable strain, which in turn gives rise to a large amount of dislocations and an internal piezoelectric field. The high internal electric field quenches the internal quantum efficiency (IQE) in GaN-based quantum structures due to the quantum confined Stark effect. Therefore, several technological modifications of the LED structure have been developed to relieve the strain in the material. Most of these approaches involve inserting a buffer layer between the sapphire wafer and LED active structure, like a low-temperature GaN layer [1], AlN or AlGaN layer [2], SiO_2 layer with openings for overgrowth [3], or a short period superlattice (SL) [4]. It has been demonstrated that the SL insertion layer results in increase of IQE [5, 6] and smaller photoluminescence (PL) peak shift with injection [4] due to supposedly smaller defect density and lower internal electrical fields. SL was also used to improve the electroluminescence due to better hole injection and current spreading [7–9].

On the other hand, IQE depends on structural quality of InGaN quantum wells that determine the amount of defects and, consequently, nonradiative recombination time. It is well known that IQE drops as the In content is increased, mostly due to lower growth temperatures needed to achieve larger In amount in the layers. A promising technique for achieving metal rich InGaN layers of good quality is a pulsed growth. This technique was mainly used for InN growth, but it has also been demonstrated as a promising tool for InGaN growth by metal-modulated epitaxy [10], high-pressure MOCVD [11, 12], and recently by low pressure MOCVD [13].

In this paper, we analyze the effects of SL insertion and the pulsed growth on IQE by monitoring carrier dynamics in the InGaN quantum well (QW) structures

emitting at 450–460 nm. Optical properties and carrier dynamics features are compared between (i) QW structures with and without an SL interlayer and (ii) identical QW samples grown by continuous or pulsed growth. We employ a number of time-resolved techniques like light-induced transient gratings (LITG), differential transmission (DT), free carrier absorption (FCA), and photoluminescence (PL) to obtain a detailed picture of carrier recombination pathways. We demonstrate a three-fold increase in IQE in the structure with an SL and a two-fold one in the pulsed grown sample, as compared to that of the corresponding reference structures. We analyze the effects of changes in the internal electrical field and carrier delocalization on the IQE in the structures. We also demonstrate that a full LED structure with a p-contact layer may reach the peak IQE equal to that of the underlying MQW structure.

2. Samples and measurement techniques

Two sets of MQWs structures under investigation were grown by MOCVD on (0001) sapphire with a ~3 μm thick GaN template. Ammonia (NH_3), trimethylgallium (TMG), trimethylindium (TMI), trimethylaluminum (TMA), silane, and magnesium bispentacyclodienyl (Cp_2Mg) were used as source compounds, nitrogen and hydrogen were used as carrier gases.

In the first set of MQWs samples (samples *A* and *B*) we investigated an impact of InGaN/GaN SL as a crystal grating stress modified interlayer between the GaN template and MQWs. The SL growth parameters in sample *A* were optimized: the SL structure consists of 8 periods of $In_{0.06}Ga_{0.94}N$/GaN heterostructures with a total thickness of 30–35 nm. The active regions of the structures contained five (3–4) nm wide $In_{0.1}Ga_{0.9}N$ QWs separated by 6 nm wide GaN quantum barriers. The whole structure is capped by a 30 nm thick GaN layer. Sample *B* was grown under identical conditions, but without SL.

In the second set of 3 samples (samples *1*, *2*, *3*) we analyzed impact of the pulsed growth on QW and full LED quantum efficiency. All samples were grown on a 3 μm thick GaN template on sapphire together with an optimized SL interlayer which has been described above. The active part consisted of 5 periods $In_{0.1}Ga_{0.9}N$/GaN multiple QW structure 3–4 nm thick wells and 6 nm thick barriers. A reference InGaN/GaN MQW structure (sample *1*) was grown in a conventional precursor continuous-flux mode. In the pulsed growth mode, NH_3 was constantly flowing, while TMI and TMG were sent into a chamber for 15 s, and then bypassed for 5 s (sample *2*). More details of the pulsed growth MOCVD can be found in Ref. [14]. Finally, a full LED structure with a top 40 nm thick *p*-type $Al_{0.1}Ga_{0.9}N$ blocking layer and a 300 nm thick *p*-type GaN layer was grown (sample *3*).

The experimental set-up for the time-resolved DT consisted of a PHAROS (*Light Conversion*) laser, delivering 1030 nm and 200 fs duration pulses at the 30 kHz repetition rate and an ORPHEUS (*Light Conversion*) optical parametric amplifier (OPA), generating wavelengths in the 630–2600 nm range. Frequency doubling of OPA pulses was used to set the wavelength of one of the split beams from the laser for the selective excitation (382 nm, 3.25 eV) of the QWs in the samples while the other delayed beam was passed through a sapphire crystal to generate a white light continuum probe. A spectrograph with the 300 lines/mm grating and a CCD camera spectrometer provided means to observe the evolution of DT spectra in a 380–480 nm window. A chopper was used to periodically close the pump pulse and measure the DT with and without excitation ($T_p(\lambda, t)$ and $T_0(\lambda)$, respectively) at various probe delays, providing the instantaneous $T(\lambda, t)$ spectra (in mOD units): $T(\lambda, t) = 1000 \times \log(T_0(\lambda)/T_p(\lambda, t))$.

FCA and PL IQE measurements were carried out using the same laser system as in DT. In FCA, the second OPA was used for a probe beam. The probe was tuned to 1.65 μm (0.75 eV). An integrating sphere with the three-measurement approach was used for the evaluation of PL IQE [15]. In the three-measurement approach 3 PL spectra are taken: one with an empty sphere, one with the sample in the sphere but out of the path of the pump beam and one with the sample in the sphere and in the path of the pump beam. For both experiments, the pump was 390 nm (3.18 eV).

The YAG:Nd^{3+} laser with 25 ps pulse duration and 10 Hz repetition rate was combined with a *Hamamatsu* C10627 streak camera and an *Acton* SP2300 monochromator for TRPL measurements, providing a temporal resolution of 20 ps. With the water Raman-shift of the third laser harmonic (355 nm) the wavelength of the pump beam was 405 nm (3.06 eV).

For the LITG experiment, the same YAG:Nd^{3+} laser with the water Raman-shifted pump to 405 nm was used. The principle of the technique is the excitation of the sample by an interference field of two coherent pump beams, creating a transient spatially modulated free carrier pattern $N(x) = N_0 + \Delta N[1 + \cos(2\pi x/\Lambda)]$ with spacing Λ, which modulates the refractive index $\Delta n(x) \propto \Delta N(x)$ and diffracts a delayed probe beam (1064 nm – 1.17 eV, fundamental laser harmonic). Diffraction efficiency of a transient grating $\eta(t) \propto (\Delta N d)^2$ and its decay $1/\tau_g = 1/\tau_R + 1/\tau_D$ provided a convenient way to determine the recombination-governed

grating decay time τ_R and the diffusive decay time $\tau_D = \Lambda^2/(4\pi^2 D_a)$. The latter is Λ dependent, therefore the bipolar diffusion coefficient D_a was determined by performing measurements with different induced grating periods at various photoexcited carrier densities.

The reflectivity of the samples was 0.3 for the FCA experiment (because of the Brewster's angle of the sample in respect of the pump beam) and 0.2 for other techniques. For the calculations of photoexcited carrier densities the absorption coefficient $\alpha = 10^5$ cm^{-1} was taken, which resulted in 1.35×10^{19} cm^{-3} for the 100 μJ/cm^2 excitation energy fluence.

3. Results and discussion

Figure 1(a) shows the IQE as a function of photoexcited carrier density in the samples with and without an SL layer. Both IQE curves reveal the typical features of "efficiency droop" in InGaN QWs: the IQE value increases up to carrier densities of $(1–3) \times 10^{19}$ cm^{-3} and starts to decline at higher excitations. SL insertion resulted in threefold increase of the peak IQE value (30% in sample *A* versus 10% in sample *B*) and much "flatter" IQE vs the excitation curve. We note a rather large blueshift of the PL peak position with excitation in sample *B* (170 meV), compared to the shift by 40 meV in sample *A* (Fig. 1(b)). Consequently, a full width at the half maximum (FWHM) of the PL spectrum in sample *B* became considerably broader at high excitations, while at low ones the FWHM values were similar in both structures (Fig. 1(c)). Different blueshift and emission wavelengths can be attributed to the effects of the internal electrical field. A larger blueshift with excitation indicates a stronger internal piezo electrical field in sample *B* due to larger strain, while much shorter emission wavelengths at high carrier densities point out a smaller indium amount in this structure. The reported strain relaxation due to the SL [4] and slower indium incorporation in the compressively strained QWs [16] support the latter assumption. In addition, TEM and XRD data (to be reported elsewhere) suggest that the QW growth rate is larger in more strained structures. As a result, thinner QWs with higher In content can be expected in sample *A*, which is favourable for higher IQE [17, 18] and smaller efficiency droop. The impact of

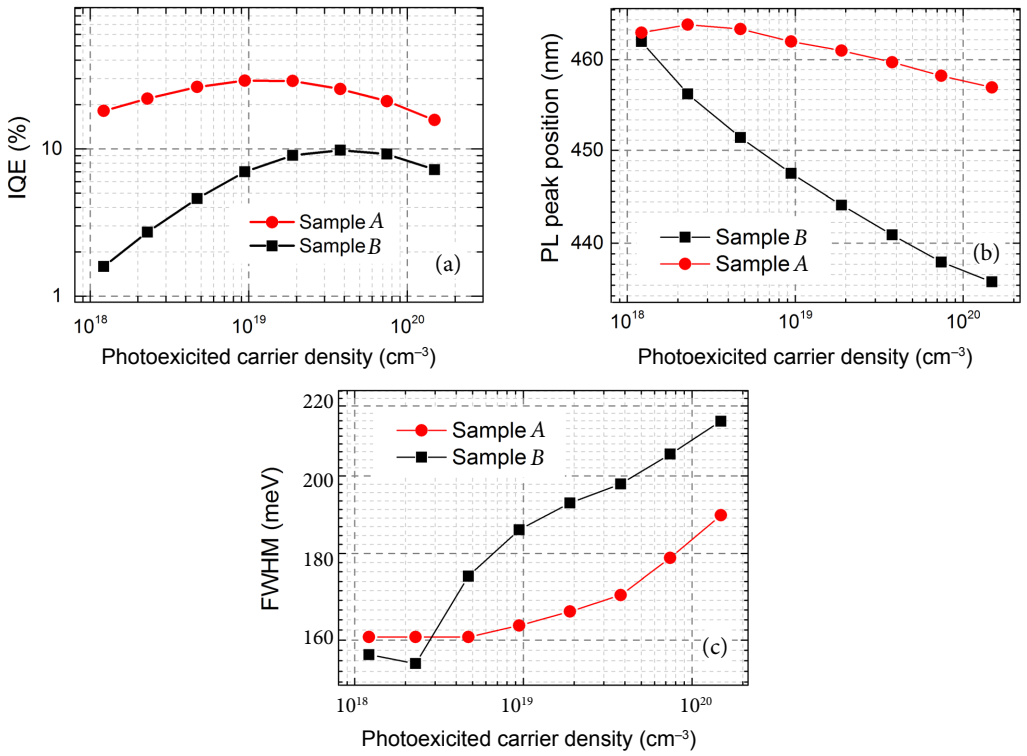

Fig. 1. Photoluminescence quantum efficiency (a), peak position of PL spectra (b), and FWHM (c) as a function of photoexcited carrier density in the structures with SL (sample *A*, red online) or without SL (sample *B*, black).

the internal electrical field, however, cannot fully account for differences in IQE, especially at high carrier densities. Also, large PL peak shift can be caused by saturation of localized states at a low energy side of the PL spectrum [19–22].

Time-resolved FCA, PL, and DT measurements were carried out for a direct observation of carrier dynamics and discrimination between the radiative and non-radiative recombination pathways. The FCA technique allowed determination of the average lifetime of the net carrier population, while DT provided complementary information on temporal changes in the occupancy of particular states. Figure 2(a) shows the FCA kinetics recorded in sample *A* for various excitation energy densities within the 30–890 μJ/cm^2 range. The peak amplitude of the transients increases linearly with the carrier density within the entire excitation range, thus confirming a linear increase of the photoexcited carrier density and the absence of absorption bleaching. A precise calibration of the carrier density N and density-dependent recombination constants of the ABC model [23] is feasible under this condition. For the sake of estimation simplicity, an instantaneous decay time at the very initial part of the kinetics (within 90–200 ps after the pump) was calculated as a function of N (Fig. 2(b)). The latter dependence revealed a close to the linear decrease of lifetime with excitation which may be attributed either to the increase of the radiative recombination rate ($1/\tau_{rad} \sim B_{rad}N$, where B_{rad} is the radiative recombination coefficient) or to the density-activated nonradiative recombination after carriers escape from the potential minima and are captured by traps [24], which can be expressed by the nonradiative recombination rate $A(N) = B_{nr}N$. If both processes take place simultaneously, only a part of the total density-dependent recombination rate can contribute to the radiative decay, i. e. $B^* = B_{rad} + B_{nr}$, in agreement with our previous observations [25, 26].

We applied the described models for the analysis of the excitation-dependent carrier lifetime. Following the standard ABC model, the constant non-radiative recombination coefficient A (or excitation-independent nonradiative lifetime $\tau_{NR} = 1/A$) and the effective recombination coefficient $B^* \sim 1/N$ can be obtained from the fitting of the decay time $\tau = (A + B^*N+CN^2)^{-1}$, where C is the Auger recombination term. The Auger term is considered as a possible mechanism of non-radiative losses; however, it should be important only at carrier densities well above 10^{19} cm^{-3} due to a small value (~10^{-31} cm^6/s) in InGaN [27]. For both samples $\tau_{NR} = 1/A \approx 35$ ns was estimated from TRPL transients at long delay times (>30 ns); this term is dominant at carrier densities below 10^{18} cm^{-3}. The values of the recombination coefficient B^* were estimated from Fig. 2(b) as 0.8×10^{-11} cm^3/s and 2.4×10^{-11} cm^3/s for samples *B* and *A*, respectively. The ratio of three between the B^* as well the IQE values agrees quite well for these samples, suggesting that competition between the radiative and nonradiative processes varies with excitation and depends on the sample structural quality. On the other hand, different IQE values may be a consequence of different density of carriers contributing to radiative recombination. We fitted the measured IQE curves with the modified AB*C model:

$$\mathrm{IQE} = \frac{B_{rad}N}{A + (B_{rad} + B_{nr})N}. \quad (1)$$

To better account for the IQE droop, saturation of B_{rad} with the excitation due to the phase-state filing was included [28]:

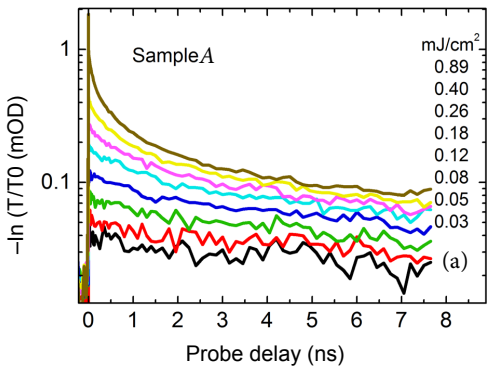

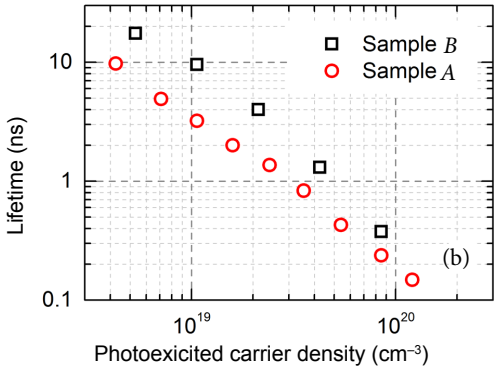

Fig. 2. (a) FCA kinetics in sample *A* at various excitations. (b) Instantaneous carrier lifetime at 100–200 ps delay as a function of photoexcited carrier density.

$$B_{\mathrm{rad}} = \frac{B_0}{1 + \dfrac{N}{N^*}}. \qquad (2)$$

Here, B_0 is the unsaturated recombination coefficient and N^* is the threshold carrier density of saturation. $B^* = B_{\mathrm{rad}} + B_{\mathrm{nr}}$ = const was also assumed since FCA measurements showed no saturation of the net B^* term. A good fit of IQE curves was obtained under these assumptions, without adding the Auger term (Fig. 3). Equation (1) allowed obtaining exact absolute IQE values, while the standard ABC with the C term of 2×10^{-31} cm^6/s yields in an overestimated IQE. Fitting parameters were as follows: $1/A$ = 26 ns, $B^* = 2.4 \times 10^{-11}$, $N^* = 9.4 \times 10^{19}$ cm^{-3}, $B_0 = 0.9 \times 10^{-11}$ cm^3/s (sample A); $1/A$ = 15 ns, $B^* = 0.8 \times 10^{-11}$, $N^* = 20 \times 10^{19}$ cm^{-3}, $B_0 = 0.11 \times 10^{-11}$ cm^3/s (sample B). Net B^* values were taken from the fit in Fig. 2(b). The analysis of Eq. (1) shows that the peak IQE value is governed by the ratio of $B_{\mathrm{rad}}/B_{\mathrm{nr}}$: this ratio is 0.6 and 0.16 in samples A and B, which correlates with the IQE peak values of 30 and 10%. The efficiency droop occurs due to the expected saturation of B_{rad} [29] and predominantly due to the increase of B_{nr} [26, 30]. The initially constant A term, being relatively small in the samples, has some impact only at lower excitations. Different values of the radiative recombination efficiency B_{rad} in the samples can be attributed to the quantum confined Stark effect: stronger electrical field results in larger separation of electron-hole wave functions and smaller radiative recombination in sample B. We note that N^* values can also be affected by the electrical field, since it is not accounted for in the simplistic model (1).

To assess the physical reasons behind the lower radiative recombination rate in sample B, we measured and compared the PL and DT spectra at various excitations and delay time instants (Fig. 4). The DT signal has a negative sign indicating the bleaching of absorption in the bandgap vicinity. A shift between the spectral positions of DT and PL spectra indicates that absorption occurs in higher energy states (presumably in the extended states of a QW), then carriers relax in low energy localized states, where radiative recombination occurs. An overlap between the DT and PL spectra pointed out to the most efficient spectral range of carrier transfer from high to low energy states. This process may influence the PL efficiency, since the PL efficiency from the high energy states is low if compared to that from the localized low energy states [31]. At the 46 μJ/cm^2 excitation (corresponding to 6.2×10^{18} cm^{-3} carrier density), the shift between PL and DT spectra is 25 and 31 nm in samples A and B, respectively. Larger separation between the absorption and PL peaks results in smaller IQE in sample B, especially at lower excess carrier densities. With increasing excitation,

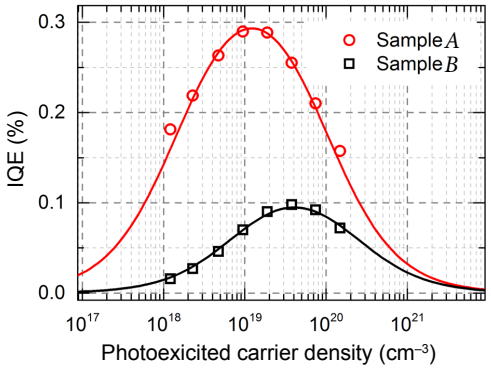

Fig. 3. Fitted IQE curves using the (1) model.

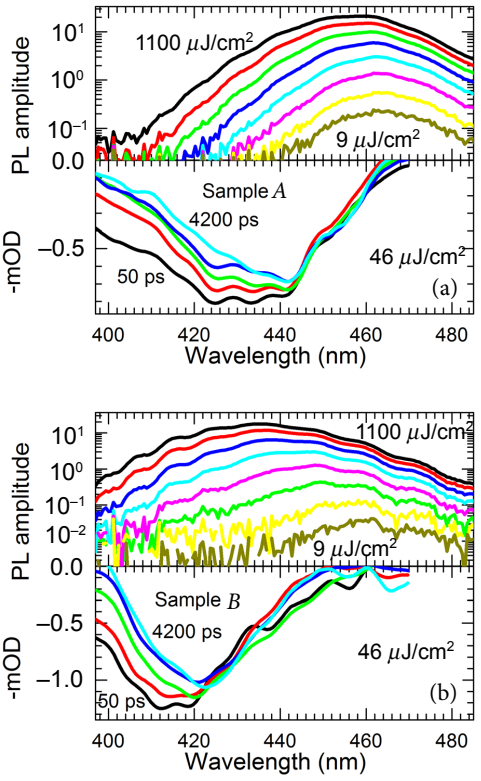

Fig. 4. Time-integrated PL spectra at various excitations (top figures, excitation range is indicated on the plot) and differential transmission (DT) spectra at various delay times (bottom figures) in samples with SL (a) and without SL (b).

the PL spectra broaden as the localized states get saturated and the fast PL transients point to emission from the higher energy. This broadening is larger in sample *B* (Fig. 1(c)), pointing out to lower density of the localized states in it with respect to sample *A*.

Stronger carrier localization in sample *A* is further evidenced by the dependence of the diffusion coefficient *D* on carrier density (Fig. 5). *D* is equal to 0.5 cm^2/s and 1 cm^2/s at carrier density of 1×10^{19} cm^{-3} in samples *A* and *B*, respectively. It increases with excitation in both samples, but the increase is more pronounced in sample *B*. LITG gives the bipolar diffusion coefficient, which under the used experimental conditions is proportional to the hole mobility [32]. We explain higher mobility of free carriers (holes) in sample *B* by a larger part of free carriers occupying the extended states in QWs, as compared to that of sample *A*. With increasing excitation, a relatively larger part of carriers is being transferred to the extended states, and this is reflected in asymmetrical broadening of DT and PL spectra towards higher energies. A similar effect has been reported previously [26]. Therefore, it can be suggested that larger increase in the *D* value is also a signature of faster non-radiative recombination and, thus, lower IQE at high excitations. Delocalization of presumably holes and subsequent increase of non-radiative recombination of carriers with increasing density is the physical origin of the term B_{nr} and a possible reason for IQE droop.

An impact of the pulsed MOCVD growth on the IQE of QW structures was investigated by performing similar measurements of IQE, time-resolved PL, DT spectra, and LITG kinetics. Here a set of 3 samples was analyzed.

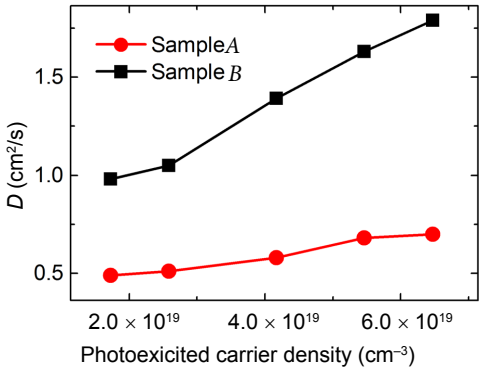

Fig. 5. Diffusion coefficient as a function of photoexcited carrier density.

Figure 6(a) shows the comparison of IQE in the samples grown under continuous or pulsed growth mode (sample *1* and sample *2*, respectively). The pulsed growth resulted in almost twofold IQE increase with respect to the reference structure. In contrast to the previous set, the peaks of the IQE curves appear at similar carrier density of ~2×10^{19} cm^{-3} in both samples. This value is close to that in sample *A*, which confirms that the droop threshold density is closely related to the structure of the sample, since the latter determines the strain, internal electrical field strength, and carrier localization. The latter is weaker in the reference structure, as evidenced by higher carrier diffusivity with respect to the pulsed growth structure (Fig. 6(b)). Moreover, even slightly weaker carrier localization and higher *D* value in the LED structure lead to its low IQE value at low excitations (sample *3*). The LED structure also exhibits larger PL blueshift with excitation (~70 meV) if compared to sample *2* (30 meV, Fig. 7). Similarly

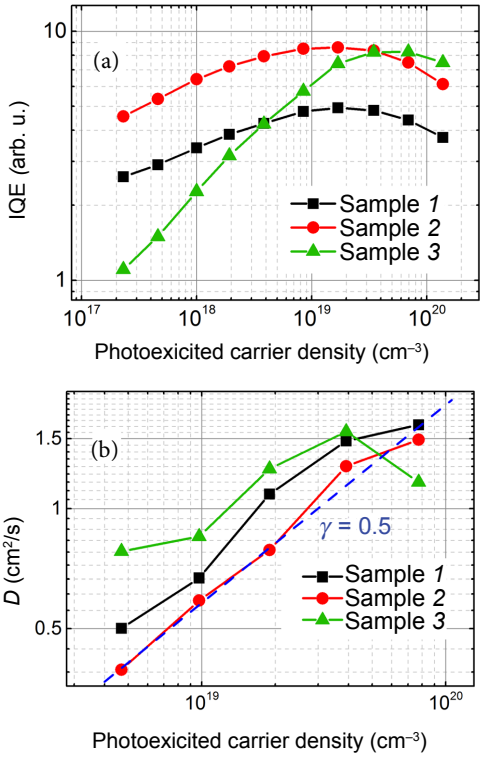

Fig. 6. IQE values (a) and diffusion coefficient (b) as a function of carrier density in the structures grown under continuous (sample *1*) or pulsed growth (sample *2*), and in the full LED structure (sample *3*).

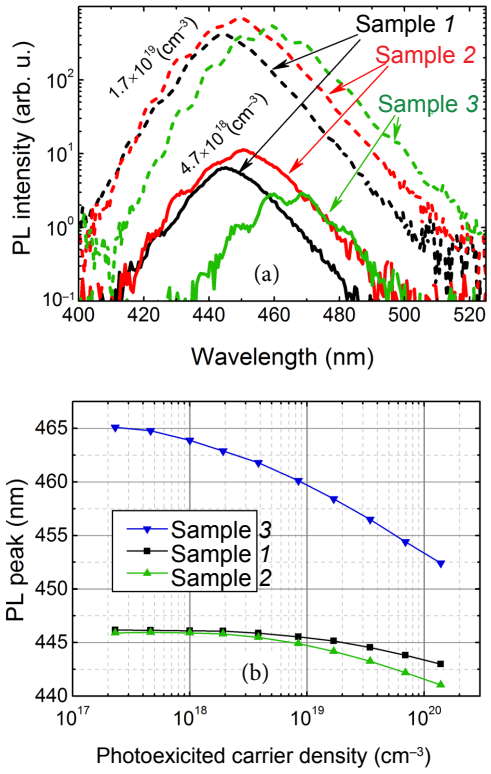

Fig. 7. PL spectra (a) and PL peak position vs carrier density (b) in samples *1*, *2* and *3*.

like in the previous set, a larger blueshift can be a mixture of larger screening effects due to stronger electric fields and saturation of localized states. Both effects, however, have a similar negative influence on IQE at low excitations and are eliminated at high carrier densities, where IQE of the LED structure reaches the same peak value as in sample *2*. The latter fact indicates a relatively low defect density and low non-radiative recombination rate A. It is evidenced by TRPL measurements: $1/A = \tau$ values are 13.5, 27, and 49 ns at 1.4×10^{18} cm^{-3} in samples *1*, *2*, and *3*, respectively. Long lifetime and high IQE at high excitations indicate that the top p-GaN layer has a negligible negative effect on LED performance, which is often the case due to diffusion of Mg dopants to the active MQW area [33].

4. Conclusions

Insertion of the superlattice interlayer and the pulsed MOCVD growth were employed and yielded three- and two-fold enhancement of IQE in InGaN/GaN QWs, respectively. A detailed investigation by time-resolved transient grating, photoluminescence, free carrier absorption, and differential transmission techniques was employed to analyze the physical origins of IQE increment and IQE droop at high carrier densities. The superlattice interlayer resulted in lower strain and smaller internal electrical field in the MQW samples. A crucial influence of carrier delocalization to IQE and its droop was evidenced by an inverse correlation between the IQE values and carrier diffusion coefficient: the increase in diffusivity resulted in the drop of IQE in all samples. A simple model based on the modified ABC rate equation with the excitation-dependent A term was used to account for increasing rate of nonradiative recombination with the excitation. The IQE droop was explained assuming the linear increase of both radiative and nonradiative recombination rates, together with the saturation of the radiative recombination coefficient due to phase-space filling. Finally, a LED structure with a *p*-type contact layer was grown with the peak IQE similar to that of the underlying MQW structure.

Acknowledgements

This work at Vilnius University was supported by the European Social Fund under Project VP1-3.1-ŠMM-07-K-02-006.

References

[1] S. Nakamura, GaN growth using GaN buffer layer, Jpn. J. Appl. Phys. **30**(10A), L1705 (1991), http://dx.doi.org/10.1143/JJAP.30.L1705

[2] H. Amano, N. Sawaki, I. Akasaki, and Y. Toyoda, Metalorganic vapor phase epitaxial growth of a high quality GaN film using an AlN buffer layer, Appl. Phys. Lett. **48**(5), 353–355 (1986), http://dx.doi.org/10.1063/1.96549

[3] A. Sakai, H. Sunakawa, and A. Usui, Defect structure in selectively grown GaN films with low threading dislocation density, Appl. Phys. Lett. **71**(5), 2259–2261 (1997), http://dx.doi.org/10.1063/1.120044

[4] S.J. Leem, Y.C. Shin, K.C. Kim, E.H. Kim, Y.M. Sung, Y. Moon, S.M. Hwang, and T.G. Kim, The effect of the low-mole InGaN structure and InGaN/GaN strained layer superlattices on optical performance of multiple quantum well active layers, J. Cryst. Growth **311**(1), 103–106 (2008), http://dx.doi.org/10.1016/j.jcrysgro.2008.10.047

[5] S.P. Chang, C.H. Wang, C.H. Chiu, J.C. Li, Y.S. Lu, Z.Y. Li, H.C. Yang, H.C. Kuo, T.C. Lu, and S.C. Wang, Characteristics of efficiency droop in GaN-based light emitting diodes with an insertion layer between the multiple quantum wells and

n-GaN layer, Appl. Phys. Lett. **97**(25), 251114 (2010), http://dx.doi.org/10.1063/1.3531957

[6] W.V. Lundin, A.E. Nikolaeva, A.V. Sakharova, E.E. Zavarina, G.A. Valkovskiy, M.A. Yagovkina, S.O. Usov, N.V. Kryzhanovskaya, V.S. Sizov, P.N. Brunkov, A.L. Zakgeim, A.E. Cherniakov, N.A. Cherkashin, M.J. Hytch, E.V. Yakovlev, D.S. Bazarevskiy, M.M. Rozhavskaya, and A.F. Tsatsulnikov, J. Cryst. Growth **315**(1), 267–271 (2011), http://dx.doi.org/10.1016/j.jcrysgro.2010.09.043

[7] T.C. Wen, S.J. Chang, C.T. Lee, W.C. Lai, and J.K. Sheu, Nitride-based LEDs with modulation-doped $Al_{0.12}Ga_{0.88}N$-GaN superlattice structures, IEEE Trans. Electron Dev. **51**(10), 1743–1746 (2004), http://dx.doi.org/10.1109/TED.2004.835985

[8] Y.J. Liu, T.Y. Tsai, C.H. Yen, L.Y. Chen, T.H. Tsai, and W.C. Liu, Characteristics of a GaN-based light-emitting diode with an inserted p-GaN/i-InGaN superlattice structure, IEEE J. Quantum Electron. **46**(4), 492–498 (2010), http://dx.doi.org/10.1109/JQE.2009.2037337

[9] T. Jeong, H.J. Park, J.W. Ju, H.S. Oh, J.H. Baek, J.S. Ha, G.H. Ryiu, and H.Y. Ryu, High efficiency InGaN blue light-emitting diode with >4 W output power at 3 A, IEEE Photon. Technol. Lett. **26**(7), 649–652 (2014), http://dx.doi.org/10.1109/LPT.2014.2301874

[10] M. Moseley, B. Gunning, J. Greenlee, J. Lowder, G. Namkoong, and W.A. Doolittle, Observation and control of the surface kinetics of InGaN for the elimination of phase separation, J. Appl. Phys. **112**(1), 014909 (2012), http://dx.doi.org/10.1063/1.4733347

[11] N. Dietz, M. Alevli, V. Woods, M. Strassburg, H. Kang, and I.T. Ferguson, The characterization of InN growth under high-pressure CVD conditions, Phys. Status Solidi B **242**(15), 2985–2994 (2005), http://dx.doi.org/10.1002/pssb.200562246

[12] V. Woods and N. Dietz, InN growth by high-pressures chemical vapor deposition: Real-time optical growth characterization, Mater. Sci. Eng. B **127**(2–3), 239–250 (2006), http://dx.doi.org/10.1016/j.mseb.2005.10.032

[13] A. Kadys, T. Malinauskas, M. Dmukauskas, I. Reklaitis, K. Nomeika, V. Gudelis, R. Aleksiejūnas, P. Ščajev, S. Nargelas, S. Miasojedovas, and K. Jarašiūnas, Photoluminescence features and carrier dynamics in InGaN heterostructures with wide staircase interlayers and differently shaped quantum wells, Lith. J. Phys. **54**(3), 187–198 (2014), http://dx.doi.org/10.3952/physics.v54i3.2959

[14] A. Kadys, T. Malinauskas, T. Grinys, M. Dmukauskas, J. Mickevičius, J. Aleknavičius, R. Tomašiūnas, A. Selskis, R. Kondrotas, S. Stanionytė, H. Lugauer, and M. Strassburg, Growth of InN and In-rich InGaN layers on GaN templates by pulsed metal-organic chemical vapor deposition, J. Electron. Mater. **44**(1), 188–193 (2015), http://dx.doi.org/10.1007/s11664-014-3494-6

[15] S. Leyre, E. Coutino-Gonzalez, J.J. Joos, J. Ryckaert, Y. Meuret, D. Poelman, P.F. Smet, G. Durinck, J. Hofkens, G. Deconinck, and P. Hanselaer, Absolute determination of photoluminescence quantum efficiency using an integrating sphere setup, Rev. Sci. Instrum. **85**(12), 123115 (2014), http://dx.doi.org/10.1063/1.4903852

[16] S. Valdueza-Felip, E. Bellet-Amalric, A. Núñez-Cascajero, Y. Wang, M.-P. Chauvat, P. Ruterana, S. Pouget, K. Lorenz, E. Alves, and E. Monroy, High In-content InGaN layers synthesized by plasma-assisted molecular-beam epitaxy: Growth conditions, strain relaxation, and In incorporation kinetics, J. Appl. Phys. **116**(23), 233504 (2014), http://dx.doi.org/10.1063/1.4903944

[17] S. Park, T. Chung, J.H. Baek, and D. Ahn, Reduction of efficiency droop in green strain-compensated InGaN/InGaN light-emitting diodes grown on InGaN substrate, Jpn. J. Appl. Phys. **54**(2), 022101 (2015), http://dx.doi.org/10.7567/JJAP.54.022101

[18] Y.L. Li, Y.R. Huang, and Y.H. Lai, Efficiency droop behaviors of InGaN/GaN multiple-quantum-well light-emitting diodes with varying quantum well thickness, App. Phys. Lett. **91**(18), 181113 (2007), http://dx.doi.org/10.1063/1.2805197

[19] G. Sun, G. Xu, Y.J. Ding, H. Zhao, G. Liu, J. Zhang, and N. Tansu, Investigation of fast and slow decays in InGaN/GaN quantum wells, Appl. Phys. Lett. **99**(8), 081104 (2011), http://dx.doi.org/10.1063/1.3627166

[20] M.J. Davies, T.J. Badcock, P. Dawson, M.J. Kappers, R.A. Oliver, and C.J. Humphreys, High excitation carrier density recombination dynamics of InGaN/GaN quantum well structures: Possible relevance to efficiency droop, Appl. Phys. Lett. **102**(2), 022106 (2013), http://dx.doi.org/10.1063/1.4781398

[21] N.I. Bochkareva, Y.T. Rebane, and Y.G. Shreter, Efficiency droop and incomplete carrier localization in InGaN/GaN quantum well light-emitting diodes, Appl. Phys. Lett. **103**(19), 191101 (2013), http://dx.doi.org/10.1063/1.4828780

[22] R. Aleksiejūnas, K. Nomeika, S. Miasojedovas, S. Nargelas, T. Malinauskas, K. Jarašiūnas, Ö. Tuna, and M. Heuken, Carrier dynamics in blue and green emitting InGaN MQWs, Phys. Status Solidi B **252**(5) 977–982 (2015), http://dx.doi.org/10.1002/pssb.201451583

[23] J. Piprek, Efficiency droop in nitride-based light-emitting diodes, Phys. Status Solidi A **207**(10), 2217–2225 (2010), http://dx.doi.org/10.1002/pssa.201026149

[24] J. Hader, J.V. Moloney, and S.W. Koch, Density-activated defect recombination as a possible explanation for the efficiency droop in GaN-based diodes, Appl. Phys. Lett. **96**(22), 221106 (2010), http://dx.doi.org/10.1063/1.3446889

[25] T. Malinauskas, A. Kadys, T. Grinys, S. Nargelas, R. Aleksiejūnas, S. Miasojedovas, J. Mickevičius, R. Tomašiūnas, K. Jarašiūnas, M. Vengris, S. Okur, V. Avrutin, X. Li, F. Zhang, Ü. Özgür, and H. Morkoç,

Impact of carrier localization, recombination, and diffusivity on excited state dynamics in InGaN/GaN quantum wells, Proc. SPIE **8262**, 82621S–1 (2012), http://dx.doi.org/10.1117/12.906488

[26] R. Aleksiejūnas, K. Gelžinytė, S. Nargelas, K. Jarašiūnas, M. Vengris, E.A. Armour, D.P. Byrnes, R.A. Arif, S.M. Lee, and G.D. Papasouliotis, Diffusion-driven and excitation-dependent recombination rate in blue InGaN/GaN quantum well structures, Appl. Phys. Lett. **104**(2), 022114 (2014), http://dx.doi.org/10.1063/1.4862026

[27] T. Sadi, P. Kivisaari, J. Oksanen, and J. Tulkki, On the correlation of the Auger generated hot electron emission and efficiency droop in III-N light-emitting diodes, Appl. Phys. Lett. **105**(9), 091106 (2014), http://dx.doi.org/10.1063/1.4894862

[28] A. David and M.J. Grundmann, Droop in InGaN light-emitting diodes: A differential carrier lifetime analysis, Appl. Phys. Lett. **96**(10), 103504 (2010), http://dx.doi.org/10.1063/1.3330870

[29] J.I. Shim, H.S. Kim, D.S. Shin, and H.Y. Yoo, An explanation of efficiency droop in InGaN-based light emitting diodes: Saturated radiative recombination rate at randomly distributed In-rich active areas, J. Korean Phys. Soc. **58**(3), 503–508 (2011), http://dx.doi.org/10.3938/jkps.58.503

[30] R. Aleksiejūnas, P. Ščajev, S. Nargelas, T. Malinauskas, A. Kadys, and K. Jarašiūnas, Impact of diffusivity to carrier recombination rate in nitride semiconductors: from bulk GaN to (In, Ga)N quantum wells, Jpn. J. Appl. Phys. **52**(8 S), 08JK01 (2013), http://dx.doi.org/10.7567/JJAP.52.08JK01

[31] F. Hitzel, G. Klewer, S. Lahmann, U. Rossow, and A. Hangleiter, Localized high-energy emissions from the vicinity of defects in high-efficiency $Ga_xIn_{1-x}N$/GaN quantum wells, Phys. Rev. B **72**, 081309(R) (2005), http://dx.doi.org/10.1103/PhysRevB.72.081309

[32] R. Aleksiejūnas, M. Sūdžius, T. Malinauskas, J. Vaitkus, K. Jarašiūnas, and S. Sakai, Determination of free carrier bipolar diffusion coefficient and surface recombination velocity of undoped GaN epilayers, Appl. Phys. Lett. **83**(6), 1157–1159 (2003), http://dx.doi.org/10.1063/1.1599036

[33] D.M. Graham, P. Dawson, Y. Zhang, P.M.F.J. Costa, M.J. Kappers, C.J. Humphreys, and E.J. Thrush, The effect of a Mg-doped GaN cap layer on the optical properties of InGaN/AlGaN multiple quantum well structures, Phys. Status Solidi B **3**(6), 2005–2008 (2006), http://dx.doi.org/10.1002/pssc.200565246

KVANTINIO NAŠUMO PAGERINIMAS InGaN KVANTINĖSE DUOBĖSE ĮTERPIANT SUPERGARDELĘ IR NAUDOJANTIS IMPULSINIU AUGINIMU

K. Nomeika, M. Dmukauskas, R. Aleksiejūnas, P. Ščajev, S. Miasojedovas, A. Kadys, S. Nargelas, K. Jarašiūnas

Vilniaus universiteto Taikomųjų mokslų institutas, Vilnius, Lietuva

Santrauka

Vidinio kvantinio našumo (VKN) pagerinimas InGaN kvantinėse duobėse dėl supergardelės įterpimo ir impulsinio auginimo pritaikymo ištirtas laikinės skyros optinių metodikų kombinacija. Supergardelės tarpsluoksnio įterpimas padidino VKN tris kartus, tai gali būti aiškinama sumažėjusiu vidiniu elektriniu lauku dėl mažesnių įtempimų ir pakeistų lokalizacijos sąlygų. Impulsinio auginimo dėka VKN padidėjo dvigubai, tikimiausiai dėl geresnės defektų kontrolės struktūrose. Šviesos diodo darinys su viršutiniu *p* tipo GaN kontaktiniu sluoksniu buvo pagamintas naudojant supergardelės tarpsluoksnį ir impulsinį auginimą, tokiu būdu gautas toks pats maksimalus VKN kaip ir darinyje be kontaktinio sluoksnio. Tiesinės rekombinacijos koeficientas augo palaipsniui nuo žadinimo intensyvumo dėl krūvininkų delokalizacijos. Pasinaudojus tokia priklausomybe, buvo sėkmingai sumodeliuotas VKN smukimas.

Paper II

Influence of metalorganic precursors flow interruption timing on green InGaN multiple quantum wells

M. Dmukauskas, A. Kadys, T. Malinauskas, T. Grinys, I. Reklaitis, K. Badokas, M. Skapas, R. Tomašiūnas, D. Dobrovolskas, S. Stanionytė, I. Pietzonka, M. Strassburg, H.J. Lugauer,

Journal of Physics D-Applied Physics, 49 (2016)
DOI:10.1088/0022-3727/49/50/505101

IOP Publishing Journal of Physics D: Applied Physics
J. Phys. D: Appl. Phys. **49** (2016) 505101 (7pp) doi:10.1088/0022-3727/49/50/505101

Influence of metalorganic precursors flow interruption timing on green InGaN multiple quantum wells

M Dmukauskas[1], A Kadys[1], T Malinauskas[1], T Grinys[1], I Reklaitis[1], K Badokas, M Skapas[1,3], R Tomašiūnas[1], D Dobrovolskas[2], S Stanionytė[3], I Pietzonka[4], M Strassburg[4], and H-J Lugauer[4]

[1] Institute of Applied Research, Vilnius University, Sauletekio 10, 10223 Vilnius, Lithuania
[2] Semiconductor Physics Department, Faculty of Physics, Vilnius University, Sauletekio 7, 10223 Vilnius, Lithuania
[3] Department of Characterization of Materials Structure, Institute of Chemistry, Centre for Physical Sciences and Technology, Sauletekio 7, 10223 Vilnius, Lithuania
[4] OSRAM Opto Semiconductors GmbH, Leibnizstr. 4, 93055 Regensburg, Germany

E-mail: arunas.kadys@ff.vu.lt

Received 8 April 2016, revised 23 September 2016
Accepted for publication 12 October 2016
Published 11 November 2016

Abstract

The paper reports on fully strained green light emitting InGaN/GaN multiple quantum wells, grown by metalorganic vapor phase epitaxy, using metal precursor multiple flow interruptions during InGaN quantum well growth. Optimization of the interruption timing (pulse $t_1 = 20$ s, pause $t_2 = 12$ s) lets us reach the integrated photoluminescence enhancement for the growth at temperature 780 ºC. The enhancement, as a function of pause duration, appeared to be pulse duration dependent: a lower enhancement can be achieved using shorter pulses with optimized relatively shorter pauses. Indium evaporation during the interruption time was interpreted as the main issue to keep the layers intact. Quantum wells revealing the highest photoluminescence enhancement were inspected for interface quality, layer thickness, growth speed, strain, surface morphology and roughness by TEM, XRD and AFM techniques, and compared with the one grown in the conventional mode.

Keywords: III–V semiconductors, MOCVD, quantum wells

(Some figures may appear in colour only in the online journal)

1. Introduction

III-nitrides semiconductor technology has undergone tremendous development and recognition. Numerous GaN-based devices, including light emitting diodes (LEDs), laser diodes, photodetectors and high power electronics, have emerged on the market. InGaN-based quantum well (QW) LEDs became important for solid state lighting [1, 2]. On the other hand, challenges like green light LEDs still remain a major problem. Compared to the blue LEDs, green or yellow ones have lower efficiency. Large lattice mismatches for the InGaN layers grown on GaN and strong piezoelectric fields, particularly inside InGaN QW polar structures, raise significant difficulties [3].

Light emission is a result of the competition between radiative and non-radiative recombination in semiconductors. High defect densities in InGaN layers, grown on GaN/sapphire templates, increase the impact of the non-radiative recombination and reduce the light emission. However, efficient luminosity, observed in highly defected InGaN QWs, is due to In-rich regions; the potential minima for localized carriers provide efficient radiative recombination channels, in spite of the surroundings with a high dislocation density [4–12]. Indium segregation in InGaN alloys [13–15] or some spinodal decomposition [16–18] are named as the origin of these potential fluctuations [6, 10–12]. For the green or yellow light emitting QWs, the situation becomes even more complicated, as

lower growth temperatures and higher In concentrations lead to more defected areas and a higher density of non-radiative recombination channels. Surprisingly, a relatively high carrier diffusion length was considered, which enhanced the accessibility of the non-radiative recombination channels in green light emitting QWs [8]. To reduce the segregation in defect-containing areas, and to increase localization in the non-defected areas in InGaN QWs, along with the optimization of the precursor flow and growth temperature, some other technological tricks have been tested. Two-temperature or temperature-bounced growth, ramping up the temperature immediately after the InGaN growth under ammonia without metal-organics (MO), led to gross well-width fluctuations and enhanced carrier localization [19–21]. By introducing different flows of hydrogen during the InGaN growth interruptions, a formation of 3D island-like structures in the active region of InGaN/GaN LEDs was demonstrated, revealing enhanced emission efficiency [22, 23]. A remarkable enhancement of emission efficiency for yellow-green LEDs using multiple interruptions, while maintaining an unchanged ammonia flow, has been shown by *Du et al* [24].

In this article, we report on the influence of the interruption timing of the metalorganics flow for the growth of green light emitting InGaN MQWs structures. A lab scale $3 \times 2''$ closed-coupled showerhead reactor provided a flexible control over the timing of multiple MO precursor flow interruption variations.

2. Experimental procedures

2.1. InGaN MQWs fabrication

In this work InGaN/GaN MQWs were grown on a GaN template (*c*-plane sapphire substrate) by low-pressure conventional and metalorganic vapor-phase epitaxy (MOVPE) using an AIXTRON $3 \times 2''$ closed-coupled showerhead reactor. Trimethylgallium (TMGa), trimethylindium (TMIn) and ammonia were used as Ga, In and N precursors, respectively. N_2 was used as the ambient and carrier gas. All samples consisted of eight period 4 nm InGaN/GaN superlattices and five InGaN QWs, separated by a several times thicker GaN barrier (QB). The superlattice was grown for all samples at the same conditions. The InGaN MQWs were grown by the pulse mode at temperature $T_{growth} = 780$ °C and, for comparison, by the conventional mode at temperatures in the range of (830 ÷ 780) °C. The pulse growth was conducted by modulating the flow of In and Ga precursors into the reactor chamber, while maintaining the flow of the ammonia constant (see figure 1) [25]. The MO precursor pulse duration t_1 varied from 20 to 5 s, the pause duration t_2—from 3 to 20 s. A summary of the growth parameters is given in table 1.

2.2. Measurement techniques

X-ray diffraction measurements (XRD, Rigaku, SmartLab) were carried out to determine the crystalline structure and composition of the InGaN QWs. Surface and structure morphology was studied by atomic force microscopy (AFM, Witec Alpha 300) and a transmission electron microscope (TEM, FEI Tecnai G2 F20 X-TWIN). Photoluminescence (PL) was investigated using a continuous wave laser diode as an excitation source (405 nm), a Princeton Instruments Acton SP2300 spectrometer and a Pixis 256 CCD camera.

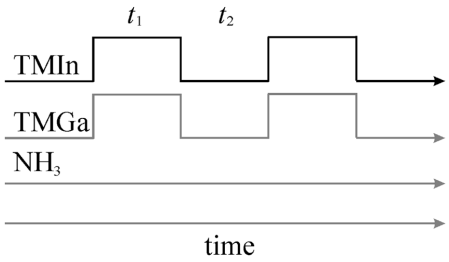

Figure 1. Timing of TMIn and TMGa precursors flow during pulse growth.

3. Results and discussion

3.1. Structural investigations

InGaN MQW sample **5,** grown in the pulsed mode featuring the best PL characteristics, was chosen for the TEM investigations. The comparison to reference sample 1 is presented in figure 2. The estimated thickness of the QW and QB pair for the reference varies in the range (1.6 ÷ 1.7) nm and (6.2 ÷ 7.9) nm, respectively. The calculated QW growth speed is 0.021 nm s^{-1}. The thickness of the QW grown in the pulsed mode (1.8 ÷ 1.9) nm is similar to the reference. The QW growth speed is 0.019 nm s^{-1} or 0.012 nm s^{-1}, if only the pulses or the pulses and pauses were considered, respectively. A slight discrepancy in the QW growth speed should be related to the MO switching conditions. In general, the speed modification for the pulsed mode will certainly depend on various growth parameters, such as temperature, pressure and pause duration. For example, the increased growth temperature and decreased pressure would enhance both the Ga and In evaporation from the InGaN, and then the increase of the pause duration would decrease the growth speed substantially.

Assuming the estimated growth speed is around 0.02 nm s^{-1}, no less than one InGaN monolayer was expected to grow during one $t_1 = 20$ s pulse. The result is based on the lattice constant *c*, which changes from 5.1850 Å (GaN) up to 5.7033 Å (InN) depending on In concentration, though a slight increase due to biaxial strain in the InGaN QWs on GaN is possible [26]. One $t_1 = 10$ s pulse would end up with less than one monolayer.

The $\omega - 2\theta$ XRD scan of the MQWs (plane (0002)) is shown in figure 3. The diffraction peaks corresponding to the GaN and InGaN/GaN MQWs are clearly expressed. Satellite peaks up to the minus fourth order are resolved and confirm the well-defined interfaces for the structure.

To evaluate the strain and indium composition in the QWs, the typical reciprocal space mapping (RSM) around the (105) reflection was measured [27]. The vertical dashed and slanted solid lines are plotted for the fully strained and fully relaxed

Table 1. Parameters of the InGaN/GaN MQWs pulse growth.

Sample No.	1 (ref)	2	3	4	5	6	7	8	9	10	11	12	13	14	15	16
t_1, s	80	20	20	20	20	20	10	10	10	10	10	5	5	5	5	5
t_2, s	0	3	6	9	12	15	3	6	9	12	15	3	6	9	12	15
p[a]	1	5	5	5	5	5	10	10	10	10	10	20	20	20	20	20

[a]amount of pulses to grow one InGaN QW layer.

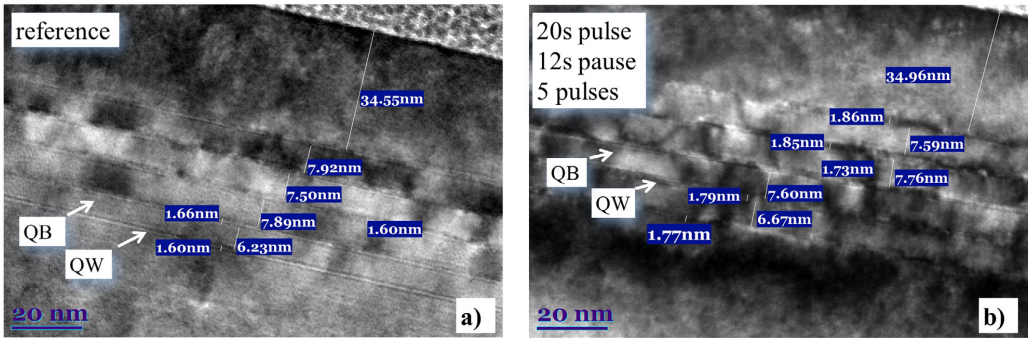

Figure 2. TEM pictures of reference sample **1** (a) and sample **5** grown by the pulse mode (b).

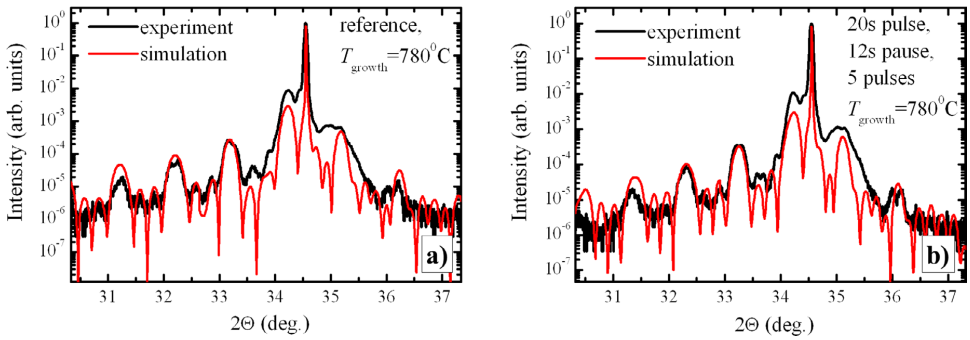

Figure 3. XRD scan of reference sample 1 (a) and sample 5 grown by the pulse mode (b).

InGaN layers, respectively (figure 4). For the reference sample, the QWs peak is shifted (dash-dotted line, figure 4(a)) along the q_x axis from the main GaN peak. It shows that the InGaN/GaN MQW structure is not coherently strained on GaN, and thus is slightly relaxed to accommodate stress caused by the InGaN layers with a larger lattice constant; a feature which has already been observed and investigated in detail [29]. The average MQW lattice constants were obtained using these equations: $a_{MQW} = \lambda/\sqrt{3}q_x$ and $c_{MQW} = 5\lambda/2q_z$, where λ is the x-ray source wavelength (0.154 06 nm), and q_x and q_z are the reciprocal lattice points of MQW 0th order peak of the (105) reflection. Lattice constants and Poisson ratios of the relaxed GaN ($c_{GaN} = 5.1850$ Å, $a_{GaN} = 3.1892$ Å, $\nu_{GaN} = 0.2$) and InN ($c_{InN} = 5.7033$ Å, $a_{InN} = 3.5378$ Å, $\nu_{InN} = 0.29$) were used to calculate In content in the QWs by applying Vegard's and Hooke's laws [28]. The QB and QW thicknesses were taken from the TEM measurements. The indium content of 27% and 20% was obtained for reference samples 1 5, respectively. The observed higher In concentration for the reference may result from the gradual strain relaxation leading to the incorporation of more In atoms into the subsequent InGaN layer [30, 31]. The reduced In concentration for the pulse growth mode probably relates to extra In evaporation during the MO flow interruption. Indium atom desorption from the growing surface of the InGaN epilayer, due to weak In–N bonds, was confirmed from the uncapped InGaN layers' different annealing investigations [32, 33]. Sample 5, grown in the pulse mode, however, showed no lattice relaxation, with the RSM peak aligned vertically (figure 4(b)). Thanks to the optimized pulse and pause durations, fully strained green InGaN QWs on GaN have been grown.

Figure 5 shows AFM images for reference samples 1 and 5 with the calculated area root-mean-square (RMS) roughness of about 3.0 and 2.2 nm, respectively. The reduced surface

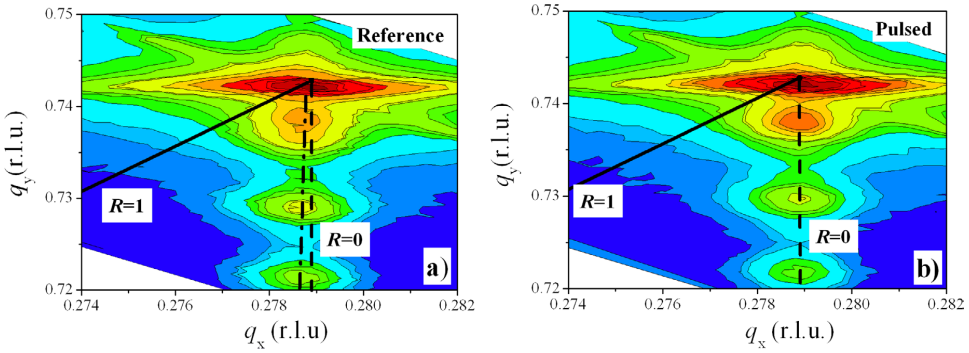

Figure 4. RSM around the (105) reflection of reference sample 1 (a) and sample 5 grown by the pulse mode (b). The dashed and solid lines passing through the GaN template reciprocal lattice points correspond to the fully strained ($R = 0$) and fully relaxed ($R = 1$) state, respectively (see the text for more explanation). The dash dotted line (a) corresponds to a partially relaxed state.

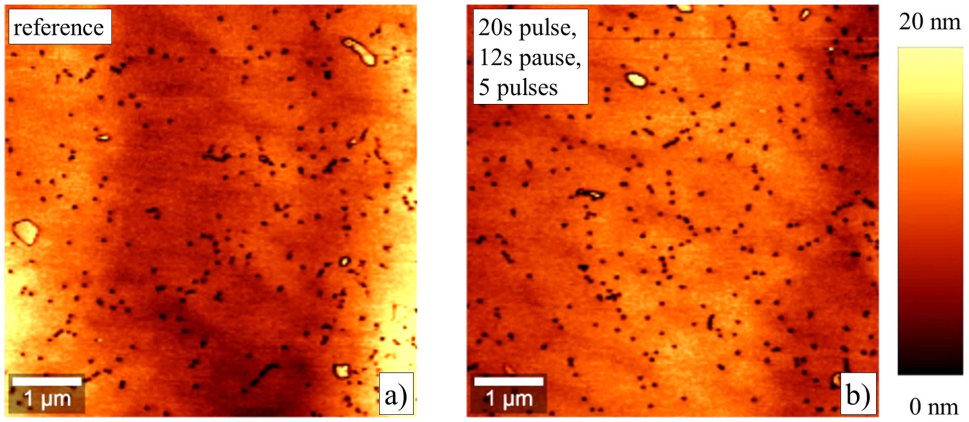

Figure 5. AFM images of reference samples 1 (a) and 5 grown by the pulse mode (b). The scan area is $6 \times 6\ \mu m^2$.

roughness for the pulsed mode is related to the enhanced surface reactant atom mobility and increased V/III ratio, due to prolonged growth time. A decreased growth speed comes into play here as predicted above. The MO flow interruption provides extra time for nitridization and migration of the In and Ga atom on the surface, suppressing any kind of metal segregation, either lateral or vertical [13, 14].

Independentof the pulse/pause duration, a high density ($(7 \div 9) \times 10^{-8}\ cm^{-2}$) of dark coloured pits regarded as *V*-shaped defects and some raised-centre trench defects of larger volume (relatively large white spots contoured in black, see figure 5) were observed. The structure of the *V*-defects include sidewall quantum wells and an open hexagonal inverted pyramid defined by six planes [34, 35]. The formation mechanism for the *V*-defects includes the growth kinetics of GaN and the segregation of In atoms in the strain field around the cores of the threading dislocations [36–38]. Indium atoms trapped and segregated in the strained field around the core of a threading dislocation play a role as a small mask, hindering Ga atoms from migrating easily to the (0001) monolayer and smoothing

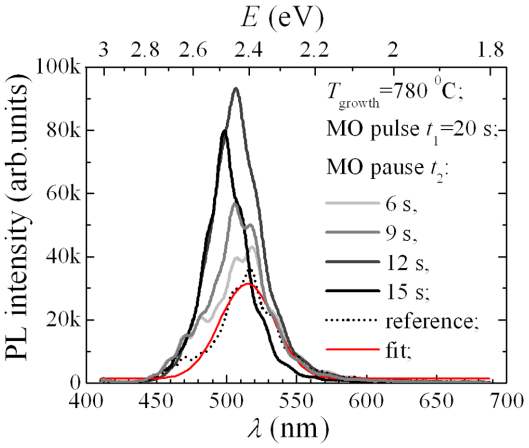

Figure 6. PL spectra of the reference 1 and the samples 3, 5 and 6 grown by the pulse mode.

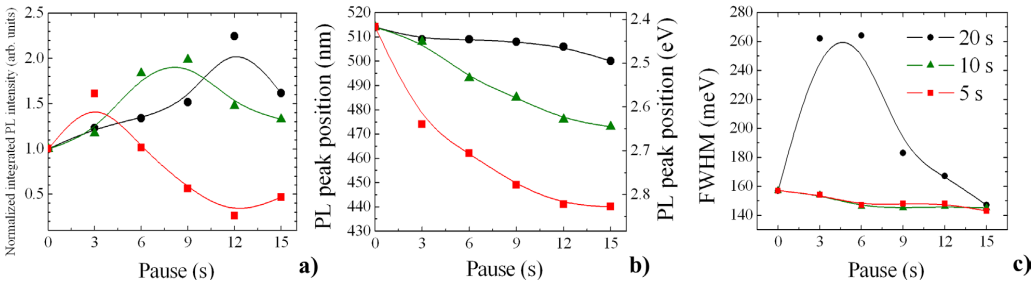

Figure 7. PL integrated signal (normalized to reference 1) (a), spectra peak position (b) and FWHM (c) as a function of the pause duration t_2 of samples grown by the pulse mode ($t_1 = 20$ s (black circles), 10 s (green triangles), 5 s (red squares)) at temperature 780 °C. The lines are guides for the eye.

the surface. From our observations, the reduction of In segregation and the enhancement of atom mobility in the course of the pulse growth is insufficient to suppress *V*-defect formation in the MQWs. It can also be seen that the pits can form trench-like aggregates as a result of coalescence [39]. A trench does not necessarily form a closed loop, where the inner region is not entirely isolated from the surrounding material [40]. All of these types of aggregates, including intersections with *V*-defects, we have observed in our work.

3.2. PL investigations

A systematic study of the PL intensity on the pause duration t_2 was carried out. A whole set of InGaN MQW samples grown at temperature 780 °C with different MO pulse durations $t_1 = 5$, 10, 20 s was investigated. The highest PL intensity was obtained for the sample grown at pulse $t_1 = 20$ s and pause $t_2 = 12$ s duration. The PL spectra presented in figure 6 revealed a rapid rise of the PL peak with the pause duration for the $t_1 = 20$ s growth. Then, after reaching its maxima at $t_2 = 12$ s, the peak that was more than twice as large compared to the reference started to decline slightly ($t_2 = 15$ s). A summary of the PL integrated intensity, its spectra position and full width at half maximum (FWHM) as a function of t_2, compared to the reference, is presented in figure 7. The PL integrated intensity (figure 7(a)) and peak position (figure 7(b)) demonstrate a similar track to that of the peak height indicating on In re-evaporation or thermal etching when reaching relatively long growth interruptions, a process lowering the number and the size of PL effective regions and decreasing the thickness of the QWs. The FWHM keeps a common tendency of decreasing with the pause duration, indicating an improvement of the QW due to the pulse growth (figure 7(c)). However, a remarkably rapid increase of the FWHM at a short pause duration $t_2 = 3$ s and 6 s, followed by a decrease to the initial value at longer durations comparable to the reference, is observed for the $t_1 = 20$ s growth. The broad PL spectra at a short pause duration may indicate a large variety of recombination channels involved with the still high In segregation effect. Shorter MO pulses ($t_1 = 10$ s) show a much earlier decrease of the FWHM with the pause duration, same as the already noticed PL peak increase, whereas the blueshift undergo a more rapid increase.

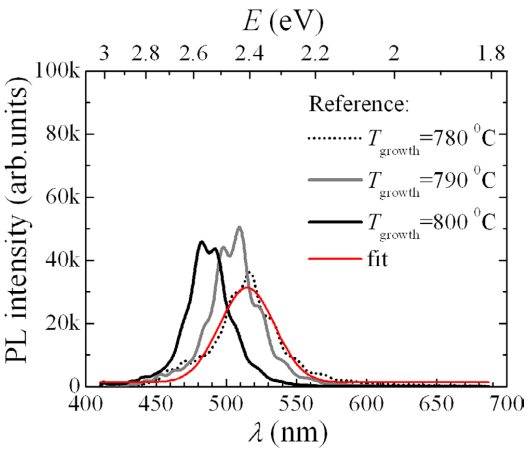

Figure 8. PL spectra of the reference samples grown at different temperatures.

Figure 8 presents the PL spectra measured for three references, where InGaN QWs are grown at different temperatures (780, 790, 800 °C). The PL efficiency and the blueshift have increased with the temperature (dotted curve toward solid). We show that the pulse growth provides the same features already for the structures grown at the lowest temperature: the interruptions introduced into the growth process act as multiple annealing processes, resulting in higher In desorption, especially in In-rich regions around the defect sites which prevent stronger In segregation and new defect creation. However, a comparison of the PL efficiency enhancement (more than two times for the pulsed mode (figure 6), and ~1.3 times for the conventional growth with increasing temperature (figure 8)) for the similar blueshift (~20 nm) shows undisputed merit of the QWs growth using MO interruptions, instead of higher QW growth temperature.

4. Conclusions

A major result of this work is fully strained green light emitting InGaN/GaN MQWs grown at 780 °C temperature under optimized pulse growth conditions. The investigation

revealed that care has to be taken while selecting an appropriate pulse and pause duration ratio for the In and Ga precursor flow interruption. The PL efficiency enhancement up to two times for the green light emitting InGaN/GaN MQWs was observed, when, during the growth of QWs with interruptions, MO pulse durations of 20 s with pause durations of 12s were used. The QW thickness, estimated by TEM measurement, revealed that during the 20 s duration, an MO pulse with about one monolayer of InGaN is grown. The main drawback of the QW growth using the MO flow interruptions is that some decrease of In in the QW leads to the shift of the main PL peak to a shorter wavelength. Some PL efficiency enhancement can be obtained in MQWs grown by shorter MO pulses, but the duration of the pause has to be shortened too, or the blueshift of main PL peak increases drastically.

Acknowledgment

This work was supported by the project NEWLED (EC FP7 #318388).

References

[1] Ponce F A and Bour D P 1997 Nitride-based semiconductors for blue and green light-emitting devices *Nature* **386** 351
[2] Zukauskas A, Shur M S and Gaska R 2002 *Introduction to Solid-State Lighting* (New York: Wiley)
[3] Bernardini F, Fiorentini V and Vanderbilt D 1997 Spontaneous polarization and piezoelectric constants of III–V nitrides *Phys. Rev.* B **56** R10024
[4] Lester S D, Ponce F A, Craford M G and Steigerwald D A 1995 High dislocation densities in high efficiency GaN-based light emitting diodes *Appl. Phys. Lett.* **66** 1249
[5] Narukawa Y, Kawakami Y, Funato M, Fujita S, Fujita S and Nakamura S 1997 Role of self-formed InGaN quantum dots for exciton localization in the purple laser diode emitting at 420 nm *Appl. Phys. Lett.* **70** 981
[6] Chichibu S F *et al* 1998 Effective band gap inhomogeneity and piezoelectric field in InGaN/GaN multiquantum well structures *Appl. Phys. Lett.* **73** 2006
[7] Hangleiter A, Hitzel F, Netzel C, Fuhrmann D, Rossow U, Ade G and Hinze P 2005 Suppression of nonradiative recombination by *V*-shaped pits in GaInN/GaN quantum wells produces a large increase in the light emission efficiency *Phys. Rev. Lett.* **95** 127402
[8] Kaneta A, Funato M and Kawakami Y 2008 Nanoscopic recombination processes in InGaN/GaN quantum wells emitting violet, blue and green spectra *Phys. Rev.* B **78** 125317
[9] Oliver R A, Bennett S E, Zhu T, Beesley D J, Kappers M J, Saxey D W, Cerezo A and Humphreys C J 2010 Microstructural origins of localization in InGaN quantum wells *J. Phys. D: Appl. Phys.* **43** 354003
[10] Nakamura S 1998 The roles of structural imperfections in InGaN-based blue light emitting diodes and laser diodes *Science* **281** 956
[11] O'Donnell K P, Martin R W and Middleton P G 1999 Origin of luminescence from InGaN diodes *Phys. Rev. Lett.* **82** 237
[12] Jinschek J R, Erni R, Gardner N F, Kim A Y and Kisielowski C 2006 Local indium segregation and bang gap variations in high efficiency green light emitting InGaN/GaN diodes *Solid State Commun.* **137** 230
[13] Neugebauer J 2003 Surfactants and antisurfactants on group-III-nitride surfaces *Phys. Stat. Solidi* C **6** 1651
[14] Choi S, Kim T H, Wolter S, Brown A, Everitt H O, Losurdo M and Bruno G 2008 Indium adlayer kinetics on the gallium nitride (0 0 0 1) surface: monitoring indium segregation and precursor-mediated adsorption *Phys. Rev. Lett.* B **77** 115435
[15] Chen H, Feenstra R M, Northrup J E, Zywietz T and Neugebauer J 2000 Spontaneous formation of Indium-rich nanostructures on InGaN(0 0 0 1) surfaces *Phys. Rev. Lett.* **85** 1902
[16] Stringfellow G B 2010 Microstructures produced during the epitaxial growth of InGaN alloys *J. Cryst. Growth* **312** 735
[17] Ponce F A *et al* 2003 Microstructure and electronic properties of InGaN alloys *Phys. Stat. Solidi* B **240** 273
[18] Karpov S Y 1998 Suppression of phase separation in InGaN due to elastic strain *MRS Internet J. Nitride Semicond. Res.* **3** 16
[19] Oliver R A *et al* 2013 The impact of gross well width fluctuations on the efficiency of GaN-based light emitting diodes *Appl. Phys. Lett.* **103** 141114
[20] Wang Y, Pei X J, Xing Z G, Guo L W, Jia H Q, Chen H and Zhou J M 2007 Effects of barrier growth temperature ramp-up time on the photoluminescence of InGaN/GaN quantum wells *J. Appl. Phys.* **101** 033509
[21] Laak N K, Oliver R A, Kappers M J and Humphreys C J 2007 Role of gross well-width fluctuations in bright, green-emitting single InGaN/GaN quantum well structures *Appl. Phys. Lett.* **90** 1911
[22] Lundin W V, Nikolaev A E, Sakharov A V, Yagovkina M A and Tsatsulnikov A F 2014 Properties of InGaN/GaN heterostructures obtained using growth interruptions under various conditions *Tech. Phys. Lett.* **40** 365
[23] Tsatsulnikov A F *et al* 2015 Formation of three-dimensional islands in the active region of InGaN based light emitting diodes using a growth interruption approach *Sci. Adv. Mater.* **7** 1629
[24] Du C, Ma Z, Zhou J, Lu T, Jiang Y, Zuo P, Jia H and Chen H 2014 Enhancing the quantum efficiency of InGaN yellow-green light-emitting diodes by growth interruption *Appl. Phys. Lett.* **105** 071108
[25] Kadys A *et al* 2015 Growth of InN and In-rich InGaN layers on GaN templates by pulsed metalorganic chemical vapor deposition *J. Electron. Mater.* **44** 188
[26] Vurgaftman I and Meyer J R 2003 Band parameters for nitrogen-containing semiconductors *J. Appl. Phys.* **94** 3675
[27] Moram M A and Vickers M E 2009 X-ray diffraction of III-nitrides *Rep. Progr. Phys.* **72** 1
[28] Pereira S, Correia M R, Pereira E, O'Donnell K P, Alves E, Sequeira A D, Franco N, Watson I M and Deatcher C J 2002 Strain and composition distributions in wurtzite InGaN/GaN layers extracted from x-ray reciprocal space mapping *Appl. Phys. Lett.* **80** 3913
[29] Kim Y H, Kim C S, Noh S K, Ban S I, Kim S G, Lim K Y and O B S 2003 Structural characterization of InGaN/GaN multi-quantum well structures using high-resolution XRD *J. Korean Phys. Soc.* **42** S285
[30] Tsai W C, Hsu C H, Fu S F, Lee F W, Chen C Y, Chou W C, Chen W K and Chang W H 2014 Optical properties associated with strain relaxations in thick InGaN epitaxial films *Opt. Express* **22** A416
[31] Xi G, Hui W, De-Sheng J, Yu-Tian W, De-Gang Z, Jian-Jun Z, Zong-Shun L, Shu-Ming Z and Hui Y 2010 Evaluation of both composition and strain distributions in InGaN epitaxial film using x-ray diffraction techniques *Chin. Phys.* B **19** 106802
[32] Ju G, Fuchi S, Tabuchi M and Takeda Y 2013 *In situ* x-ray reflectivity measurements on annealed $In_xGa_{1-x}N$ epilayer grown by metalorganic vapor phase epitaxy *Japan. J. Appl. Phys.* **52** 08JB12

[33] Ju G, Honda Y, Tabuchi M, Takeda Y and Amano H 2014 *In situ* x-ray investigation of changing barrier growth temperatures on InGaN single quantum wells in metal-organic vapor phase epitaxy *J. Appl. Phys.* **115** 094906
[34] Wu X H, Elsass C R, Abare A, Mack M, Keller S, Petroff P M, DenBaars S P, Speck J S and Rosner S J 1998 Structural origin of *V*-defects and correlation with localized excitonic centers in InGaN/GaN multiple quantum wells *Appl. Phys. Lett.* **72** 692
[35] Chen Y, Takeuchi T, Amano H, Akasaki I, Yamada N, Kaneko Y and Wang S Y 1998 Pit formation in GaInN quantum wells *Appl. Phys. Lett.* **72** 710
[36] Shiojiri M, Chuo C C, Hsu J T, Yang J R and Saijo H 2006 Structure and formation mechanism of V defects in multiple InGaN/GaN quantum well layers *J. Appl. Phys.* **99** 073505
[37] Sugahara T, Hao M, Wang T, Nakagawa D, Naoi Y, Nishino K and Sakai S 1998 Role of dislocation in InGaN phase separation *Japan. J. Appl. Phys.* **37** L1195
[38] Lei H, Chen J and Ruterana P 2010 Role of *c*-screw dislocations on indium segregation in InGaN and InAlN alloys *Appl. Phys. Lett.* **96** 161901
[39] Massabuau F C P, Sahonta S L, Trinh-Xuan L, Rhode S, Puchtler T J, Kappers M J, Humphreys C J and Oliver R A 2012 Morphological, structural, and emission characterization of trench defects in InGaN/GaN quantum well structures *Appl. Phys. Lett.* **101** 212107
[40] Bruckbauer J, Edwards P R, Wang T and Martin R W 2011 High resolution cathodoluminescence hyperspectral imaging features in InGaN/GaN multiple quantum well structures *Appl. Phys. Lett.* **98** 141908

Paper III

Correlation between growth interruption and indium segregation in InGaN MQWs

M. Dmukauskas, J. Mickevičius, D. Dobrovolskas, A. Kadys,
S. Nargelas, G. Tamulaitis

Journal of Luminescence, 221, (2020).
DOI: 10.1016/j.jlumin.2020.117103

Journal of Luminescence 221 (2020) 117103

Contents lists available at ScienceDirect

Journal of Luminescence

journal homepage: http://www.elsevier.com/locate/jlumin

Correlation between growth interruption and indium segregation in InGaN MQWs

M. Dmukauskas, J. Mickevičius *, D. Dobrovolskas, A. Kadys, S. Nargelas, G. Tamulaitis

Institute of Photonics and Nanotechnology, Vilnius University, Saulėtekio al. 3, LT-10257, Vilnius, Lithuania

ARTICLE INFO

Keywords:
III-Nitrides
InGaN
Photoluminescence
Carrier localization

ABSTRACT

InGaN/GaN multiple quantum wells (MQWs) with the same indium content and QW widths were grown by metalorganic chemical vapor deposition using metal precursor flow interruptions of different length. The influence of the growth interruption length on photoluminescence (PL) properties was studied by combining temperature-dependent and spatially-resolved PL spectroscopy. The PL band variations are attributed to the transformation of localizing potential: growth interruptions change the density of indium clusters, which modifies the density of localized states. The optimized localizing potential in the structure grown using 9 s-long growth interruptions facilitated an increase in PL intensity by a factor of up to 2.

1. Introduction

InGaN-based photonic devices are extensively used in general lighting and large area displays because of the high room-temperature internal quantum efficiencies achievable in InGaN/GaN quantum well (QW) structures. It is generally accepted that the influence of dislocations and point defects, as nonradiative recombination centers, are strongly diminished due to the localization of carriers in potential minima [1,2]. Nevertheless, the efficiency rapidly decreases as the emission wavelength is shifted from the blue spectral region to green [3]. This efficiency loss is usually attributed to several factors contributing together [4,5]. Higher indium content necessary to shift the emission wavelength results in a larger lattice-mismatch-induced strain of InGaN QWs, which might facilitate the formation of dislocations [6]. The larger strain also enhances the quantum confined Stark effect (QCSE), which increases the separation of electrons and holes to the opposite sides of the QW. Additionally, the increasing atomic-scale indium content fluctuations and uncorrelated carrier localization causes the reduction of the in-plane overlap of electron and hole wave functions [7].

While InGaN QWs are predicted to have random alloy fluctuations [8,9], one should expect some deviation from such an idealized structure. The compositional uniformity in active InGaN layers is affected by the growth conditions of the QWs as well as by the presence of extended defects: lower growth temperatures, typically used to increase the indium content, favor the point defect formation and parasitic impurity incorporation [10] alongside the indium segregation within InGaN layers [11]. Moreover, indium atoms tend to segregate in the vicinity of dislocations [12]. Thus, as the indium content in InGaN QWs and epilayers is increased, higher defect concentration drives the segregation process [13], and partially relaxed regions with a higher density of nonradiative recombination centers (NRCs) and a higher density of localized states might be formed [1,14]. Several techniques have been proposed to reduce the indium segregation. Treatment by trimethylindium (TMIn) prior to the QW growth results in an increased efficiency, though the In segregation is not reduced, as evidenced by the red shift of photoluminescence (PL) band [15,16]. Conversely, the TMIn treatment after the QW growth causes smoother interfaces and improves the luminescence efficiency [17]. Alternative methods are based on the interruptions during the growth of QWs: modulating the flow of both In and Ga precursors is claimed to result in more uniform In composition within QWs and enhancement of PL efficiency [11,18]. Modulating the flow of only Ga precursor, while maintaining the TMIn flow constant, led to stronger and narrower luminescence line and smaller band blue shift with increasing driving current, which was attributed to the better homogeneity of indium composition [19]. A growth technique based on InN/GaN growth switching resulted in a higher emission efficiency but also in a larger emission wavelength blue shift with increasing current [20].

In this paper, we report on a study of the influence of the growth interruption length on the emission properties in InGaN/GaN multiple quantum wells (MQWs) by using temperature-dependent and spatially-

* Corresponding author.
E-mail address: juras.mickevicius@ff.vu.lt (J. Mickevičius).

https://doi.org/10.1016/j.jlumin.2020.117103
Received 26 March 2019; Received in revised form 5 February 2020; Accepted 7 February 2020
Available online 8 February 2020

resolved photoluminescence spectroscopy. Despite having the same structure and average indium content in QWs, the samples grown with different growth interruption length exhibited certain differences in PL band properties. The correlation between growth interruption length and PL band parameters both on macro- and micro-scales is analyzed and attributed to the localizing potential variations.

2. Experimental

The samples were grown using metalorganic chemical vapor deposition (MOCVD) in a close-coupled showerhead 3 × 2″ reactor (AIXTRON). Trimethylgallium (TMGa), trimethylindium, and ammonia (NH_3) were used as Ga, In, and N precursors, respectively. N_2 was used as the ambient and carrier gas. 3-μm-thick c-plane GaN templates deposited on sapphire were used as substrates. To improve the optical properties of the structure, the active layers were grown on a short-period superlattice (SPSL) [21,22]. The SPSL consisted of 9 periods of alternating low-In-content $In_xGa_{1-x}N$ ($x = 4$–5%) and GaN layers grown in a conventional MOCVD regime at the temperature of 850 °C.

The InGaN/GaN MQWs consisted of five pairs of QWs and barriers. The QWs were grown at the pressure of 400 mBar using a pulsed growth regime, which was accomplished by modulating the flow of In and Ga precursors, while maintaining the flow of NH_3 constant. The NH_3 flow was maintained at 0.268 mol/min, whereas TMIn and TMGa flows during the supply pulse were 9.0×10^{-6} and 3.2×10^{-6} mol/min, respectively. Both metalorganic precursors were delivered into the reactor chamber simultaneously for 20 s, the growth interruption length varied from 3 to 15 s (samples S3, S6, S9, S12, and S15, respectively). An additional reference sample was grown in the conventional continuous-flow regime (growth interruption length of 0 s, sample S0). The growth temperature of QWs was 800 °C. Right after the QW growth, ~1 nm GaN layer was deposited at the same temperature to prevent In decomposition, and the temperature was ramped up with TMIn and TMGa flows switched off. The GaN barriers were grown in the usual continuous flow regime at the temperature of 840 °C. A thin (25–30 nm) GaN capping layer was grown on the top of active layer.

By combining X-ray diffraction (XRD) and transmission electron microscopy (TEM) measurements, the MQWs samples were found to have GaN barriers of thickness 6.9 ± 0.3 nm and InGaN QWs of thickness 4.0 ± 0.2 nm with indium content of 9.9 ± 0.7% (more details are provided in Fig. SM1 in supplementary materials). Surface morphology was studied by atomic force microscopy (AFM) in contact mode (*WITec Alpha 300S*). Photoluminescence of the samples was studied under steady-state excitation conditions using CW He–Cd laser (325 nm). The luminescence signal was analyzed by a double monochromator (*Jobin Yvon HRD-1*) and detected by a photomultiplier (*Hamamatsu*). The measurements were performed in a wide temperature range from 8 to 300 K using a closed-cycle helium cryostat. To eliminate the oscillations due to Fabry-Perot interference, the PL spectra were processed using FFT filtering, as illustrated in Fig. SM2 in supplementary materials. The study of the spatial variation of PL parameters on a sub-micrometer scale was performed using *WITec Alpha 300* microscope system operated in confocal mode. For recording the spatially-resolved spectra, the microscope was coupled via an optical fiber with spectrometer *UHT300* followed by a CCD camera. A CW laser diode (405 nm) was exploited for excitation. A high numerical aperture (NA = 0.9) objective was used to focus the excitation laser beam and to collect the luminescence signal in order to ensure the in-plane spatial resolution of ~250 nm. The confocal scans were performed at room temperature over randomly selected areas of 10 × 10 μm^2 with a step of 50 nm to provide an image of 200 × 200 pixels.

3. Results and discussion

Fig. 1 presents the room-temperature PL spectra of InGaN/GaN MQWs grown using different length of growth interruptions (the low-temperature spectra are provided in the Fig. SM3 in supplementary materials). While the shape of all the spectra is similar, certain changes with increasing growth interruption length can be observed. By increasing growth interruption length, a general although non-monotonous trend is the increase of PL intensity by up to a factor of 2 in sample S9, and the blue shift of the peak position by up to 54 meV in sample S15. Meanwhile, the PL bandwidth is 147 meV in sample S0, slightly increases to 160 meV in sample S3, and remains very similar for further increases of growth interruption length. The internal quantum efficiency (IQE), defined as the ratio between PL intensities at 300 and 8 K temperatures, increases from 4% up to 7.3% in samples S0 and S9, respectively, and is presented in the inset in Fig. 1. The extracted PL spectra parameters are summarized in Table 1.

Since both the indium content and QW width are very similar amongst the studied samples, the changes in PL spectra have to be caused by the modifications of localizing potential and/or density of NRCs. The increase in PL band width implies increasing fluctuations of localizing potential, however, the blue shift of the peak position points to the higher average energy of the filled localized states. Meanwhile, the PL intensity increase indicates decreasing contribution of non-radiative recombination due to either reduction of the density of NRCs or more favorable localizing potential.

The carrier localization conditions in the InGaN/GaN MQWs under study were estimated using the temperature dependence of the PL band peak position. The PL spectra measured at different temperatures are shown in Fig. 2(a) for sample S3. Points in Fig. 2(b) present the shift of the PL band peak with respect to the peak position at 8 K. All the samples exhibited a so-called S-shape dependence with three shift regions: redshift-blueshift-redshift. Such S-shape dependence is typical of ternary III-nitrides and is usually attributed to hopping of carriers (excitons) through localized states [23,24]. The blueshift-redshift region of the peak position dependence at elevated temperatures can be described using a simple quantitative model linking it to the fluctuations of the local potential. At nondegenerate occupation, the temperature dependence of the PL peak position can be expressed as [23]:

$$E_{peak}(T) = E_g(0) - \frac{\alpha T^2}{\beta + T} - \frac{\sigma^2}{k_B T}. \quad (1)$$

Here, $E_g(0)$ is the band gap at $T = 0$, α and β are Varshni coefficients for band gap reduction with temperature, and σ is the standard deviation of the Gaussian distribution of the band gap fluctuations due to the random fluctuations in In content and/or QW width. Several

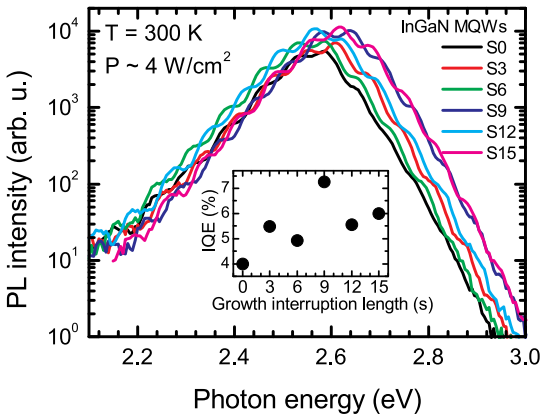

Fig. 1. PL spectra of InGaN/GaN MQWs samples grown using different interruption length: 0, 3, 6, 9, 12, and 15 s (reflected in sample labeling, indicated) measured under excitation power density of 4 W/cm^2 at 300 K. Inset shows the IQE dependence on growth interruption length.

Table 1
Macro-PL data of the InGaN/GaN MQWs under study.

Sample	S0	S3	S6	S9	S12	S15
Growth interruption length (s)	0	3	6	9	12	15
PL intensity at 8 K (arb. u.)[a]	1.00	1.10	1.13	1.22	1.25	1.19
PL intensity at 300 K (arb. u.)[a]	1.00	1.52	1.40	2.22	1.74	1.79
IQE (%)	4.0	5.5	4.9	7.3	5.6	6.0
Peak position at 300 K (eV)	2.574	2.595	2.563	2.615	2.568	2.628
FWHM at 300 K (meV)	147	160	158	160	160	164

[a] PL intensities are normalized with respect to sample S0.

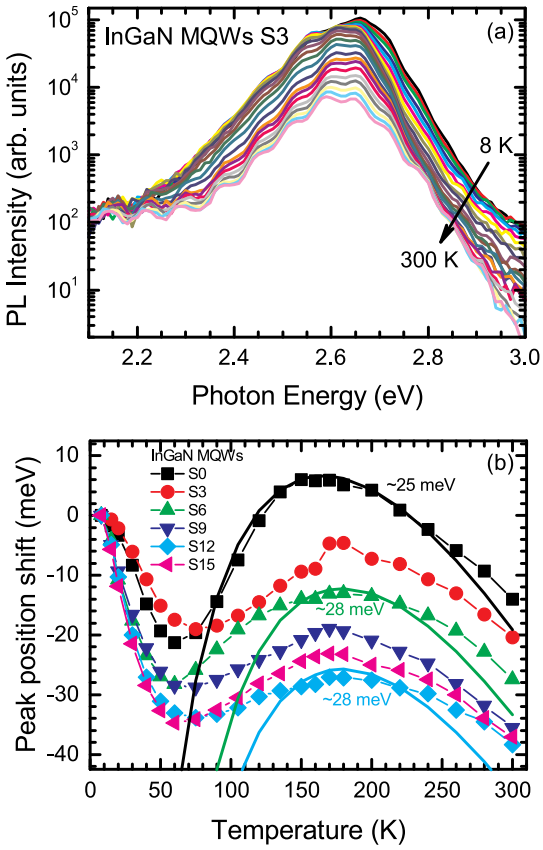

Fig. 2. PL spectra of InGaN MQWs sample S3 measured at different temperatures (a), and temperature dependences of PL band peak position shift in InGaN/GaN MQWs under study (b). Solid lines in (b) show the fits using a simple model of carrier (exciton) hopping through the localized states.

dependences of the PL peak position shown by solid lines in Fig. 2(b) were calculated according to Eq. (1) with α and β values of 0.85 meV/K and 800 K, respectively (interpolated between GaN and InN values taken from Refs. [25,26]).

As seen in Fig. 2(b), the fit is tolerable only for the sample S0 with the estimated σ value of 25 meV, however, fails to capture the complexity of the experimental dependences for the samples grown using growth interruptions. Nevertheless, transformation of S-shape with increasing growth interruption length is evident: the initial red shift becomes larger, while the peak blue shift decreases. The temperatures corresponding to redshift-blueshift and blueshift-redshift turning points are approximately constant for all samples, except for sample S0, which exhibits its turning points at slightly lower temperatures. This difference hints at slightly larger potential fluctuations in the samples grown using growth interruptions.

The experimental macro-PL results show that the introduction of growth interruptions results in slightly wider energy distribution of localized states. On the other hand, low variations of room-temperature PL band widths and blueshift-redshift turning points indicate a negligible influence of the length of growth interruptions. Nevertheless, the increasing value of the initial red shift at low temperatures points to certain transformations of the localizing potential. Using the approach of Refs. [27–29], the localized states can be qualitatively divided into shallow and deep states, having, respectively, smaller and larger energy difference from the mobility edge. The observed changes in PL band properties can then be interpreted by the changing contributions of the shallow and deep states. Since the initial temperature-dependent red shift occurs due to thermally-activated carrier redistribution to the lower available states, the larger red shift suggests a larger density of available deep localized states. On the other hand, at room temperature, the carriers are able to redistribute efficiently and a larger fraction of shallow localized states is occupied, while the observed blueshifted PL band position implies a decreased energy difference of deep localized states from the mobility edge. Taking into account the similarity of indium content and QW width amongst the samples, the two observations lead to a conclusion that the main effect of the increasing growth interruption length is on the properties of deep localized states: their density increases, while the energy difference from the mobility edge decreases. Such transformation results in the asymmetric density of localized states function, which manifests in the worsening fits of the peak position shift dependences shown in Fig. 2(b).

To understand better the peculiarities of the localizing potential and its modifications with increasing growth interruption length, we studied the spatial variations of PL parameters with a sub-micrometer spatial resolution. Typical images of the spatial distributions of PL intensity and peak position are shown in Fig. 3(a) and (b), respectively, for sample S3 (the corresponding images for all the studied samples can be found in the supplementary materials). The statistically averaged data extracted for all the studied samples are listed in Table 2.

In spatially resolved images, an inhomogeneous PL intensity distribution is observed: a pattern of round-shaped areas of higher emission intensity on a background of lower emission intensity. The spatial PL intensity variation (the standard deviation divided by the mean value) was approximately 0.47 for all the samples under study. A similar inhomogeneous distribution was also observed for the peak position. The spatial variations of the PL band peak position were rather small and varied in the range from 3 to 4 nm (16–20 meV) for the studied samples. The correlation between the peak wavelength and PL intensity was positive and strong: the Pearson's product moment correlation coefficient R was in the range from 0.3 to 0.6 with the trend of slight decrease as the growth interruption length increased. This positive correlation is common in InGaN and is caused by a lower probability to reach NRCs for those carriers, which are localized at deeper energy levels and, correspondingly, are emitting at longer wavelengths [30,31].

Even though the spatial variations of the PL spectra peak position are not large, the single-pixel spectra (collected from an area of 50×50 nm^2 in our experiments) are rather broad, with the average PL band width ranging from 110 to 125 meV in the studied samples. The large widths of the PL spectra from individual pixels indicate the presence of the double-scaled potential profile: the larger areas (hundreds of nanometers) with different average potential are revealed by the peak wavelength variations, whereas the small-scale potential fluctuations (probably, of a few nanometers in size) manifest themselves through the inhomogeneous broadening of the local PL spectra. The double-scaled potential profile

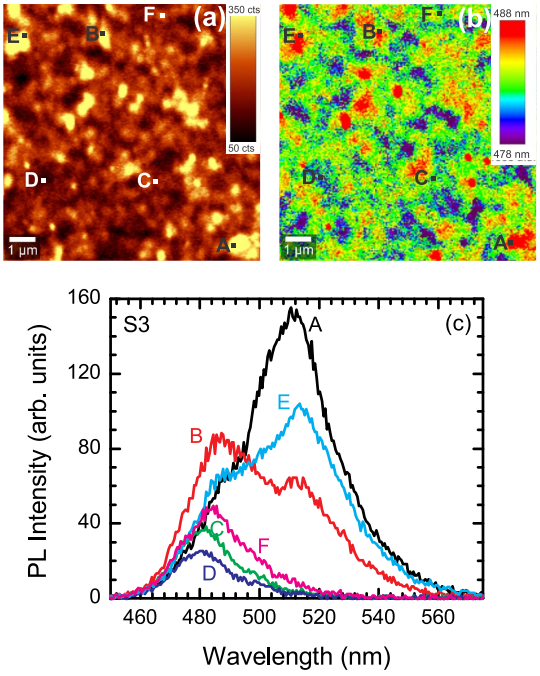

Fig. 3. Spatial distribution of spectrally-integrated PL intensity (a) and PL band peak wavelength (b) within an area of 10 × 10 μm^2 of InGaN/GaN MQWs sample S3 and several PL spectra (c) taken from indicated spots.

Table 2
Statistical parameters of the confocal scans of the InGaN/GaN MQWs under study.

Sample	S0	S3	S6	S9	S12	S15
Growth interruption length (s)	0	3	6	9	12	15
Intensity variation	0.48	0.43	0.44	0.43	0.47	0.54
Peak wavelength mean (nm)	487	483	489	479	485	480
Peak wavelength deviation (nm)	4.0	3.4	3.2	3.0	3.3	3.7
FWHM mean (meV)	110	125	125	121	123	124
FWHM deviation (meV)	20	17	15	15	13	18
Peak wavelength-to-peak intensity Pearson correlation coefficient	0.58	0.61	0.47	0.56	0.31	0.48
Peak wavelength-to-FWHM Pearson correlation coefficient	0.59	0.52	0.44	0.46	0.28	0.43

model has been previously used to interpret the carrier migration and recombination peculiarities in InGaN/GaN MQWs structures [30,31]. Both large- and small-scale inhomogeneities have also been observed experimentally using scanning near-field optical microscopy (SNOM) [32,33], cathodoluminescence (CL), μ-PL [34], and Z-contrast [35] techniques.

The detailed analysis of the single-pixel PL spectra [the typical spectra for different spots are shown in Fig. 3(c)] revealed areas having considerably larger than average PL band width with some of these areas also having a significantly redshifted peak position [curves A and E in Fig. 3(c)]. As can be observed, the increase of the PL band width is caused by the emergence of the second PL band on the long wavelength slope at ~510 nm. When the intensity of this second PL band is high enough, it also results in the strong red shift of the overall PL spectrum. Such double-peaked PL spectra have been assigned to the luminescence from the spots in the vicinity of V-pits [36,37]: the long-wavelength band is attributed to the spontaneous formation of In-rich regions around the V-pits [36], while the short-wavelength band corresponds to the emission from the V-pit itself [37]. Additionally, the PL band red shift accompanied by an increase of PL intensity might be caused by the trench defects [38].

The V-pit and trench defect densities were evaluated using AFM measurements. A typical image is shown in Fig. 4(a). The estimated V-pit density is 8.5 × 10^8 cm^{-2} in sample S0, and slightly increases to 1.3 × 10^9 cm^{-2} and 1.6 × 10^9 cm^{-2} in samples S3 and S15, respectively, showing no significant correlation with the growth interruption length. Meanwhile, the trench defect density is very similar for all the studied samples and ranges from 1 × 10^7 to 2.4 × 10^7 cm^{-2}. The spatial resolution of AFM measurements is substantially better than that of PL imaging, thus, the adjacent V-pits can hardly be resolved in the images of PL parameters. For the typical V-pit diameter of 80 nm and the in-plane spatial resolution of 250 nm in confocal PL measurements, the blur effectively reduces the resolved V-pit density by an order of magnitude. Thus, the total resolvable defect density is 1 × 10^8 cm^{-2} in sample S0, and (1.5–1.7) × 10^8 cm^{-2} in other samples. Similar densities of areas having larger than average PL band width can be observed in spatial PL band width distribution images [see Fig. 4(b)]. Here, the marked pixels are distinguished by the PL band width, which is above the average by at least 1.5*s*, where *s* is the standard deviation of band width distribution. Since such pixels take only ~3–4% of the total area, they do not considerably affect the mean values, i.e., the parameters of the spatially-integrated PL band. Furthermore, the lack of considerable correlation between the growth interruption length and the defect densities (either from AFM images or from PL bandwidth images) implies a negligible role of defects on the transformation of localizing potential. On the other hand, the presence of defects already involves certain potential fluctuations, e.g., the spontaneous formation of In-rich regions around V-pits, as mentioned above.

To study the effect of the growth interruption length on the deep localized states, we analyzed the areas having a significantly redshifted PL band peak position. The typical spatial distribution image of such areas is shown in Fig. 5(a) for sample S3. The image was obtained from the peak position distribution, as in Fig. 3(b), by selecting pixels having the PL band peak position at considerably longer wavelength than the mean position, i.e. redshifted more than the standard deviation [e.g., spots A and E in Fig. 3(c)]. The compiled histograms reflecting the density of pixels with certain peak position are provided in supplementary materials. The estimated number of grains is 413 with the average grain area and total covered area equal to 9500 nm^2 and 3.918 μm^2, respectively. The average peak position of the deep localized states was 492.3 nm. Likewise, the grain parameters were estimated for all the samples under study, and their dependences on the growth interruption length are shown in Fig. 5(b)–(d). The increase of the growth

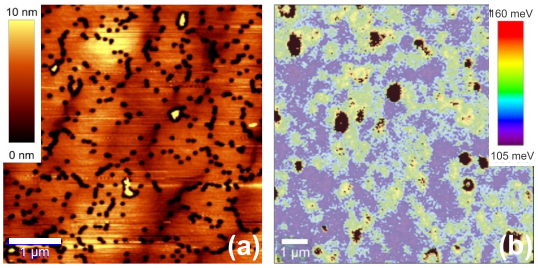

Fig. 4. Surface topography within an area of 5 × 5 μm^2 (a) and spatial distribution of PL band width within an area of 10 × 10 μm^2 (b) of InGaN/GaN MQWs sample S3. The PL band width in marked pixels is above average by at least 1.5*s*, where *s* is the standard deviation of band width distribution.

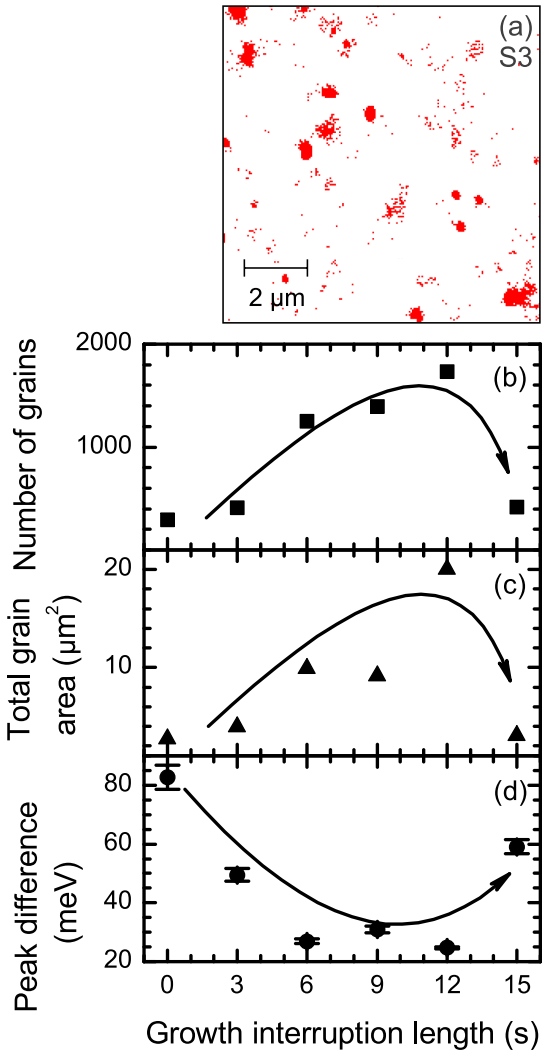

Fig. 5. The redshifted grains in the peak position image of sample S3 (a) and the growth interruption length dependences of the number of grains (b), the total grain area (c), and the difference between the average band peak position over the entire area and the mean value of the peak position in the areas dominated by deep localized states (d). Error bars in (d) represent the standard error.

interruption length up to 12 s results in the increase of the number of grains and the total area covered by the grains.

All the experimental observations support the proposition that the changes in PL band properties are caused by the modifications of the localizing potential due to changes in growth conditions. The longer growth interruptions result in a higher effective V/III ratio due to an extended supply of NH_3. Higher V/III ratio has been shown to produce smaller and denser islands [39,40]. Moreover, the extra time for nitridation and migration of In and Ga atoms on the surface suppresses any kind of metal segregation, either lateral or vertical [41,42]. The In clusters manifest in the peak position images as the redshifted grains. Indeed, the density of grains increases in the samples grown using longer growth interruptions (see Fig. 5). Meanwhile, the decreasing difference between the overall peak position mean and the average peak position in deep localized states (see Fig. 5 and Fig. SM4) points to the decreasing energy difference between deep states and mobility edge, consistently with the PL band blue shift (see Fig. 1). On the other hand, the increasing density of the clusters ensues an increase in the total area covered by the redshifted grains and indicates higher total density of localized states, which is consistent with the higher range of the initial red shift in temperature dependence of PL band peak position [see Fig. 2(b)]. As a result of the aforementioned transformations, the PL intensity increases by a factor of up to 2, despite similar increase in the V-pit density. Thus, the longer interruption length facilitates formation of the localizing potential, which inhibits migration of nonequilibrium carriers to nonradiative recombination centers. However, the excessive increase of grain-covered area diminishes the positive effect of growth interruptions, probably, due to increasing density of accompanying nonradiative recombination centers, as indicated by the reduced peak wavelength-FWHM correlation coefficient [14]. In contrast, the formation of grains ceases for 15 s-long interruptions, when the positive changes are overshadowed by the effects of indium re-evaporation or thermal etching.

4. Conclusions

To summarize, the influence of growth interruption length on photoluminescence properties was studied for InGaN/GaN quantum well structures grown using pulsed MOCVD on c-plane sapphire substrates. Increasing the growth interruption length leads to a higher PL efficiency and a slight blue shift and broadening of PL band. Combining the results obtained from the temperature dependences of PL parameters and spatially-resolved PL measurements, the PL band variations were attributed to the modifications of localizing potential. Increasing the growth interruption length to ~12 s results in a higher density of indium clusters in QWs and increases the total density of localized states. Meanwhile, the average energy of deep localized states is shifted towards the mobility edge. The highest PL efficiency was observed in the structure grown using the growth interruptions of 9 s, indicating the optimal localizing potential. The optimization inhibits carrier migration to nonradiative recombination centers, despite the increase in the defect density, and increases the PL intensity by a factor of up to 2.

CRediT authorship contribution statement

M. Dmukauskas: Conceptualization, Investigation. **J. Mickevičius:** Investigation, Writing - original draft. **D. Dobrovolskas:** Investigation, Formal analysis. **A. Kadys:** Conceptualization, Methodology, Resources. **S. Nargelas:** Writing - review & editing, Funding acquisition. **G. Tamulaitis:** Supervision, Writing - review & editing.

Acknowledgments

The research was supported by the Lithuanian Research Council (Contract. No. S-MIP-17-75).

Appendix A. Supplementary data

Supplementary data to this article can be found online at https://doi.org/10.1016/j.jlumin.2020.117103.

References

[1] A. Kaneta, M. Funato, Y. Kawakami, Phys. Rev. B 78 (2008) 125317.
[2] D. Watson-Parris, M.J. Godfrey, P. Dawson, R.A. Oliver, M.J. Galtrey, M.J. Kappers, C.J. Humphreys, Phys. Rev. B 83 (2011) 115321.
[3] T.D. Moustakas, R. Paiella, Rep. Prog. Phys. 80 (2017) 106501.
[4] Y.-C. Leem, S.-Y. Yim, ACS Photonics 5 (2018) 1129.
[5] S.Yu Karpov, Photon. Res. 5 (2017) A7.

[6] A.V. Lobanova, A.L. Kolesnikova, A.E. Romanov, S.Yu Karpov, M.E. Rudinsky, E. V. Yakovlev, Appl. Phys. Lett. 103 (2013) 152106.
[7] M. Auf der Maur, A. Pecchia, G. Penazzi, W. Rodrigues, A. Di Carlo, Phys. Rev. Lett. 116 (2016), 027401.
[8] K.H. Baloch, A.C. Johnston-Peck, K. Kisslinger, E.A. Stach, S. Gradecak, Appl. Phys. Lett. 102 (2013) 191910.
[9] C.J. Humphreys, J.T. Griffiths, F. Tang, F. Oehler, S.D. Findlay, C. Zheng, J. Etheridge, T.L. Martin, P.A.J. Bagot, M.P. Moody, D. Sutherland, P. Dawson, S. Schulz, S. Zhang, W.Y. Fu, T. Zhu, M.J. Kappers, R.A. Oliver, Ultramicroscopy 176 (2017) 93.
[10] S. Hammersley, M.J. Kappers, F.C.-P. Massabuau, S.-L. Sahonta, P. Dawson, R. A. Oliver, C.J. Humphreys, Appl. Phys. Lett. 107 (2015) 132106.
[11] C. Du, Z. Ma, J. Zhou, T. Lu, Y. Jiang, P. Zuo, H. Jia, H. Chen, Appl. Phys. Lett. 105 (2014), 071108.
[12] F.C.-P. Massabuau, M.K. Horton, E. Pearce, S. Hammersley, P. Chen, M.S. Zielinski, T.F.K. Weatherley, G. Divitini, P.R. Edwards, M.J. Kappers, C. McAleese, M. A. Moram, C.J. Humphreys, P. Dawson, R.A. Oliver, J. Appl. Phys. 125 (2019) 165701.
[13] M.H. Zoellner, G.A. Chahine, L. Lahourcade, C. Mounir, C.L. Manganelli, T. U. Schulli, U.T. Schwarz, R. Zeisel, T. Schroeder, ACS Appl. Mater. Interfaces 11 (2019) 22834.
[14] M.D. Mensi, D.L. Becerra, R. Ivanov, S. Marcinkevičius, S. Nakamura, S. P. DenBaars, J.S. Speck, Opt. Mater. Express 6 (2016) 39.
[15] M.S. Kumar, J.Y. Park, Y.S. Lee, S.J. Chung, C.-H. Hong, E.-K. Suh, Jpn. J. Appl. Phys. 47 (2008) 839.
[16] B. Xu, J.L. Zhao, H.T. Dai, S.G. Wang, R.-M. Lin, F.-C. Chu, C.-H. Huang, S.-F. Yu, X. W. Sun, Thin Solid Films 551 (2014) 142.
[17] H.-C. Lin, R.-S. Lin, J.-I. Chyi, Appl. Phys. Lett. 92 (2008) 161113.
[18] M. Dmukauskas, A. Kadys, T. Malinauskas, T. Grinys, I. Reklaitis, K. Badokas, M. Skapas, R. Tomašiūnas, D. Dobrovolskas, S. Stanionytė, I. Pietzonka, M. Strassburg, H.-J. Lugauer, J. Phys. D Appl. Phys. 49 (2016) 505101.
[19] L. Qiao, Z.-G. Ma, H. Chen, H.-Y. Wu, X.-F. Chen, H.-J. Yang, B. Zhao, M. He, S.-W. Zheng, S.-T. Li, Chin. Phys. B 25 (2016) 107803.
[20] W.-C. Lai, C.-H. Yen, S.-J. Chang, Appl. Phys. Express 6 (2013) 102101.
[21] C.-L. Tsai, J. Lumin. 174 (2016) 36.
[22] W. Qi, J. Zhang, C. Mo, X. Wang, X. Wu, Z. Quan, G. Wang, S. Pan, F. Fang, J. Liu, F. Jiang, J. Appl. Phys. 122 (2017), 084504.
[23] P.G. Eliseev, P. Perlin, J. Lee, M. Osinski, Appl. Phys. Lett. 71 (1997) 569.
[24] A. Bell, S. Srinivasan, C. Plumlee, H. Omiya, F.A. Ponce, J. Christen, S. Tanaka, A. Fujioka, Y. Nakagawa, J. Appl. Phys. 95 (2004) 4670.
[25] I. Vurgaftman, J.R. Meyer, L.R. Ram-Mohan, J. Appl. Phys. 89 (2001) 5815.
[26] J. Wu, W. Walukiewicz, W. Shan, K.M. Yu, J.W. Ager III, S.X. Li, E.E. Haller, H. Lu, W.J. Schaff, J. Appl. Phys. 94 (2003) 4457.
[27] D.S.P. Tanner, M.A. Caro, E.P. O'Reilly, S. Schulz, RSC Adv. 6 (2016) 64513.
[28] T. Lin, H.C. Kuo, X.D. Jiang, Z.C. Feng, Nanoscale Res. Lett. 12 (2017) 137.
[29] W.E. Blenkhorn, S. Schulz, D.S.P. Tanner, R.A. Oliver, M.J. Kappers, C. J. Humphreys, P. Dawson, J. Phys. Condens. Matter 30 (2018) 175303.
[30] J. Mickevičius, D. Dobrovolskas, J. Aleknavičius, T. Grinys, A. Kadys, G. Tamulaitis, J. Lumin. 199 (2018) 379.
[31] K. Gelžinytė, R. Ivanov, S. Marcinkevicius, Y. Zhao, D.L. Becerra, S. Nakamura, S. P. DenBaars, J.S. Speck, J. Appl. Phys. 117 (2015), 023111.
[32] A. Pinos, V. Liuolia, S. Marcinkevičius, J. Yang, R. Gaska, M.S. Shur, J. Appl. Phys. 109 (2011) 113516.
[33] S. Marcinkevičius, R. Jain, M. Shatalov, J. Yang, M. Shur, R. Gaska, Appl. Phys. Lett. 105 (2014) 241108.
[34] Y. Iwata, T. Oto, D. Gachet, R.G. Banal, M. Funato, Y. Kawakami, J. Appl. Phys. 117 (2015) 115702.
[35] D.M. Graham, A. Soltani-Vala, P. Dawson, M.J. Godfrey, T.M. Smeeton, J. S. Barnard, M.J. Kappers, C.J. Humphreys, E.J. Thrush, J. Appl. Phys. 97 (2005) 103508.
[36] T. Tao, T. Zhi, B. Liu, Y. Li, Z. Zhuang, Z. Xie, D. Chen, P. Chen, R. Zhang, Y. Zheng, Phys. Status Solidi 211 (2014) 2823.
[37] N. Okada, H. Kashihara, K. Sugimoto, Y. Yamada, K. Tadatomo, J. Appl. Phys. 117 (2015), 025708.
[38] A. Vaitkevičius, J. Mickevičius, D. Dobrovolskas, O. Tuna, C. Giesen, M. Heuken, G. Tamulaitis, J. Appl. Phys. 115 (2014) 213512.
[39] H. Wang, D.S. Jiang, J.J. Zhu, D.G. Zhao, Z.S. Liu, Y.T. Wang, S.M. Zhang, H. Yang, Semicond. Sci. Technol. 24 (2009), 055001.
[40] A. Kadir, K. Bellmann, T. Simoneit, M. Pristovsek, M. Kneissl, Phys. Status Solidi 209 (2012) 2487.
[41] J. Neugebauer, Phys. Status Solidi C (2003) 1651, 0.
[42] S. Choi, T.-H. Kim, S. Wolter, A. Brown, H.O. Everitt, M. Losurdo, G. Bruno, Phys. Rev. B 77 (2008) 115435.

UŽRAŠAMS

UŽRAŠAMS

Vilniaus universiteto leidykla
Saulėtekio al. 9, LT-10222 Vilnius
info@leidykla.vu.lt, www.leidykla.vu.lt
Tiražas 12 egz.